

**GRAPHENE-BASED MULTISCALE MULTIPHASE
SELF-SENSING COMPOSITES**

By

Nathan Hostettler

A thesis submitted to McGill University in partial fulfilment of the requirements of the
degree of Doctor of Philosophy

Structures and Composite Materials Laboratory

Department of Mechanical Engineering

McGill University, Montréal, Canada

©Nathan Hostettler - 2023

Abstract

The adoption of composite materials has become widespread across various industries, including transportation, energy, and sports, due to their lightweight advantage (specific stiffness and strength) over metals. However, the brittle nature of thermosetting matrix composites continues to raise concerns about uncontrolled crack propagation and potential catastrophic failure. In response, this research focuses on the development of a self-sensing multiscale multiphase composite material capable of tracking stress, strain and damages. This material consists of a blended matrix of unsaturated polyester (UP) and polycaprolactone (PCL), reinforced by glass fibres and industrial few-layer graphene (FLG).

First, to develop and optimize the resin system, three different unsaturated polyester resins were blended with varying amounts of polycaprolactone. The relationship between the phase-separated morphologies and the quantity of added PCL was analyzed using optical and scanning electron microscopy. The impact of the phase morphology on the toughness of the system was then assessed through single-edge-notch bending (SENB) tests. Results showed that the largest improvement in toughness was observed at compositions below the phase inversion, with as little as 2 wt% PCL, where the UP phase was continuous with a fine dispersion of the PCL. The addition of graphene to the neat resin (UP) also had a significant effect, resulting in a 96% increase in toughness at 6 wt% graphene. The combination of thermoplastic and graphene to the neat resin was found to create a self-assembly network of graphene concentrated in the UP-rich phase. This optimized composition showed a 114% improvement in toughness, resulting in a less brittle system compared to the neat resin. A tailored processing method was then developed to integrate

these resin systems into a fibreglass preform, studying the effect of fibres and pressure on the phase-separation morphology and graphene dispersion. More specifically, it was shown that fibreglass and pressure had no impact on the phase-separation morphology and that graphene filtration could be avoided choosing non-crimp fibre geometries.

Next, the impact of phase morphology on the transverse and longitudinal AC and DC electrical conductivity was evaluated for the reinforced system. The coupled effect of graphene and fibreglass significantly improved the electrical conductivity of the system by creating graphene-rich regions, effectively reducing the tunneling distance. As a result, there was a noticeable shift in the percolation threshold from 8.2 wt% graphene for the neat resin to 1.4 wt% graphene for the reinforced modified resin system ($V_f = 0.4$). The sensing capabilities (gauge factor) of the optimized composite were then evaluated under different loading modes, and a linear relationship was observed between resistivity and stress/strain in the elastic region. A simple measurement of resistivity allowed for the accurate measurement of the applied strain or stress, as well as the elastic modulus of the system. The same behaviour was shown tracking damages, with a noticeable increase in resistivity directly linked to the propagation of cracks in both static and fatigue tensile testing. Furthermore, the system's ability to localize and quantify 2D damages was successfully demonstrated using electric impedance tomography (EIT). The combination of the multiphase and multiscale approach to composite material design was proven effective in increasing the toughness, reducing the percolation threshold, and providing reliable sensing capabilities in both the elastic and plastic regimes. The developed system presents a real opportunity as well as a proof-of-concept to optimize composite parts by continuously monitoring their mechanical state throughout their lifespan.

Abrégé

L'adoption de matériaux composites s'est largement répandue à travers l'industrie notamment dans le transport, l'énergie et le sport, en raison de leur avantageuse basse densité (rigidité et ténacité spécifique) comparé aux métaux. Cependant, la nature fragile des composites à matrice thermodurcissable continue de susciter des inquiétudes quant à la propagation incontrôlée des fissures menant à une rupture complète de la pièce. En réponse à ces problèmes, cette recherche se concentre sur le développement d'un matériau composite multi-phase et multi-échelle capable mesurer les contraintes, les déformations ainsi que les dommages qu'il subit. Ce matériau consiste en une matrice composée d'un mélange de polyester non-saturé (UP) et de polycaprolactone (PCL), renforcée par une préforme de fibres de verre et de particules de graphène (FLG). Tout d'abord, le développement et l'optimisation de la résine a été conduit en testant trois résines polyesters mélangées à différentes quantités de polycaprolactone. Le lien entre les morphologies de séparation de phase et la quantité de PCL a été étudiée par microscopie optique et électronique à balayage. L'impact de ces morphologies sur la ténacité du système a ensuite été évalué à l'aide de tests de flexion sur échantillon entaillé (SENB). Les résultats ont montré que la plus grande augmentation de ténacité est obtenue à des compositions plus faible que celle de l'inversion de phase, avec aussi peu que 2 %pds de PCL, où le polyester est continue avec une fine dispersion de PCL. L'ajout de graphène à la résine de base (UP) a également un effet important, entraînant une augmentation de 96 % de la ténacité à 6 %pds de graphène. La combinaison de thermoplastique et de graphène à la résine de base crée un réseau auto-assemblé de graphène concentré dans la phase riche en polyester. Cette composition optimisée augmente la ténacité de 114 %. Une méthode

de production optimisée a été développée pour intégrer ces systèmes de résine dans une préforme en fibre de verre, étudiant l'effet des fibres et de la pression sur la morphologie de séparation de phases et sur la dispersion du graphène. Plus précisément, il a été montré que la morphologie de séparation de phases n'est pas impacté par pression et la présence de fibre, et que la filtration du graphene peut-être évitée par un choix de fibre non-tissée. L'impact de la morphologie de séparation de phase sur la conductivité électrique AC et DC, transversale et longitudinale, a été évalué pour le système renforcé. L'effet couplé du graphène et des fibres de verre améliore considérablement la conductivité électrique du système en créant des régions riches en graphène, réduisant ainsi efficacement la distance d'effet tunnel. En conséquence, un décalage notable du seuil de percolation a été observé, passant de 8.2 %pds pour la résine de base à 1.4 %pds de graphène pour la résine modifiée ($V_f = 0.4$). La capacité de détection (facteur de jauge) de ce composite a ensuite été évaluée avec différents modes de charge, et une relation linéaire a été observée entre la résistivité et la contrainte/déformation dans le region élastique. Une simple mesure de résistivité permet ainsi de mesurer avec précision la déformation ou la contrainte appliquée ainsi que le module élastique du système. Le même comportement a été observé avec des dommages plus important, ou l'augmentation de la résistivité est directement liée à la propagation des fissures lors d'essais statiques et de fatigue en traction. En outre, la capacité du système à localiser et quantifier les dommages en 2D a été démontrée avec succès en utilisant la tomographie à impédance électrique (EIT). La combinaison de l'approche multi-phase et multi-échelle pour la conception de matériaux composites s'est avérée efficace pour augmenter la ténacité, réduire le seuil de percolation et fournir une capacité de détection fiable dans les régimes élastique et plastique. Le système développé

présente ainsi une réelle opportunité ainsi qu'une preuve de concept pour optimiser les pièces composites en mesurant en continu leur état mécanique tout au long de leur durée de vie.

Acknowledgements

First and foremost, I would like to express my sincere gratitude to my supervisor, Professor Pascal Hubert, for his enthusiastic support and guidance throughout this research. It has been a great pleasure and I feel extremely fortunate to have had the opportunity to work with you during these years.

I would also like to express my gratitude to my friends and colleagues at the McGill Structures and Composite Materials Laboratory. Your friendship and support have been crucial factors in the success of this work.

Next, I would like to extend my gratitude to NanoXplore Inc. for their support throughout this research, and particularly to Dr. Giovanna Gutiérrez and Dr. Abdou Khadri Diallo for their helpful insights and feedback.

I would also like to acknowledge the financial support provided by the Werner Graupe Fellowship, the Natural Sciences and Engineering Research Council of Canada (NSERC), Prima Quebec and the Research Center for High Performance Polymer and Composite Systems (CREPEC).

Finally, thank you to my parents, my sister and my brother for their unconditional love and support in my adventures abroad. I would also like to thank my friends in Canada and Switzerland for the many adventures and laughs we have shared. Your friendship has been an essential part of my life during this time, and I am grateful for the joy and support you have brought me.

Contribution of the author

The author has performed all the work presented in this thesis with the following exceptions:

- The scanning electron microscopy (SEM) images were taken by Dr. Maryam Golozar from the McGill Electron Microscopy Research Group of Prof. Raynald Gauvin.
- The ultrasonic C-scans were performed by Olivier Arès and Julien Walter at the Aerospace Technology Centre (CTA).

Table of Contents

1. Introduction	1
1.1. Research Objectives	3
1.2. Thesis Organization	4
References	6
2. State of the Art	10
2.1. Introduction	10
2.2. Graphene-based composites	11
2.2.1. Processing methods	11
2.2.2. Interfacial properties	12
2.2.3. Mechanical properties	13
2.2.4. Electrical properties	15
2.3. Phase separation	21
2.3.1. A thermodynamic approach to phase separation	21
2.3.2. Phase separation of the UP/LPA/Styrene system	23
2.3.3. Phase separation with nanoparticles	26
2.4. Research gaps	29
References	30
3. A phase separation strategy for enhanced toughness self-assembly graphene-network composites.	38
3.1. Introduction	39

3.2. Materials and Methods	41
3.2.1. Materials	41
3.2.2. Methods	42
3.3. Results and Discussion	45
3.3.1. Phase separation and resulting morphologies	45
3.3.2. SENB and compression tests	51
3.3.3. Phase separation with graphene	54
3.3.4. Coupled effect of graphene and phase separation on toughness and yield stress	56
3.3.5. Effect of graphene network on the electrical conductivity	59
3.4. Conclusion	60
References	63
4. Processing of a multiscale multiphase composite.	68
4.1. Introduction	68
4.2. Materials and Methods	69
4.3. Results and Discussion	71
4.4. Conclusion	80
References	81
5. Electrical characterization and sensing capabilities of self-assembly multi- scale multi-phase graphene-based composites.	84
5.1. Introduction	85
5.2. Materials and Methods	86
5.2.1. Materials	86

5.2.2. Methods	87
5.3. Results and Discussion	90
5.3.1. Phase-separation morphology with fibres and graphene	90
5.3.2. DC electrical characterization	91
5.3.3. AC electrical characterization	98
5.3.4. Sensing and gauge factors	102
5.4. Conclusion	104
References	106
6. Sensing capabilities and gauge factor of a multiscale multiphase graphene-based composite.	111
6.1. Introduction	112
6.2. Materials & Methods	113
6.2.1. Materials	113
6.2.2. Methods	113
6.3. Results & Discussion	116
6.3.1. Sensing capabilities	116
6.3.2. Gauge factor	120
6.3.3. Gauge factor vs. strain rate	121
6.4. Conclusion	122
References	122
7. Multiphase multiscale graphene-based composite as intrinsic damage sensors.	125
7.1. Introduction	126
7.2. Experimental methods	127

7.2.1. Materials and Manufacturing	127
7.2.2. Fatigue testing and damage sensing	128
7.2.3. Electrical Impedance Tomography	129
7.3. Results and discussion	131
7.3.1. Tension-tension fatigue	131
7.3.2. 2D Damage localization	134
7.4. Conclusion	136
References	137
8. Conclusion	139
8.1. Original Contributions	139
8.2. Publications in Referred Journals	144
8.3. Suggestions for Future Work	144
Appendices	146
A. Molecular dynamic approach to the calculation of solubility and interaction parameters - A first look into building phase-diagrams.	148
A.1. Introduction	148
A.2. Methodology	149
A.2.1. Hildebrand solubility parameters	149
A.2.2. Flory-Huggins free energy model	150
A.3. Molecular dynamic method	152
A.3.1. Definition of the simulation box	152
A.3.2. Curing method	154

A.3.3. Cohesive energy density method	156
A.4. Results & Discussion	157
A.4.1. Curing process	157
A.4.2. Hildebrand solubility parameters	159
A.4.3. Interaction parameters and Gibbs free energy	161
A.5. Conclusion & Future work	164
References	165
B. Supplementary Materials	
A phase separation strategy for enhanced toughness self-assembly graphene-	
network composites.	169
B.1. Graphene morphology	172
C. Electrical Circuits for sensing setup	173

List of Figures

Figure 2.1. Normalized fracture toughness as a function of the filler content for graphene, carbon nanotubes and nanoclay in epoxies. [26] <i>Reproduced with permission from Elsevier.</i>	14
Figure 2.2. Fracture mechanism observed in graphene-based composites. [26] <i>Reproduced with permission from Elsevier.</i>	15
Figure 2.3. Schematic representation of the percolation theory in graphene composites.	16
Figure 2.4. Example of health monitoring: by direct resistivity measurement (left) [28] and by electrical impedance tomography (EIT) (right) [49]. <i>Reproduced with permission from [49]. Copyright 2019 American Chemical Society.</i>	20
Figure 2.5. Phase diagram representing the binodal and spinodal curves evolution with the degree of cure and the fraction of LPA.	23
Figure 2.6. SEM images of UP blends containing (a) 1%, (b) 2%, (c) 3%, (d) 4% and (e) 6% of PVAc. The phase inversion is easily observable between (b) and (d).	25
Figure 3.1. 3-point bending setup with notched sample.	44
Figure 3.2. Fractured surface showing the phase separated morphologies of Polylite 31520/PCL blends: (a) 5 wt% PCL, (b) 16.5 wt% PCL and (c) 25 wt% PCL.	47

Figure 3.3. Close-up view of the fractured surface showing the morphology of the PolyLite 31520/PCL blends: (a) 5 wt% PCL and (b) 25 wt% PCL.	48
Figure 3.4. Fractured surface showing the phase separated morphologies of PolyLite 31289/PCL blends: (a) 4 wt% PCL, (b) 7 wt% PCL and (c) 10 wt% PCL.	49
Figure 3.5. Close-up view of the fractured surface showing the morphologies of the PolyLite 31289/PCL blends: (a) 4 wt% PCL and (b) 10 wt% PCL.	50
Figure 3.6. Fractured surface showing the morphologies of the AOC R920/PCL blends: (a) 5 wt% PCL and (b) 10 wt% PCL.	50
Figure 3.7. Toughness as a function of PCL content measured from SENB tests.	53
Figure 3.8. Close-up morphologies of the AOC R920 – 5 wt% PCL.	54
Figure 3.9. Compressive yield stress as a function of the fraction of PCL.	55
Figure 3.10. PolyLite 31289 with 7 wt% PCL and 6 wt% graphene (a) before dispersion, (b) after dispersion and (c) after stabilization.	56
Figure 3.11. Toughness as a function of the fraction of thermoplastic and graphene.	58
Figure 3.12. Fractured surface of neat UP with 1 wt% of graphene showing the crack pinning mechanism.	59
Figure 3.13. Compressive yield stress as a function of the fraction of thermoplastic and graphene.	59
Figure 3.14. Electrical conductivity as a function of the PCL and graphene content.	61
Figure 4.1. Square mould used for the processing of the plates (the front part was removed for the picture). [9]	71

Figure 4.2. (a) pressure evolution during processing and optical microscopy images of the plate (b) 40 °C without shim, (c) 40 °C with shim.	73
Figure 4.3. Schematic for the measurement of R_{tow}	73
Figure 4.4. Degree of impregnation as a function of time and applied pressure.	74
Figure 4.5. (a) pressure evolution during processing and optical microscopy images of the plate with a zero-thickness at 12 MPa (b) cold pressed with shim, (c) 40 °C with shim.	75
Figure 4.6. Microscopy image of a UP – 8 wt%PCL.	77
Figure 4.7. Microscopy images (a) UP – 4 wt% PCL without fibres, (b) UP-7 wt% PCL without fibres, (c) UP - 4 wt% PCL with fibres, (d) UP - 7 wt% PCL with fibres.	77
Figure 4.8. Microscopy images (a) UP–8 wt% gf with the complex fibre architecture (b) UP–8 wt% gf with the weave fibre architecture.	79
Figure 4.9. Microscopy image of UP – 4 wt% PCL and 8 wt% gf.	79
Figure 5.1. Optical microscopy of polished samples: (a) UP 8 wt% graphene (b) UP 8 wt% PCL and (c) UP 6 wt% graphene and 4 wt% PCL. (A high-resolution version of these images for use with the Virtual Microscope is available as eSlide: (a) VM06778 (b) VM06779 (c) VM06781)	92
Figure 5.2. (a) Transverse and (b) longitudinal DC electrical conductivity.	94
Figure 5.3. Fitted DC electrical conductivity its second derivative for a sample without PCL measured in the (a) transverse and (b) longitudinal direction.	95

- Figure 5.4. Optical microscopy images: (a) UP 6 wt% graphene and 2 wt% PCL - the fine darker dots are the PCL-rich phase and the lighter round are the glassfibres [17], (b) UP 6 wt% graphene and 4 wt% PCL. (A high-resolution version of these images for use with the Virtual Microscope is available as eSlide: (a) VM06782 (b) VM06783) 96
- Figure 5.5. Schematic of the phase separated microstructure of UP blends with (a) 2 wt% (b) 4 wt% (c) 6 wt% and (d) 8 wt% of PCL. The PCL-rich phase is orange, the UP-rich phase yellow and the graphene black. 96
- Figure 5.6. Evolution of the measured current as a function of the applied voltage: (a) neat UP with increasing quantity of graphene. (b) Blend of UP – 3 wt% gf with 2 and 4 wt% PCL slightly above and below the percolation threshold, respectively. (c) UP – 6 wt% gf with increasing quantity of PCL. 99
- Figure 5.7. AC frequency sweep: (a) neat UP with increasing quantity of graphene. (b) blend of UP-8 wt%gf with increasing quantity of PCL. 102
- Figure 5.8. (a) Evolution of the deformation, force and resistivity during a cyclic sensing tests in compression for UP – 6 wt%gf 2 wt%PCL. (b) Gauge factor as a function of graphene and PCL content. 104
- Figure 6.1. Resistance evolution with an applied load of 0.75kN and different load amplitudes (top right inserts) for: (a) 3-point bending, (b) 4-point bending and (c) traction. 118
- Figure 6.2. Resistivity evolution with (a) applied load and (b) applied strain. 119
- Figure 6.3. Evolution of the gauge factor as a function of the strain rate for the traction sample both in traction and compression. 121

Figure 7.1. Plate investigated by electrical impedance tomography (from left-to-right): reference plate, drilled and impacted.	129
Figure 7.2. Current injection method, FEM and EIT concept.	131
Figure 7.3. (a) Static tensile testing of the system showing the Stress vs. time curve (black) and the relative change in resistivity (orange) during the test, vertical dashed lines show crack propagations. (b) Fatigue Stress vs. Strain hysteresis comparing the change in slope between the 1 st , 250 th and 500 th cycle. (c) Relative evolution of the resistivity around the 1 st , 250 th and 500 th cycle. (d) Evolution of the local average resistivity and local average strain during fatigue testing, the vertical lines show the crack propagation. (e) Effect of the testing frequency in the gauge factor (GF). (f) Effect of the relative stress amplitude on the gauge factor.	133
Figure 7.4. Comparison between ultrasonic C-scan and EIT for (a) drilled and (b) impacted plate.	135
Figure A.1. Molecules created in Chem3D: (a) UP (n=1), (b) St and (c) PCL (n=30)	153
Figure A.2. Flowchart - Creation of the simulation box.	153
Figure A.3. Curing method 1 in LAMMPS.	155
Figure A.4. Optimized curing method in LAMMPS.	156
Figure A.5. Evolution of the cluster size with the degree of cure for UP (n=2). . .	158
Figure A.6. Evolution of the interaction parameter with the initial molar mass of UP and degree of cure at 25, 50 and 75°C.	162
Figure A.7. Evolution of the interaction parameter as a function of 1/T for different initial molar mass of UP and degree of cure.	163

Figure A.8. Temperature phase-diagram for UP(n=4)/PCL blends at varying degree of cures.	164
Figure B.1. close-up view of graphite residues in a 2wt% graphene sample. . . .	172
Figure B.2. size distribution histogram.	172
Figure C.1. 2-point equivalent electrical circuit and plugging procedure for the resistivity measurement used for strain and damage sensing. Note that no shielding was used in the context of this work. Adapted from the " <i>Keithley Model 6517A Electrometer User's Manual</i> " (2014).	173

List of Tables

Table 3.1. Quantity of PCL required to reach the critical composition.	51
Table 4.1. Details of the fibre nominal superficial density, stack and target thickness for $V_f = 0.4$	71
Table 4.2. Parameters used in the tow impregnation model.	74
Table 5.1. Transverse and longitudinal percolation threshold as a function of the PCL content.	97
Table 6.1. Comparison between the elastic modulus calculated from the resistivity and from the strain data.	120
Table 6.2. Average gauge factor over the whole force range for the three-loading mode.	121
Table 7.1. Elastic modulus and relative change in resistivity at different testing cycles.	132
Table A.1. Calculated and literature Hildebrand solubility parameters for PCL ($n=30$) and Styrene.	159
Table A.2. Evolution of the solubility parameters of UP as a function of the molar mass, degree of cure and temperature	160
Table B.1. Detailed results for the PolyLite 31520.	169
Table B.2. Detailed results for the AOC R920.	169

Table B.3. Detailed results for the Polylite 31289. 170

Table B.4. Detailed results of the Polylite 31289 with graphene. 170

CHAPTER 1

Introduction

The use of composite materials has been the norm for several years now in many different fields like transportation, energy, construction or sport as a lightweight alternative to metals and ceramics. The greener perspective offered by the reduced weight and flexibility of processing is, however, foreshadowed by high maintenance costs and poor end-of-life management. The brittle nature of the thermoset matrix makes it prone to uncontrolled crack propagations possibly leading to a catastrophic failure, if not repaired on time. To avoid such event, downtime for part inspections and repairs are numerous with a total budget expected to reach 22 Bn\$ worldwide by 2026 [1]. When the part is not repaired on time, it is usually disposed in landfills with a strong impact on the environment (more than 40'000 tons in France for 2015 only [2]). The size of the global composite market was about 90 Bn\$ in 2019 and is expected to continue expanding with a growth rate of 7.6% reaching 160 Bn\$ by 2027, the amount of repairs and landfilled composite parts is meant to increase accordingly [3]. Efforts are being done to reduce the amount of part landfilled by recycling or repurposing but it is also by optimizing the damage detection during the part's life that we can optimize repair and reduce the amount of discarded parts. There is a need to find a cost efficient, easy and reliable way to control and track the extend of damage of structures to ease repair and reduce material waste. This is known as structural health monitoring (SHM) which uses a physical signal (e.g. magnetic optical, ultrasonic, acoustic capacitive, piezoresistive, etc.) to probe the extend of damage in a part [4], this is

usually done by hand in a slow and tedious process. More recently, efforts were made to develop smart structures that integrate sensors and actuation systems on their surface or directly within their structure. Compared to previous methods, smart structures have the advantage to autonomously monitor the health conditions and are more predictive without associated downtimes. The sensing capabilities of surface sensors are limited and give no information on the internal condition of the part, unable to monitor micro-cracks growth. This was solved by embedding the sensors within the thermoset matrix or sandwich structure [5]. Different technologies generally based on fibre optics [6] or piezoelectric PZT transducers [5, 7] were found efficient to probe the progression of damage within a part, and are now widely used in aerospace, automobile and construction. Despite being efficient to track damage, they introduce non-structural defects in the material that can act as a preferential site for crack growth [8]. The last type of smart structures are self-sensing materials, capable of sensing their own health through piezoresistive principle, by integrating a conductive element within their composition. This approach was successful with carbon fibres and allowed to identify the location of a damage [9, 10]. The detection is, however, limited to fibre damages. The use of nano-materials like graphene, carbon nanotubes (CNTs) or carbon black (CB) were found successful in tracking the strains and damages in the polymer matrix, allowing a direct monitoring of its conditions during a static or cyclic solicitation by direct resistivity measurement [11–16] or after an impact by Electrical Impedance Tomography (EIT) [17–20]. The use of graphene offers a greater flexibility in comparison to other carbon-based filler including safer handling compared to nano-carbon black [21], and ease to disperse and process compared to carbon nanotubes. However, sensing application typically uses either

monolayer chemical vapor deposition (CVD) graphene or advanced processing method (fibre coating, filament winding, etc...). As an alternative, few-layer graphene (FLG) is required in larger amounts to reach the conductivity threshold, which in turn reduces the processability and mechanical properties of the part. Prior research has shown that by blending the thermoset resin with a thermoplastic, it is possible to create a self-assembly network of nanoparticles [22–24]. The phase-separation resulting from these blends can create a double percolation effect by localizing the graphene in only one of the two resulting phase effectively lowering the quantity of graphene needed for conduction [25]. These studies, however, lack in describing the coupled effect of graphene and phase morphology on the mechanical and electrical properties, and focus on system without continuous fibre reinforcements. These blends are especially common with unsaturated polyester where they are already used to control the cure shrinkage [26], hence their choice for such application. More details on the specific properties of a wide variety of nanocomposites polymers are found in the literature, for example [27, 28].

1.1. Research Objectives

The general objectives of this research is to develop a self-sensing multiscale multiphase composite. In other words, a composite material reinforced by both glass fibre and few-layer graphene in a phase-separating matrix that has the capacity to monitor its health. More specifically, the sub-objectives of this work are:

1. Develop a phase-separating system composed on a blend of unsaturated polyester (UP) and polycaprolactone (PCL), that optimize the quantity of few-layer graphene (FLG) needed to maximize the toughness and electrical conductivity.

2. Study and optimize the processing of this system by compression resin transfer moulding in a fibreglass preform.
3. Study the coupled effect of graphene, phase-separation and fibres on the DC and AC electrical conductivity.
4. Study the sensing capabilities of the optimized system in tracking strain and damage.

1.2. Thesis Organization

CHAPTER 2 defines the areas of interest of this research and reviews the current knowledge of the different aspects of this work. The gaps in the literature that this work addresses are highlighted.

CHAPTER 3 presents the development of several UP/PCL phase-separating systems and their resulting morphologies. The impact of these morphologies on the toughness is studied by single-edge-notch bending (SENB), to find the composition leading to the highest toughness increase with the lowest quantity of PCL. The presence of a secondary-phase separation and its effect on the resulting toughness increase is shown. In a second step, varying quantities of FLG is added and their coupled effect, together with the phase morphology, on the toughness and threshold of electrical conduction is studied. The creation of a self-assembly network of graphene in the UP phase is highlighted.

CHAPTER 4 study and optimize the processing of such system in a fibreglass preform by compression resin transfer moulding. A tow impregnation model is used to optimize the pressure profile. The problematic of graphene filtering is addressed as well as the potential effect of fibres and pressure on the phase-separated morphology.

CHAPTER 5 aims at better understanding the transverse and longitudinal electron flow in

such multiscale multiphase system. The mechanisms leading to the shift in DC electrical conductivity threshold linked to the phase morphology are discussed. The current–voltage behaviour is used to show the tunnelling effect presence at low quantities of graphene. The AC conductivity behaviour is also studied and linked to the phase–morphologies. Finally, the gauge factor is introduced and the strain sensing capabilities of the system are discussed.

CHAPTER 6 study the strain and stress sensing capabilities of the developed system in traction, 3– and 4–point bending. The link between electrical resistivity and elastic modulus is shown. The difference in shape of the electrical response to the different solicitation mode is explained and linked to the position of the neutral axis. The influence of the testing speed on the sensing capabilities is also studied.

CHAPTER 7 focuses on the damage sensing capabilities of the system in traction–traction fatigue, where the link between crack growth and resistivity baseline is shown. The effect of stress amplitude and testing frequencies are investigated. The 2D damage localization capabilities by Electrical Impedance Tomography (EIT) are discussed on two types of damage (impacts and drilled holes) and compared to ultrasonic C-scans.

Finally, CHAPTER 8 presents the conclusions and original contributions arising from this work, as well as some possible future works that can be conducted as an extension of the presented research.

A supplementary chapter on the molecular dynamic simulation of the phase separation, supplementary information as well as electrical measurement schematics are included in the APPENDIX.

References

- [1] MarketsAndMarkets. Composite Repairs Market by Type (Structural, Semi-Structural, Cosmetic), Process (Hand Lay-Up, Vacuum Infusion, Autoclave), End-Use Industry (Aerospace & Defense, Wind Energy, Automotive & Transportation), and Region - Global Forecast to 2026. 2017.
- [2] JEC-GROUP. Overview of the global composites markets: at the crossroads. 2017.
- [3] Georgia Chatziparaskeva, Iliana Papamichael, Irene Voukkali, Pantelitsa Loizia, Georgia Sourkouni, Christos Argirusis, and Antonis A. Zorpas. End-of-Life of Composite Materials in the Framework of the Circular Economy. *Microplastics*, 1(3):377–392, 2022.
- [4] Sahar Hassani, Mohsen Mousavi, and Amir H. Gandomi. Structural health monitoring in composite structures: A comprehensive review. *Sensors*, 22(1):1–45, 2022.
- [5] M. Dziendzikowski, A. Kurnyta, K. Dragan, S. Klysz, and A. Leski. In situ Barely Visible Impact Damage detection and localization for composite structures using surface mounted and embedded PZT transducers: A comparative study. *Mechanical Systems and Signal Processing*, 78:91–106, 2016.
- [6] Manjusha Ramakrishnan, Ginu Rajan, Yuliya Semenova, and Gerald Farrell. Overview of fiber optic sensor technologies for strain/temperature sensing applications in composite materials. *Sensors (Switzerland)*, 16(1), 2016.
- [7] Hong Yue Tang, Charles Winkelmann, Wahyu Lestari, and Valeria La Saponara. Composite structural health monitoring through use of embedded PZT sensors. *Journal of Intelligent Material Systems and Structures*, 22(8):739–755, 2011.
- [8] Hari P. Konka, M. A. Wahab, and K. Lian. On mechanical properties of composite sandwich structures with embedded piezoelectric fiber composite sensors. *Journal of Engineering Materials and Technology*, 134(1):1–12, 2012.
- [9] Helena Rocha, Christophe Fernandes, Nelson Ferreira, Ugo Lafont, and João P. Nunes. Damage localization on CFRP composites by electrical impedance tomography. *Materials Today Communications*, 32(July), 2022.
- [10] Susanne Nonn, Martin Schagerl, Yingjun Zhao, Sandra Gschossmann, and Christoph Kralovec. Application of electrical impedance tomography to an anisotropic carbon fiber-reinforced polymer composite laminate for damage localization. *Composites Science and Technology*, 160(February):231–236, 2018.
- [11] Erik T. Thostenson and Tsu Wei Chou. Real-time in situ sensing of damage evolution in advanced fiber composites using carbon nanotube networks. *Nanotechnology*, 19(21), 2008.
- [12] Pawan Verma, Jabir Ubaid, Kartik M. Varadarajan, Brian L. Wardle, and S. Kumar. Synthesis and Characterization of Carbon Nanotube-Doped Thermoplastic Nanocomposites for the Additive Manufacturing of Self-Sensing Piezoresistive Materials. *ACS Applied Materials and Interfaces*, 14(6):8361–8372, 2022.

- [13] Ayako Yoshida, Yi-Fei Wang, Tomohito Sekine, Yasunori Takeda, Daisuke Kumaki, and Shizuo Tokito. Printed Low-Hysteresis Stretchable Strain Sensor Based on a Self-Segregating Conductive Composite. *ACS Applied Engineering Materials*, 2022.
- [14] Hu Liu, Yilong Li, Kun Dai, Guoqiang Zheng, Chuntai Liu, Changyu Shen, Xingru Yan, Jiang Guo, and Zhanhu Guo. Electrically conductive thermoplastic elastomer nanocomposites at ultralow graphene loading levels for strain sensor applications. *Journal of Materials Chemistry C*, 4(1):157–166, 2015.
- [15] Jingwen Chu, Alexander J. Marsden, Robert J. Young, and Mark A. Bissett. Graphene-Based Materials as Strain Sensors in Glass Fiber/Epoxy Model Composites. *ACS Applied Materials and Interfaces*, 11(34):31338–31345, 2019.
- [16] Hu Liu, Qianming Li, Shuaidi Zhang, Rui Yin, Xianhu Liu, Yuxin He, Kun Dai, Chongxin Shan, Jiang Guo, Chuntai Liu, Changyu Shen, Xiaojing Wang, Ning Wang, Zicheng Wang, Renbo Wei, and Zhanhu Guo. Electrically conductive polymer composites for smart flexible strain sensors: a critical review. *Journal of Materials Chemistry C*, 6(45):12121–12141, 2018.
- [17] A. J. Thomas, J. J. Kim, T. N. Tallman, and C. E. Bakis. Damage detection in self-sensing composite tubes via electrical impedance tomography. *Composites Part B: Engineering*, 177(June):107276, 2019.
- [18] Hongbo Dai and Erik T. Thostenson. Large-Area Carbon Nanotube-Based Flexible Composites for Ultra-Wide Range Pressure Sensing and Spatial Pressure Mapping. *ACS Applied Materials and Interfaces*, 11(51):48370–48380, 2019.
- [19] Fuchao Hao, Shaokai Wang, Fei Xing, Min Li, Tianshu Li, Yizhuo Gu, Wei Zhang, and Jiahui Zhang. Carbon-Nanotube-Film-Based Electrical Impedance Tomography for Structural Damage Detection of Carbon-Fiber-Reinforced Composites. *ACS Applied Nano Materials*, 4(5):5590–5597, 2021.
- [20] Jinwon Oh, Jun Chang Yang, Jin Oh Kim, Hyunkyu Park, Se Young Kwon, Serin Lee, Joo Yong Sim, Hyun Woo Oh, Jung Kim, and Steve Park. Pressure insensitive strain sensor with facile solution-based process for tactile sensing applications. *ACS Nano*, 12(8):7546–7553, 2018.
- [21] Nima Moghimian and Soroush Nazarpour. The future of carbon: An update on graphene’s dermal, inhalation, and gene toxicity. *Crystals*, 10(9):1–6, 2020.
- [22] Xue Wang, Weizhen Li, Zhao Zhang, Kaimin Chen, and Wenjun Gan. Selective localization of multi-walled carbon nanotubes in epoxy/polyetherimide system and properties of the conductive composites. *Journal of Applied Polymer Science*, 136(35):1–10, 2019.
- [23] Emna Helal, Rafael S. Kurusu, Nima Moghimian, Giovanna Gutierrez, Eric David, and Nicole R. Demarquette. Correlation between morphology, rheological behavior, and electrical behavior of conductive cocontinuous LLDPE/EVA blends containing commercial graphene nanoplatelets. *Journal of Rheology*, 63(6):961–976, 2019.

- [24] Hajime Kishi, Sanae Tanaka, Yasuaki Nakashima, and Takashi Saruwatari. Self-assembled three-dimensional structure of epoxy/polyethersulphone/silver adhesives with electrical conductivity. *Polymer*, 82:93–99, 2016.
- [25] A. J. Marsden, D. G. Papageorgiou, C. Vallés, A. Liscio, V. Palermo, M. A. Bissett, R. J. Young, and I. A. Kinloch. Electrical percolation in graphene-polymer composites. *2D Materials*, 5(3), 2018.
- [26] Clive B. Bucknall, Peter Davies, and Ivana K. Partridge. Phase separation in styrenated polyester resin containing a poly(vinyl acetate) low-profile additive. *Polymer*, 26(1):109–112, 1985.
- [27] Jeffrey Jordan, Karl I. Jacob, Rina Tannenbaum, Mohammed A. Sharaf, and Iwona Jasiuk. Experimental trends in polymer nanocomposites - A review. *Materials Science and Engineering A*, 393(1-2):1–11, 2005.
- [28] S. C. Tjong. Structural and mechanical properties of polymer nanocomposites. *Materials Science and Engineering R: Reports*, 53(3-4):73–197, 2006.

PREFACE – CHAPTER 2

The following chapter presents the relevant literature review for each of the fundamental aspects of this work. Graphene and graphene-based composites are first introduced. The effect of graphene on the mechanical and electrical properties of the resin system is presented as well as the resulting sensing capabilities. The concept of phase separation in unsaturated polyester is then presented and the addition of nano-particles in such system is discussed. Finally, the literature review is analyzed and the research gaps with which this research is concerned are highlighted. Note that a specific literature review is also found in the introduction of each published chapters.

CHAPTER 2

State of the Art

2.1. Introduction

Graphene is a 2D sp^2 hybridized network of carbon atoms that was first discovered in 2004 at the University of Manchester [1]. It has since then broken the laboratory barrier and reached the industrial scale especially with the big push and mass production of the Chinese industry [2]. The material that was originally produced by mechanical exfoliation with a simple scotch tape technique can now be obtained in large quantities and even at large surface dimensions ($20 \times 20 \text{ cm}^2$) through continuous chemical vapour deposition. This still growing interest is mostly due to its intrinsic properties that have largely exceeded what could be obtained by any other materials with an elastic modulus up to 1 TPa and an intrinsic strength of 130 GPa [3] compared to only ~ 100 GPa and ~ 1000 MPa [4], respectively, for carbon reinforced composites. It also shows an impressive electrical conductivity of 10^8 S/m [5] ($\sim 10^7 \text{ S/m}$ for pure silver [6]) and many other specificities as the ability to be infinitely tuned by chemical functionalization as well as a high specific surface area (calculated value of $2630 \text{ m}^2\text{g}^{-1}$ [7]). These properties leaves only imagination as a limit to the possible application of graphene, a promising one being its use as a filler in fibre reinforced plastics (FRPs). There is, however, still a fear in using such material because of the brittle nature of its thermosetting matrix, leading to uncontrolled crack propagations and to catastrophic failure. The use of graphene coupled

with phase separation would be a solution to that issue, linking the toughness increase of both graphene and phase separation, and allowing the live tracking of defect formation by continuous resistivity measurements. However, when studies on graphene-based composites are already numerous, there is still work to be done especially regarding its integration in fibre reinforced thermosetting resin for structural application, its use in phase separating systems and its capacity as a strain and stress sensor. The present literature review first focuses on the key processing parameters, and the resulting properties and enhancement mechanisms on graphene-based composites, as well as their sensing capabilities. The second part focuses on the phase separation phenomenon in thermosetting resin by addition of a low profile additive (LPA) and the effect of nanoparticles in such systems.

2.2. Graphene-based composites

2.2.1. Processing methods

The key parameter when manufacturing graphene bulk nanocomposites is to ensure that the graphene is homogeneously dispersed in the matrix. A good dispersion coupled with high quality graphene (fewest carbon layer and lowest oxygen to carbon ratio possible) will lead to the best mechanical reinforcement and increase of electrical and thermal conductivity. The aspect ratio of the filler as well as the nature of its interface with the matrix are other key parameters in the design of graphene nanocomposites [8]. Because of its high surface area, graphene has a tendency to form aggregates (or agglomerates) which critically reduces the mechanical, electrical and thermal properties of the resulting material. Different strategies exist to mix and disperse the filler across the matrix, the main

ones being sonication, shear mixing and three roll mill or calendar process [9]. The three main methods followed to integrate the filler in the matrix are solution compounding, *in situ* polymerization and melt mixing. Some other more exotic processing techniques involve coating the fibres with graphene before the composite processing, leading to a highly organized network of conductive reinforcement [10, 11]. The integration as well as the different mixing techniques are well documented in many reviews [8, 12–16] and won't be further discussed here.

2.2.2. Interfacial properties

The final dispersion of graphene is key to obtain a good reinforcement as well as a low percolation threshold. The dispersion can be improved by reducing the Van der Waals interactions between the carbon layers and increasing the affinity of the filler with the matrix. This is usually done via covalent (direct modification of the graphene) or by noncovalent functionalization (addition of surfactants, ionic liquids, etc...) [17]. The covalent functionalization of graphene increases the graphene-matrix chemical affinity and bonding by decorating the graphene sheet with functional groups [9, 18–20]. These groups are specially chosen for their affinity with the used polymer and should be adapted for each different matrices. The functionalization of graphene oxide (GO) is facilitated by the presence of epoxide and hydroxyl group on the basal plane of the sheet, appearing during the processing of GO from elemental graphite via the Brodie, Staudenmeirer or Hummers method. [7, 21]. In the case of noncovalent functionalization, the use of surfactants can prevent the restacking of graphene sheets by increasing its solubility and compatibility with the solvent or polymer. That usually lead to an increased interface quality enhancing the mechanical properties of the final material. Triton X-100 is an example of used

surfactant of high dispersion power due to its benzene ring enhancing the adsorption of the nanomaterial by $\pi - \pi$ interactions [9]. The use of surfactant usually causes less damage to the graphene than classic functionalization, avoiding any disruption of the 2D sp^2 network electronic properties [17]. The characterization of these interactions are problematic as there is no easy method to directly measure their intensity. The research studying this phenomenon usually uses simulation tools as molecular dynamic calculation to simulate the interface properties [22].

2.2.3. Mechanical properties

The addition of graphene usually has a positive effect on the mechanical properties of the polymer. The presence of high modulus graphene highly increases the elastic modulus of the resin, sometimes even up to 200 % the initial value with 5 vol% of graphene for thermoplastic polyurethane (TPU) [23]. For thermosetting resin as epoxy, the reported values are usually close to 8-10% of increase for 1 wt% of filler loading [24]. When the increase of modulus is usually observed, it is not always the case for tensile and flexural strength where the addition of filler can even lead to a reduction of the properties compared to the neat resin value [25]. The addition of graphene was shown to affect the failure mechanisms of the material, usually interestingly increasing the fracture toughness. However, this effect is strongly linked to the quality of the graphene flakes and on the quality of the dispersion. The variety of graphene and dispersion techniques found in the literature lead to a large spread of its effect on the toughness (see Figure 2.1).

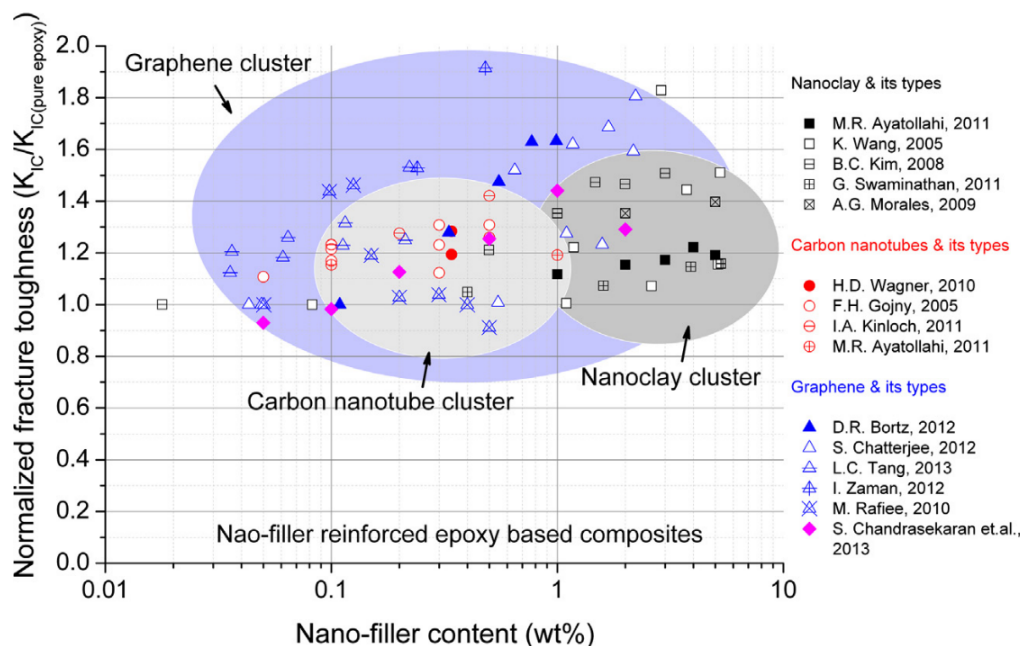


Figure 2.1: Normalized fracture toughness as a function of the filler content for graphene, carbon nanotubes and nanoclay in epoxies. [26] *Reproduced with permission from Elsevier.*

Two main fracture mechanisms can be isolated [26]: (i) crack pinning and (ii) crack deflection and separation between the graphene layers. In the first case, when the crack encounters a graphene nanoplatelet oriented perpendicularly to its propagation, it will bifurcate to avoid the particle increasing the tortuosity and the fracture toughness. In the second case, the crack encounters a graphene nanoplatelet parallel to its sheets, as the van der Waals forces between the graphene sheets are weak, the crack propagates in between the layers reducing the local fracture toughness. This second mechanism becomes facilitated when the quantity of filler is increased (> 2 wt% in [26]), justifying the reduction of toughness at higher filler loading. Reported values show an increase of the compressive failure strength and toughness by 48 and 1185 %, respectively, at a graphene loading of only 0.0275 wt% [27].

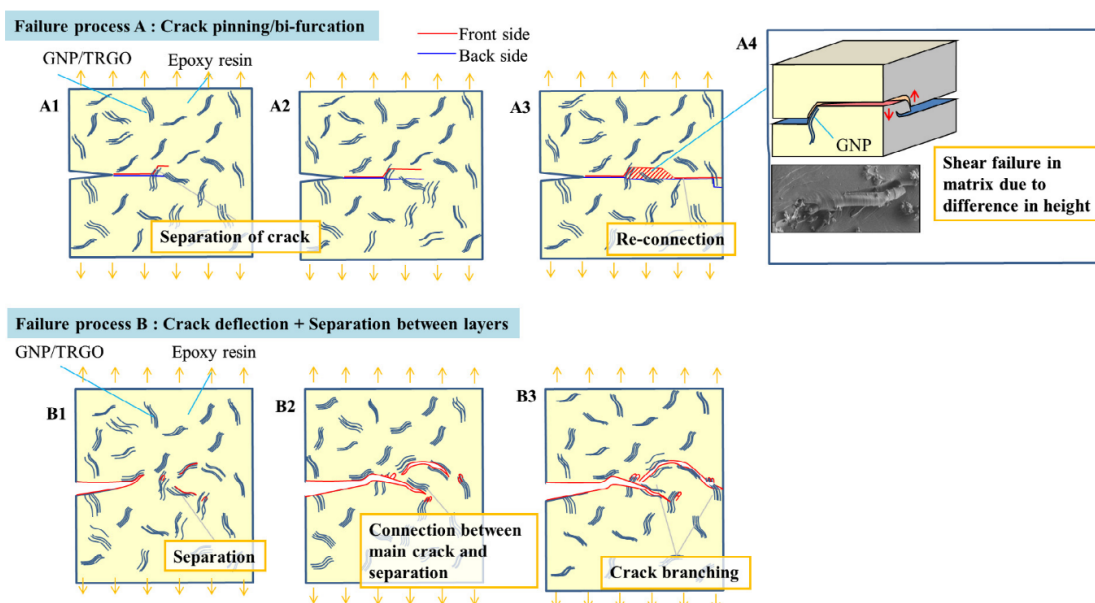


Figure 2.2: Fracture mechanism observed in graphene-based composites. [26] *Reproduced with permission from Elsevier.*

2.2.4. Electrical properties

Fundamentals of electrical conduction in graphene-based composites

The principle for electrical conduction in graphene-based composites is mainly based on the percolation theory which defines the minimum particle mass fraction (percolation threshold p_c) needed to form an electron-conductive network [28]. Three main stages are observed: (i) insulating, where no direct network of filler is present, precluding any charge flow (ii) conductive, where a direct network of filler leads to conduction and (iii) percolating. In the latter, there is no direct contact between the filler, but conduction is still possible via tunneling effect through an interface formed between the filler and the matrix [29]. This effect depends on the configuration of the percolating network (from homogeneously dispersed to aggregated) and the number of available electron-conducting path (direct or at tunneling distance). Parameters which in return depend on the properties of the constituent materials as the filler size, aspect ratio and curvature, as well as the

viscosity of the matrix. Finally, the processing of the materials also play a key role for percolation, having a strong influence on the quality of the dispersion [30]. In most of the case, the evolution of electrical conductivity σ is described as a power-law following:

$$\sigma \propto (p - p_c)^t \quad (2.1)$$

with p and p_c the effective and percolation mass fraction of filler and t the conductivity exponent which only depends on the network dimensionality. This model applies to mass fraction above but close to the percolation threshold in which the critical fluctuation extends over distances much larger than of the constituents.

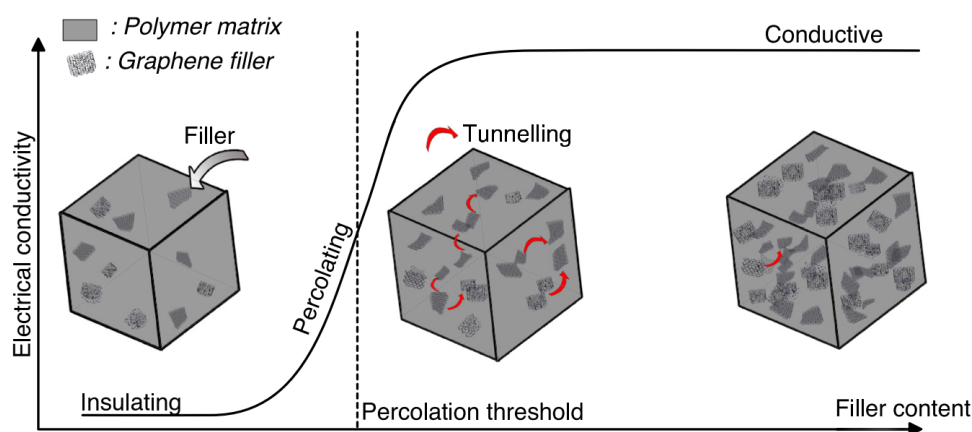


Figure 2.3: Schematic representation of the percolation theory in graphene composites. [28] *Reproduced with permission from [28].*

The measured percolation threshold and electrical conductivity is usually inconsistent between different researches because of the large variety of filler quality (C/O ratio, number of layers, aspect ratio, etc...) as well as the used processing methods and resulting dispersion enhancing or not the measured properties. On the few researches conducted on thermosetting resin, epoxy/graphene based materials are the most dominant and show a percolation threshold and ultimate DC electrical conductivities ranging from 10^{-6} S/m at

0.16 vol% to 10 S/m at 4 vol% of graphene [28]. When for thermoplastics, as polylactic acid (PLA), it ranges from 0.01 S/m at 0.004 vol% to 0.1 S/m at 0.75 vol% of graphene [28]. The difference between thermoplastics and thermosets is probably coming from the range of dispersion degree available. Another study by Sarker *et al.* studied the effect of graphene nano-platelets in epoxy/glass fibre composite. The measurement found a rather high percolation threshold and low maximal conductivity (8 wt% and 10^{-3} S/m respectively), the addition of a large fraction of insulating glass fibre highly reducing the conductivity of the final material.

Gauge factor and Sensing capabilities

The electrical conduction in conductive particle-filled composite materials is a function of the number of existing electron-paths throughout the network (mostly by percolation at low filler content). By creating or destroying these paths with an applied strain, it is possible to track the deformation of the material from a measure of resistivity especially in the percolating region [28]. Two main effects are usually observed: under an applied strain, the graphene stretches and wrinkles within the matrix which breaks conductive pathways and increases the tunneling distance. At the same time, new pathways are created having only a marginal effect on the overall change of resistance, the breaking of pathways being predominant [31]. The most common way to measure the sensitivity of the sensing system is through the gauge factor:

$$GF = \frac{R/R_0}{\varepsilon} \quad (2.2)$$

where R and R_0 are the strained and unstrained resistance respectively and ε the applied

strain, usually low. The larger the gauge factor, the higher the sensitivity of the system. The highest values of GF for graphene loaded epoxy usually goes up to 20 – 50 [32, 33], when for metal based sensor, GF is typically close to 2 [34]. When the described effects are usually accepted as the main ones, the piezoresistivity of the carbon filler should not be neglected. It was demonstrated that large aspect ratio particles show an interdependence between intrinsic electrical resistance and strain non-marginally affecting the conductivity [30].

Several techniques were studied to efficiently incorporate graphene in resin system and study its sensing capabilities by direct resistivity measurement (see Figure 2.4). The most common strategy is to incorporate CVD graphene as a thin film on top or embedded inside the system [28, 35–37]. While this strategy showed a good reliability to probe strain, its probing capabilities is limited to the vicinity of the film, giving no information on the rest of the system. Another strategy is to directly coat the reinforcement or textile with graphene [38–41], which leads to a better monitoring of the overall health of the part. Only few studies were conducted on graphene-based resin with a continuous reinforcement, due to the high tendency of graphene particles for filtering. In such cases, the part was usually produced by hand layup to ensure a homogeneous repartition of the graphene throughout the system [42]. For these applications, CVD graphene is usually preferred to platelets because of its higher intrinsic conductivity [39], as few-layer graphene is usually needed in much larger amount (> 10 wt% [42–44]) for health monitoring, making the processing in a fibre preform extremely challenging.

Direct resistivity measurement is only one of the possible method used to measure strain and damage with a conductive filler. Recently, one especially interesting method started

to be used with conductive reinforcement or conductive filler called electrical impedance tomography (EIT) [45–52] (see Figure 2.4). This non-invasive method, originally used in the medical field, uses boundary resistivity measurement to reconstruct a 2D electrical conductivity distribution of the measured system, the calculation method is described in what follows [53, 54]. Assuming a square plate and using n_e electrodes, n_v differential measurement per electrode leading to $n_M = n_e n_n$ data points, each data frame measures a vector $\mathbf{v} \in \mathbb{R}^{n_M}$. The difference EIT calculates \mathbf{y} the data difference between the virgin plate and damaged one as $[\mathbf{y}]_i = [\mathbf{v}_2]_i - [\mathbf{v}_1]_i$. The plate is modelled by finite element method (FEM) into n_N discrete elements represented by a conductivity vector $\boldsymbol{\sigma} \in \mathbb{R}^{n_N}$. Here again, difference EIT calculates the difference in conductivity between tested and reference plate as $\mathbf{x} = \boldsymbol{\sigma}_2 - \boldsymbol{\sigma}_1$. For small differences, the relationship between \mathbf{x} and \mathbf{y} can be linearized giving the EIT forward model as [53–55]:

$$\mathbf{y} = \mathbf{J}\mathbf{x} + \mathbf{n} \quad (2.3)$$

where $\mathbf{J} \in \mathbb{R}^{n_M \times n_N}$ and $\mathbf{n} \in \mathbb{R}^{n_M}$ are the Jacobian, also called sensitivity matrix, and the noise of the measurement, respectively. The Jacobian is calculated from the FEM as $\mathbf{J}_{ij} = \left. \frac{\partial y_i}{\partial x_j} \right|_{\sigma_1}$. It depends on the current injection pattern, initial conductivity and electrodes system. The calculation of the temporal inverse is a numerical problem that can be solved using the Gauss–Newton (GN) inverse. This reconstruction method calculates the inverse solution $\hat{\mathbf{x}}$ expressed as the minimum of a sum of quadratic norms:

$$\|\mathbf{y} - \mathbf{J}\hat{\mathbf{x}}\|_{\Sigma_n}^2 + \|\mathbf{x} - \mathbf{x}^\circ\|_{\Sigma_x}^2 \quad (2.4)$$

where $\mathbf{x}^\circ = 0$, the expected value of conductivity change in difference EIT, $\Sigma_n \in \mathbb{R}^{n_M \times n_M}$ is the noise covariance matrix and $\Sigma_x \in \mathbb{R}^{n_N \times n_N}$ the expected image covariance. The linearized one-step inverse solution can then be written as:

$$\hat{\mathbf{x}} = (\mathbf{J}^T \mathbf{W} \mathbf{J} + \lambda^2 \mathbf{R})^{-1} \mathbf{J}^T \mathbf{W} \mathbf{y} \quad (2.5)$$

where $\mathbf{W} = \sigma_n^2 \Sigma_n^{-1}$ and $\mathbf{R} = \sigma_x^2 \Sigma_x^{-1}$, with σ_n the average measurement noise amplitude and σ_x the amplitude of conductivity change. Finally, λ is the hyperparameter controlling the trade-off between resolution and noise attenuation in the reconstructed image [53]. The reconstructed image then represents the local changes in conductivity of the damaged plate compared to the reference one (see Figure 2.4).

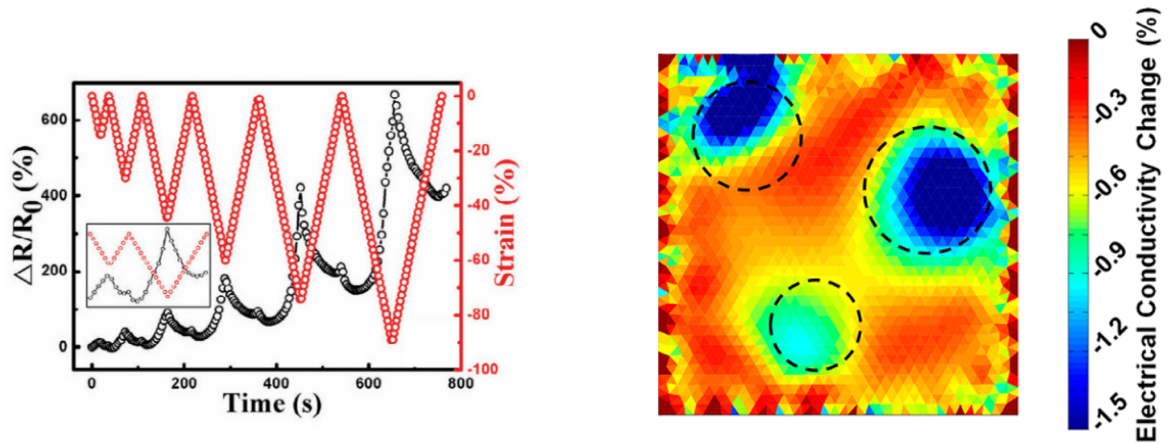


Figure 2.4: Example of health monitoring: by direct resistivity measurement (left) [28] and by electrical impedance tomography (EIT) (right) [49]. *Reproduced with permission from [49]. Copyright 2019 American Chemical Society.*

2.3. Phase separation

Phase separation is a phenomenon occurring when a homogeneous mixture of at least two polymers phase separate due to a change in miscibility of the monomer. The resulting material is composed of a multi-phase structure that reduces the shrinkage and leads to an enhanced surface quality.

2.3.1. A thermodynamic approach to phase separation

The phase separation observed in a system composed of a thermoset/thermoplastic blend can be usefully described with classical thermodynamics under several specific approximations. The most common one is the Flory-Huggins-Staverman model (FH) that takes into account temperature and molar mass effects, but as it sets the excess volumes to zero, it fails to take into account the pressure, expansion or contraction upon mixing [56]. However, the model gives a useful description of the nucleation and growth phenomena, and can be used to estimate the resulting microstructure of the phase separated blend. First, considering the interaction parameter χ to be concentration independent and only function of the temperature:

$$\chi = a + b/T \quad (2.6)$$

where a and b are constants, and T the temperature. Developing the entropy of mixing taking into account the defined interaction parameter, and assuming the monodispersity of the components, the Gibb's free energy ΔG of the system can be expressed as:

$$\Delta G = \frac{RT}{V_r} \left[\frac{\phi_P}{Z_P(p)} \ln \phi_P + \frac{\phi_M}{Z_M} \ln \phi_M + \chi(T) \phi_P \phi_M \right] \quad (2.7)$$

with R the perfect gas constant, V_r the reference volume of the unit cell, ϕ_P and ϕ_M the volume fraction of polymer (thermoset) and Low profile additive LPA (thermoplastic), $Z_P(p)$ and Z_M the ratio of the polymer/LPA molar volume to the unit cell and p is the degree of conversion of the monomer, in the case of a polymerization induced phase separation. From this expression, the chemical potential $\Delta\mu$ for each component is easily obtained:

$$\Delta\mu_P = RTZ_P(p) \left[\frac{1}{Z_P(p)} \ln \phi_P + \left(\frac{1}{Z_P(p)} - \frac{1}{Z_M} \right) \phi_M + \chi \phi_M^2 \right] \quad (2.8)$$

$$\Delta\mu_M = RTZ_M \left[\frac{1}{Z_M} \ln \phi_M + \left(\frac{1}{Z_M} - \frac{1}{Z_P(p)} \right) \phi_P + \chi \phi_P^2 \right]. \quad (2.9)$$

From these expressions, the conversion phase diagram can be calculated deriving the binodal and spinodal curves of the system. Taking the equilibrium conditions $\Delta\mu_P^\alpha = \Delta\mu_P^\beta$ and $\Delta\mu_M^\alpha = \Delta\mu_M^\beta$, the binodal curve of the system can be estimated fixing T and solving for the conversion p . Finally, the spinodal curve representing the boundary between thermodynamically unstable and metastable region of the phase diagram needs to be derived. That condition is fulfilled when the derivative of each chemical potential with respect to each components equals zero, giving the simple expression:

$$\frac{\phi_M}{Z_P(p)} + \frac{(1 - \phi_M)}{Z_M} = 2\chi\phi_M(1 - \phi_M). \quad (2.10)$$

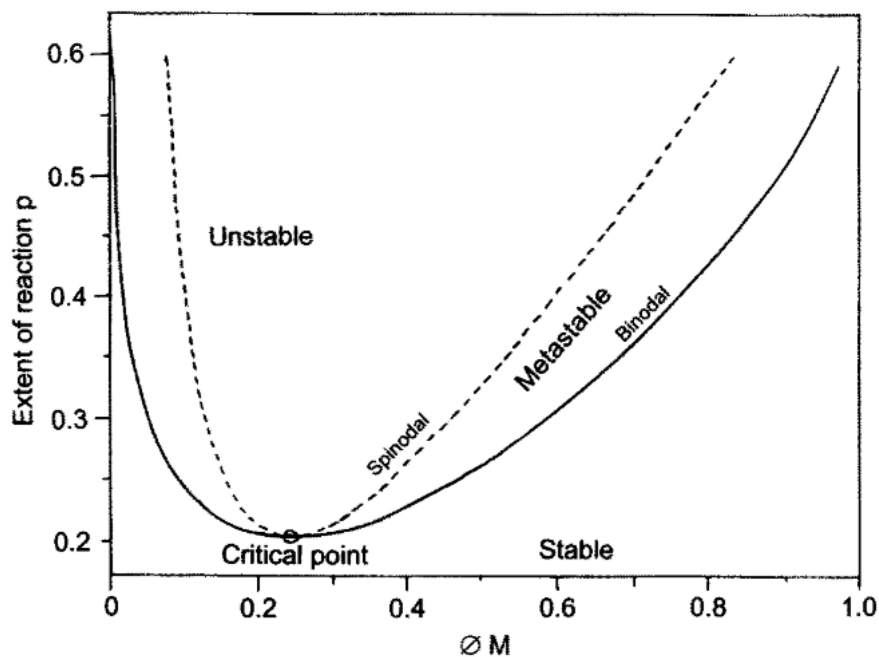


Figure 2.5: Phase diagram representing the binodal and spinodal curves evolution with the degree of cure and the fraction of LPA. [56] *Reproduced with permission from Springer Nature.*

2.3.2. Phase separation of the UP/LPA/Styrene system

The mechanism leading to phase separation of unsaturated polyester resin (UP) modified with a low profile additive (LPA) was first studied by Bucknall *et al.* in the mid 80s [57]. The research was conducted by blending UP with poly(vinyl acetate) (PVA) and representing the system as a *Monomer/PVA/Cured resin* phase diagram. That method helped to schematically understand the transition from the one-phase to the two-phase region based on the monomer consumption during polymerization. It however fails at taking into account the styrene contribution as reactive diluent. In a following paper, the different morphology of the UP/PVA/Styrene system were studied [58]. A low concentration of PVA leading to discrete particles rich in PVA in a UP matrix, when at higher concentration a bi-continuous structure is observed [56, 58]. The morphology was found to be closely linked to the composition of the resin as well as the curing

temperature, these aspects are reviewed in details later. Suspène *et al.* showed in two successive studies [59,60] the first experimental application of ternary phase diagram for a low profile additive modified UP using the cloud point curve (CPC). They also gave the first insight on the possible effect of polymerization on the CPC. The use of uncured resin is the limitation of this method, the obtained diagram deviating for cured resin because of the fractionation phenomenon that affects the polydispersity. The mechanism leading to phase separation of unsaturated polyester resin (UP) modified with a low profile additive (LPA), polymer added to allow phase separation and counteract the cure shrinkage, was studied Bucknall *et al.* [58]. The study showed the effect of styrene on a blend of UP– 6% PVAc (acrylic modified PVA). The results showed only a small effect of styrene on the morphology probably meaning a rather flat binodal curve. In the same study, the amount of PVAc was found to strongly affect the morphology showing an inversion in the phase separation and a critical point at only 5 wt% of LPA (see Figure 2.6). The same observations were observed by Bulliard *et al.* [61] in a similar study with a critical point shifted to larger quantity of PVAc because of the smaller molecular weight (M_w) of the thermoplastic. The size of the microstructure was also found affected by a change in molecular weight leading to a coarser microstructure because of the early perturbation of the system triggering an early nucleation leaving more time for growth. The same study investigated the effect of the curing temperature on the morphology of the cured blend, higher temperature refining the microstructure and slightly shifting the binodal curve toward larger volume fraction of thermoplastic.

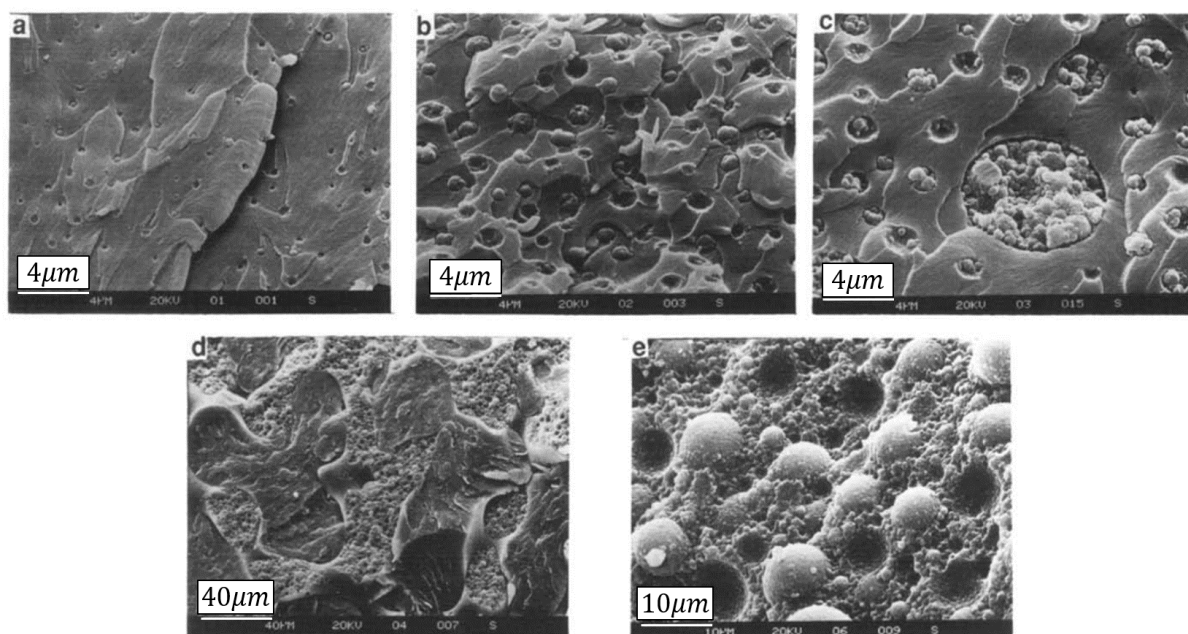


Figure 2.6: SEM images of UP blends containing (a) 1%, (b) 2%, (c) 3%, (d) 4% and (e) 6% of PVAc. [58] *Reproduced with permission from Elsevier.*

The detailed mechanisms for phase separation of UP/LPA/Styrene systems as well as their implication in the reduced polymerization shrinkage was discussed in several studies [61–63] and is believed to take place as follow. First, the initiator is decomposed in the system which triggers the cure. The early curing stage is characterized by the formation of polyester microgels due to the strong intramolecular cyclization tendency [61]. The unreacted styrene and LPA start to separate from these microgels, while they keep increasing in size until they are large enough to touch each other and form a tri-dimensional network. Gelation occurs and a co-continuous structure is created and stays upon further curing. In the last step of the cure, microvoids are developed in the LPA-rich phase and between the two domains to counterbalance the polymerization shrinkage of the UP-rich phase. Note that some LPAs, as PVA, are partially soluble in the uncured polyester/styrene solution. The phase separation will then occur due to the instability created by the cross-linking of UP. For other LPAs like poly(methyl

methacrylate) (PMMA) or polystyrene (PS), the mixture is unstable and phase separation may occur before the reaction. Similar behaviour and morphologies are observed with other LPAs as polyethylene (PE), polystyrene (PS), poly(vinyl acetate) (PVAc), poly(methyl methacrylate) (PMMA), poly ϵ -caprolactones (PCL), poly(styrene-*co*-butadiene), polyurethanes (PU), copolymers with acrylates, epoxies and other thermoplastic and thermosets. The following literature summarizes their use [48, 62–64].

2.3.3. Phase separation with nanoparticles

The effect of nanoparticles on phase separation was only studied regarding the consequences on the final morphology but few studies are focused on the phenomenon involved. Shih *et al.* [65] used carbon black in an epoxy/UP blend to enhance the flame retardant properties. The study showed phase separation both with or without the presence of carbon black. The same behaviour was observed by Guo Ma *et al.* [66]. In this study 1 wt% carbon black particles (30nm in diameter) were added to a blend of Epoxy/polyesterimide (PEI). When phase inversion was observed at 12 wt% of PEI without the filler, the critical point was shifted to 16wt% with the carbon black. The obtained morphology was small globules of epoxy embedded in a PEI matrix with the carbon black located in the continuous PEI phase leading to a double-percolation structure. Such structure shows a two phase percolation, the first one is function of the amount of conductive filler in the PEI phase, the second one originates from the continuity of the PEI phase [67, 68]. The conductivity can then be optimized by both the quantity of second phase and the quantity of filler. In all these studies, the selective distribution of the particles could be relatively successfully predicted by a thermodynamic approach first

proposed by Sumita *et al.* [67] based on the wetting coefficient:

$$\omega_a = \frac{\gamma_{fB} - \gamma_{fA}}{\gamma_{AB}} \quad (2.11)$$

with ω_a the wetting coefficient, γ_{fB} , γ_{fA} and γ_{AB} the surface tension between the filler and polymer B, the filler and polymer A and between polymer A and B, respectively. The filler will be dispersed in polymer A if $\omega_a > 1$, in between the two phases if $-1 < \omega_a < 1$ and in polymer B if $\omega_a < -1$. The surface tension between two interface 1 and 2 can be calculated using Wu's harmonic mean average assuming the surface tension γ as well as its dispersion γ^d and polar component γ^p are known¹:

$$\gamma_{12} = \gamma_1 + \gamma_2 - 4 \left(\frac{\gamma_1^d \gamma_2^d}{\gamma_1^d + \gamma_2^d} + \frac{\gamma_1^p \gamma_2^p}{\gamma_1^p + \gamma_2^p} \right). \quad (2.12)$$

The effect of GO on phase separation was studied by Yu *et al.* [70] with an epoxy (DGEBA) blended with PEI. The study concluded that the final microstructure was determined by a competition between the cure reaction and the phase separation rate. The phenomenon was largely dominated by the viscosity of the system. The speed at which phase separation occurs is closely linked to the viscosity of the system, a lower viscosity allowing a better diffusion of the polymer chain leading to a quicker separation reaction. The addition of GO increasing the viscosity, it has a slowing effect on the phase separation. However, the viscosity was not found to increase dramatically with the amount of GO. That would suggest that another phenomenon might occur probably linked to the large surface density of the GO trapping the polymer molecules and avoiding their diffusion. As both these phenomena are freezing the morphology at an earlier stage, the

¹Note that most of these values can be found in Wu's *Polymer interface and adhesion* [69].

separation remains incomplete at the gel point [70]. A DSC study showed that the onset temperature slightly decreases when the peak temperature increases with GO, which is consistent with an acceleration effect. The addition of GO would then be responsible for a quicker cure of the resin, that assumption being supported by the larger enthalpy of reaction in the presence of GO or graphene. The acceleration effect is then probably linked to the large surface area of the fillers. A recent study by Wang *et al.* [71] studied the selective localization of multi-walled carbon nanotubes (MWCNTs) in an epoxy/PEI system. They observed a selective localization of the MWCNTs in the PEI-rich phase resulting from reaction-induced phase separation, following the prediction of Equation 2.12. The electrical conductivity of the resulting material showed an impressive reduction of the percolation threshold of eight orders of magnitude in volume resistivity, compared to the non-phase separated system, at only 1.0 wt% of filler. That results is encouraging to reach similar reduction of percolation threshold with graphene, but with higher electrical conductivity ($10^6 - 10^7$ S/m for CNT and 10^8 S/m for graphene [5]). Finally, another recent study by Sahalianov *et al.* [72] numerically investigated the evolution of the conductivity and the percolation threshold in segregated polymer network with different nano-fillers. In other words, the creation of a network of high filler density in a matrix composed of polymer particles (an analogy of hot pressed carbon-coated thermoplastic particles). The study concluded the enhancement of the percolation threshold proportional to the ratio of the particle/filler (d_p/d_{filler}) diameter for all type of filler. The larger the ratio, the smaller the resulting threshold. That behaviour saturates when the size of the particle exceeded the size of the filler by more than 30 times. In the case of a disordered polymer network, which is a good approximation of a phase separated morphology, the

minimal percolation threshold was found to be close to $d_p/d_{filler} \approx 5$. Interestingly, the fillers aspect ratio was found to have no effect on the enhancement of the percolation threshold for segregated structures and to be mainly linked to the selective localization of the particle outside of the "excluded volume" represented by the polymer particles.

The degree of crystallinity of the phase-separating thermoplastic was also found to be slightly impacted in the presence of high aspect ratio particles like graphene. It was shown that graphene-oxide act as a crystallization site for the LPAs like polycaprolactone (PCL) increasing the rate of crystallization leading to slightly higher crystallinity which could influence the mechanical properties of the system [73].

2.4. Research gaps

The presented state-of-the-art showed that, while advanced in every aspect individually (graphene, composite processing, phase-separation and health monitoring), it lacks in joining them together.

1. Regarding the graphene, most of these studies use high quality CVD graphene that is not designed for large industrial applications. It is almost exclusively done in non-reinforced systems due to the complex filtering issue arising during processing, dramatically reducing the conductivity. The few studies using few-layer-graphene (FLG) in reinforced systems showed that it was needed in a very large amount to be conductive, affecting the processability of the system. To solve this and the filtering effect of the fibres, hand-layup processing is usually used which is not designed for industrial processing.
2. Regarding the phase-separation, while well documented for the phase-separated

morphologies of unsaturated polyester systems, the literature only studied the addition of carbon black and carbon nanotubes to these systems. The effect of graphene on the morphology and on the mechanical and electrical properties of such systems is still missing. Especially the coupled effect they could have on the toughness and percolation threshold of the system. Most studies are mostly focused on non-reinforced system lacking to describe the possible effect of fibres on the morphology of phase-separation.

3. Regarding the sensing capabilities, the literature focused on CVD graphene sensors lacking in describing few-layer graphene-based systems. The coupled effect of phase-separation, graphene and fibre on the electron flow and how it affects the sensing capabilities for such polymer system is absent. An in depth study of the electrical response to different solicitation mode and its link to the mechanical properties is also missing.

This work aims at filling these gaps and show that a FLG based phase-separating resin can be manufactured into a fibre reinforced system with industrial techniques (compression resin transfer moulding), while increasing its toughness and reducing its percolation threshold. Doing so, using the lowest possible amount of graphene and LPA while optimizing its sensing capabilities.

References

- [1] K. S. Novoselov, A. K. Geim, S. V. Morozov, D Jiang, Y Zhang, S. V. Dubonos, I. V. Grigorieva, and A. A. Firsov. Electric Field Effect in Atomically Thin Carbon Films Supplementary. *Science*, 5(1):1–12, 2004.
- [2] Wencai Ren and Hui Ming Cheng. The global growth of graphene. *Nature Nanotechnology*, 9(10):726–730, 2014.

- [3] Changgu Lee, Xiaoding Wei, Jeffrey W Kysar, and James Hone. Measurement of the Elastic Properties and Intrinsic Strength of Monolayer Graphene. *Science*, 321(July):385–388, 2008.
- [4] GRANTA EduPack. GrantaDesign, 2020.
- [5] Shaker A Meguid and George J Weng. *Micromechanics and Nanomechanics of Composite Solids*. 2018.
- [6] Kasap Capper, editor. *Springer Handbook of Electronic and Photonic Materials*. 2017.
- [7] Sungjin Park and Rodney S. Ruoff. Chemical methods for the production of graphenes. *Nature Nanotechnology*, 4(4):217–224, 2009.
- [8] Dimitrios G. Papageorgiou, Ian A. Kinloch, and Robert J. Young. Mechanical properties of graphene and graphene-based nanocomposites. *Progress in Materials Science*, 90:75–127, 2017.
- [9] Quentin Arthur Poutrel, Zixin Wang, Dongyi Wang, Constantinos Soutis, and Matthieu Gresil. Effect of pre and Post-Dispersion on Electro-Thermo-Mechanical Properties of a Graphene Enhanced Epoxy. *Applied Composite Materials*, 24(2):313–336, 2017.
- [10] Velram Balaji Mohan, Krishnan Jayaraman, and Debes Bhattacharyya. Fabrication of highly conductive graphene particle-coated fiber yarns using polymeric binders through efficient coating techniques. *Advances in Polymer Technology*, 37(8):3438–3447, 2018.
- [11] Minghe Fang, Xuhai Xiong, Yabin Hao, Tengxin Zhang, Han Wang, Hui Ming Cheng, and You Zeng. Preparation of highly conductive graphene-coated glass fibers by sol-gel and dip-coating method. *Journal of Materials Science and Technology*, 35(9):1989–1995, 2019.
- [12] Velram Balaji Mohan, Kin tak Lau, David Hui, and Debes Bhattacharyya. Graphene-based materials and their composites: A review on production, applications and product limitations. *Composites Part B: Engineering*, 142(January):200–220, 2018.
- [13] N. Saravanan, R. Rajasekar, S. Mahalakshmi, T. P. Sathishkumar, Ksk Sasikumar, and S. Sahoo. Graphene and modified graphene-based polymer nanocomposites - A review. *Journal of Reinforced Plastics and Composites*, 33(12):1158–1170, 2014.
- [14] Robert J. Young, Ian A. Kinloch, Lei Gong, and Kostya S. Novoselov. The mechanics of graphene nanocomposites: A review. *Composites Science and Technology*, 72(12):1459–1476, 2012.
- [15] Rani Rohini, Prajakta Katti, and Suryasarathi Bose. Tailoring the interface in graphene/thermoset polymer composites: A critical review. *Polymer*, 70:A17–A34, 2015.

- [16] Kesong Hu, Dhaval D. Kulkarni, Ikjun Choi, and Vladimir V. Tsukruk. Graphene-polymer nanocomposites for structural and functional applications. *Progress in Polymer Science*, 39(11):1934–1972, 2014.
- [17] Sunil P. Lonkar, Yogesh S. Deshmukh, and Ahmed A. Abdala. Recent advances in chemical modifications of graphene. *Nano Research*, 8(4):1039–1074, 2015.
- [18] Rani Rohini, Prajakta Katti, and Suryasarathi Bose. Tailoring the interface in graphene/thermoset polymer composites: A critical review, 2015.
- [19] Xi Shen, Zhenyu Wang, Ying Wu, Xu Liu, and Jang Kyo Kim. Effect of functionalization on thermal conductivities of graphene/epoxy composites. *Carbon*, 108:412–422, 2016.
- [20] Vikas Mittal. Functional polymer nanocomposites with graphene: A review. *Macromolecular Materials and Engineering*, 299(8):906–931, 2014.
- [21] Daniel R Dreyer, Sungjin Park, W Bielawski, and Rodney S Ruoff. The chemistry of graphene oxide. *The royal Society of Chemistry*, 39:228–240, 2010.
- [22] Meysam Rahmat. *Carbon Nanotube – Polymer Interaction in Nanocomposites*. PhD thesis, 2011.
- [23] Yu Rok Lee, Anjanapura V. Raghu, Han Mo Jeong, and Byung Kyu Kim. Properties of waterborne polyurethane/functionalized graphene sheet nanocomposites prepared by an in situ method. *Macromolecular Chemistry and Physics*, 210(15):1247–1254, 2009.
- [24] Asma Yasmin, Jyi Jiin Luo, and Isaac M. Daniel. Processing of expanded graphite reinforced polymer nanocomposites. *Composites Science and Technology*, 66(9):1182–1189, 2006.
- [25] Tapas Kuilla, Sambhu Bhadra, Dahu Yao, Nam Hoon Kim, Saswata Bose, and Joong Hee Lee. Recent advances in graphene based polymer composites, 2010.
- [26] Swetha Chandrasekaran, Narumichi Sato, Folke Tölle, Rolf Mülhaupt, Bodo Fiedler, and Karl Schulte. Fracture toughness and failure mechanism of graphene based epoxy composites. *Composites Science and Technology*, 97:90–99, 2014.
- [27] Muhammad Helmi Abdul Kudus, Muhammad Razlan Zakaria, Muhammad Bisyrul Hafi Othman, and Hazizan Md Akil. Preparation and characterization of colloidized diamine/oxidized-graphene via condensation polymerization of carboxyl groups epoxy/oxidized-graphene nanocomposite. *Polymer*, 124:186–202, 2017.
- [28] A. J. Marsden, D. G. Papageorgiou, C. Vallés, A. Liscio, V. Palermo, M. A. Bissett, R. J. Young, and I. A. Kinloch. Electrical percolation in graphene-polymer composites. *2D Materials*, 5(3), 2018.
- [29] Isaac Balberg. Percolation Theory and Its Application in Electrically Conducting Materials. In Wiley-VCH Verlag GmbH & Co, editor, *Semiconducting Polymer Composites: Principles, Morphologies, Properties and Applications*, pages 145–169. 2013.

- [30] Cyrill Cattin. *Carbon nanotube modified polydimethylsiloxane - From percolation to piezoresistance*. PhD thesis, McGill University, 2015.
- [31] Hu Liu, Yilong Li, Kun Dai, Guoqiang Zheng, Chuntai Liu, Changyu Shen, Xingru Yan, Jiang Guo, and Zhanhu Guo. Electrically conductive thermoplastic elastomer nanocomposites at ultralow graphene loading levels for strain sensor applications. *Journal of Materials Chemistry C*, 4(1):157–166, 2015.
- [32] Jun Wei Zha, Bo Zhang, Robert K.Y. Li, and Zhi Min Dang. High-performance strain sensors based on functionalized graphene nanoplates for damage monitoring. *Composites Science and Technology*, 123:32–38, 2016.
- [33] Ning Hu, Takaomi Itoi, Taro Akagi, Takashi Kojima, Junmin Xue, Cheng Yan, Satoshi Atobe, Hisao Fukunaga, Weifeng Yuan, Huiming Ning, Surina, Yaolu Liu, and Alamusi. Ultrasensitive strain sensors made from metal-coated carbon nanofiller/epoxy composites. *Carbon*, 51(1):202–212, 2013.
- [34] National Instruments. Strain Gauge Measurement – A Tutorial. *Application Note 078*, (August):1–12, 1998.
- [35] Akram Zitoun, Dimitrios Fakis, Nithin Jayasree, Sadik Omairey, Fokion Oikonomidis, Zlatka Stoeva, and Mihalis Kazilas. Graphene-based strain sensing in composites for structural and health monitoring applications. *SN Applied Sciences*, 4(2), 2022.
- [36] Yong Liu, Dong Zhang, Kai Wang, Yanyun Liu, and Yu Shang. A novel strain sensor based on graphene composite films with layered structure. *Composites Part A: Applied Science and Manufacturing*, 80:95–103, 2016.
- [37] Farid Sayar Irani, Ali Hosseinpour Shafaghi, Melih Can Tasdelen, Tugce Delipinar, Ceyda Elcin Kaya, Guney Guven Yapici, and Murat Kaya Yapici. Graphene as a Piezoresistive Material in Strain Sensing Applications. *Micromachines*, 13(1), 2022.
- [38] Rufang Yu, Chengyan Zhu, Junmin Wan, Yongqiang Li, and Xinghua Hong. Review of graphene-based textile strain sensors, with emphasis on structure activity relationship. *Polymers*, 13(1):1–22, 2021.
- [39] Jingwen Chu, Alexander J. Marsden, Robert J. Young, and Mark A. Bissett. Graphene-Based Materials as Strain Sensors in Glass Fiber/Epoxy Model Composites. *ACS Applied Materials and Interfaces*, 11(34):31338–31345, 2019.
- [40] Bin Hao, Qing Ma, Sudong Yang, Edith Mäder, and Peng Cheng Ma. Comparative study on monitoring structural damage in fiber-reinforced polymers using glass fibers with carbon nanotubes and graphene coating. *Composites Science and Technology*, 129:38–45, 2016.
- [41] Haroon Mahmood, Lia Vanzetti, Massimo Bersani, and Alessandro Pegoretti. Mechanical properties and strain monitoring of glass-epoxy composites with graphene-coated fibers. *Composites Part A: Applied Science and Manufacturing*, 107:112–123, 2018.

- [42] M. Sánchez, R. Moriche, S. G. Prolongo, A. R. Marrón, A. Jiménez-Suárez, and A. Ureña. Evaluation of sensitivity for detecting different failure modes of epoxy matrix composites doped with graphene nanoparticles. *Composite Structures*, 225(April):111167, 2019.
- [43] R. Moriche, M. Sánchez, A. Jiménez-Suárez, S. G. Prolongo, and A. Ureña. Electrically conductive functionalized-GNP/epoxy based composites: From nanocomposite to multiscale glass fibre composite material. *Composites Part B: Engineering*, 98:49–55, 2016.
- [44] R. Moriche, A. Jiménez-Suárez, M. Sánchez, S. G. Prolongo, and A. Ureña. Sensitivity, influence of the strain rate and reversibility of GNPs based multiscale composite materials for high sensitive strain sensors. *Composites Science and Technology*, 155:100–107, 2018.
- [45] Marialaura Clausi, Elisa Toto, Sabina Botti, Susanna Laurenzi, Valeria La Saponara, and M. Gabriella Santonicola. Direct effects of UV irradiation on graphene-based nanocomposite films revealed by electrical resistance tomography. *Composites Science and Technology*, 183(March):107823, 2019.
- [46] Susanne Nonn, Martin Schagerl, Yingjun Zhao, Sandra Gschossmann, and Christoph Kralovec. Application of electrical impedance tomography to an anisotropic carbon fiber-reinforced polymer composite laminate for damage localization. *Composites Science and Technology*, 160(February):231–236, 2018.
- [47] Hashim Hassan and Tyler N. Tallman. Precise damage shaping in self-sensing composites using electrical impedance tomography and genetic algorithms. *Structural Health Monitoring*, 22(1):372–387, 2023.
- [48] Sabu Thomas, Mahesh Hosur, and Cintil Jose Chirayil, editors. *Unsaturated Polyester Resins: Fundamentals, Design, Fabrication and Applications*. Elsevier, 2019.
- [49] Hongbo Dai and Erik T. Thostenson. Large-Area Carbon Nanotube-Based Flexible Composites for Ultra-Wide Range Pressure Sensing and Spatial Pressure Mapping. *ACS Applied Materials and Interfaces*, 11(51):48370–48380, 2019.
- [50] Fuchao Hao, Shaokai Wang, Fei Xing, Min Li, Tianshu Li, Yizhuo Gu, Wei Zhang, and Jiahui Zhang. Carbon-Nanotube-Film-Based Electrical Impedance Tomography for Structural Damage Detection of Carbon-Fiber-Reinforced Composites. *ACS Applied Nano Materials*, 4(5):5590–5597, 2021.
- [51] Jinwon Oh, Jun Chang Yang, Jin Oh Kim, Hyunkyung Park, Se Young Kwon, Serin Lee, Joo Yong Sim, Hyun Woo Oh, Jung Kim, and Steve Park. Pressure insensitive strain sensor with facile solution-based process for tactile sensing applications. *ACS Nano*, 12(8):7546–7553, 2018.
- [52] Helena Rocha, Christophe Fernandes, Nelson Ferreira, Ugo Lafont, and João P. Nunes. Damage localization on CFRP composites by electrical impedance tomography. *Materials Today Communications*, 32(July), 2022.

- [53] Andy Adler, Tao Dai, and William R.B. Lionheart. Temporal image reconstruction in electrical impedance tomography. *Physiological Measurement*, 28(7), 2007.
- [54] Andy Adler, John H. Arnold, Richard Bayford, Andrea Borsic, Brian Brown, Paul Dixon, Theo J.C. Faes, Inéz Frerichs, Hervé Gagnon, Yvo Gärber, Bartłomiej Grychtol, Günter Hahn, William R.B. Lionheart, Anjum Malik, Robert P. Patterson, Janet Stocks, Andrew Tizzard, Norbert Weiler, and Gerhard K. Wolf. GREIT: A unified approach to 2D linear EIT reconstruction of lung images. *Physiological Measurement*, 30(6), 2009.
- [55] Andy Adler and Robert Guardo. Electrical impedance tomography: Regularized imaging and contrast detection. *IEEE Transactions on Medical Imaging*, 15(2):170–179, 1996.
- [56] Roberto J.J. Williams, Boris A. Rozenberg, and Jean Pierre Pascault. Reaction-Induced Phase Separation in Modified Thermosetting Polymers. *Advances in Polymer Science*, 128:95–156, 1997.
- [57] Clive B. Bucknall, Peter Davies, and Ivana K. Partridge. Phase separation in styrenated polyester resin containing a poly(vinyl acetate) low-profile additive. *Polymer*, 26(1):109–112, 1985.
- [58] Clive B. Bucknall, Ivana K. Partridge, and Martin J. Phillips. Morphology and properties of thermoset blends made from unsaturated polyester resin, poly(vinyl acetate) and styrene. *Polymer*, 32(5):786–790, 1991.
- [59] L. Suspene and J.P. Pascault. Incompatible Ternary Blends Based on Unsaturated Polyester Resins. I. Phase Diagrams. *Journal of Applied Polymer Science*, 41:2665–2675, 1990.
- [60] Laurent Suspène, Dominique Fourquier, and Yeong Show Yang. Application of phase diagrams in the curing of unsaturated polyester resins with low-profile additives. *Polymer*, 32(9):1593–1604, 1991.
- [61] X. Bulliard, V. Michaud, and J. A.E. Månson. Reaction-induced phase separation in poly(vinyl acetate)/ polyester blend. *Journal of Applied Polymer Science*, 102(4):3877–3888, nov 2006.
- [62] Mark Kinkelaar, Bing Wang, and L. James Lee. Shrinkage behaviour of low-profile unsaturated polyester resins. *Polymer*, 35(14):3011–3022, 1994.
- [63] Mohamad Hosain Beheshty, Mehran Hayaty, and Mehdy Vafayan. Evaluation of low-profile additives in the curing of unsaturated polyester resins at low temperatures. *Iranian Polymer Journal (English Edition)*, 15(2):143–153, 2006.
- [64] Geoffrey Pritchard. *Plastics additives an A-Z redereence*, volume 53. 1998.
- [65] Yeng Fong Shih and Ru Jong Jeng. Carbon black containing IPNs based on unsaturated polyester/epoxy. I. Dynamic mechanical properties, thermal analysis, and morphology. *Journal of Applied Polymer Science*, 86(8):1904–1910, 2002.

- [66] C. Guo Ma, D. Yong Xi, and M. Liu. Epoxy resin/polyetherimide/carbon black conductive polymer composites with a double percolation structure by reaction-induced phase separation. *Journal of Composite Materials*, 47(9):1153–1160, 2013.
- [67] Masao Sumita, Kazuya Sakata, Shigeo Asai, Keizo Miyasaka, and Hideaki Nakagawa. Dispersion of fillers and the electrical conductivity of polymer blends filled with carbon black. *Polymer Bulletin*, 25(2):265–271, 1991.
- [68] M. Sumita, K. Sakata, Y. Hayakawa, S. Asai, K. Miyasaka, and M. Tanemura. Double percolation effect on the electrical conductivity of conductive particles filled polymer blends. *Colloid & Polymer Science*, 270(2):134–139, 1992.
- [69] Souheng Wu. *Polymer interface and adhesion*. CRC Press, 1982.
- [70] Guijun Yu and Peiyi Wu. Effect of chemically modified graphene oxide on the phase separation behaviour and properties of an epoxy/polyetherimide binary system. *Polymer Chemistry*, 5(1):96–104, 2014.
- [71] Xue Wang, Weizhen Li, Zhao Zhang, Kaimin Chen, and Wenjun Gan. Selective localization of multi-walled carbon nanotubes in epoxy/polyetherimide system and properties of the conductive composites. *Journal of Applied Polymer Science*, 136(35):1–10, 2019.
- [72] Ihor Sahalianov and Olexandra Lazarenko. Enhancement of electroconductivity and percolation threshold by the morphology of dielectric network in segregated polymer/nanocarbon composites. *Materials Research Express*, 6(9), 2019.
- [73] Isabel Castilla-Cortázar, Ana Vidaurre, Bernabé Marí, and Alberto J. Campillo-Fernández. Morphology, crystallinity, and molecular weight of poly(ϵ -caprolactone)/graphene oxide hybrids. *Polymers*, 11(7), 2019.

PREFACE – CHAPTER 3

The following chapter presents the first step of this research, the development of a phase-separating resin system. The toughness of three unsaturated polyester resins (UP) was measured as a function of the added quantity of low-profile additives (polycaprolactone) and of the obtained phase-separated morphology. The system showing the highest toughness for the lowest amount of PCL was chosen for further investigation, measuring its toughness with varying quantities of graphene. The goal of this chapter was to determine the optimal UP/PCL/graphene blend composition in order to reach the highest toughness with the lowest quantity of PCL and graphene. A first insight on the coupled effect of graphene and phase-separation on the electrical properties was conducted as well, a more detailed study is presented in Chapter 5. The supplementary materials for this chapter can be found in the Appendix - Chapter B.

CHAPTER 3

A phase separation strategy for enhanced toughness self-assembly graphene-network composites.

N. Hostettler, P. Hubert, Composites Science and Technology 225 (2022) 109503

DOI: <https://doi.org/10.1016/j.compscitech.2022.109503>

Keywords: Nanocomposites; Graphene; Fracture toughness; Electrical properties

Abstract

The toughness of three unsaturated polyester resins modified with different quantities of polycaprolactone (PCL) and few-layer graphene microsheets was evaluated by single-edge-notch bending (SENB). The addition of PCL to the resin systems created phase-separated microstructures with different critical compositions at phase inversion (7, 15 and 16.5 wt% PCL). The addition of PCL in quantities lower than the critical compositions showed increases up to 90 % in toughness. A similar effect was observed by the addition of graphene to the neat resin increasing the toughness by up to 96 % with 6 wt% of graphene. The incorporation of graphene to a phase separating system was found to form a self-assembly graphene-network at the unsaturated polyester-rich phase of the microstructure. When such network showed an appreciable effect of the toughness compared to the system without the PCL (114 % increase at 6 wt% graphene and 2 wt% PCL), it also positively impacted the electrical conductivity. A shift of the percolation threshold towards a lower quantity of graphene was achieved by the creation of such

graphene-rich network, reducing by 2 wt% the quantity of graphene needed for conduction.

3.1. Introduction

The use of composite materials is becoming the norm in different fields like transportation, energy or sport as a lightweight alternative to metals. Regulations on CO₂ and more generally gas emissions are pushing toward the use of such materials, leading to noticeable mass reduction and to “greener” final parts. This positive impact is somewhat shaded by the shorter lifetime of composite parts compared to metals. This limitation is mostly coming from the brittleness of the thermoset resin allowing easy crack propagations leading to a catastrophic failure, usually by fatigue crack growth, low velocity impacts or a coupling of the two [1,2]. As the technology for thermoset composite recycling is not yet available (or not at competitive costs), the parts are usually either repaired at high costs (total budget expected to reach 22 Bn\$ worldwide by 2026 [3]) or disposed in landfills with the known negative impact on the environment [4]. The use of multifunctional materials enabling to track the strain and damage evolution of the part are promising candidate to help tackle these issues. Such multifunctionality can be achieved by adding piezoresistive carbon-based particles to the polymer matrix usually carbon nanotubes (CNT), carbon black or graphene [5–7]. Numerous research were conducted to study the mechanical and electrical properties of graphene-based composites with, for example, reported increase in toughness from 8 % at 1 wt% of graphene [8], to 100 % at 3 wt% [9] or to an impressive 1185 % at 0.0275 wt% of graphene [10]. There is then a large variation in the observed behaviour throughout literature due to the different quality of the graphene

used in the research [11], high purity mono-layered graphene leading to higher performance than multi-layered graphene platelets. The use of such high quality graphene is, however, limited by its costs, low volume of production not suitable for large composite part processing and by its high specific surface area that makes it prone to re-aggregation. Cheaper industrial few/many-layers graphene appears to be a better candidate to be used as filler in polymeric system with the drawback of a much larger quantity needed to see a noticeable increase in toughness and conductivity, negatively affecting the production capabilities (increased viscosity, final degree of cure, etc...). The construction of a graphene network in the polymeric system could help reducing the quantity of graphene needed to reach multifunctional capabilities. Such self-assembly network of particles were studied with thermoplastic blends [12–14] and more recently with blends of epoxy and thermoplastics [15–18]. The phase-separated morphology creates a double-percolation effect by localizing the particles in one phase [14, 17] positively impacting the thermal and electrical conductivity shifting the percolation threshold toward lower quantity of filler [19]. These studies, however, lack to describe the coupled effect of graphene and phase separation on the mechanical properties of the system. Polymer blends are especially common with unsaturated polyester since most of these resins have a few percents of low-profile-additives (LPA) in their composition to avoid cracking due to the cure shrinkage [20–22], they are then good candidates for such applications. The objective of this research is to develop several phase separating systems based on unsaturated polyester (UP) and polycaprolactone (PCL), and study the coupled effects of graphene and phase-separated morphologies on the toughness and electrical conductivity of the systems.

3.2. Materials and Methods

3.2.1. Materials

The characterization of the phase separation was done on three different unsaturated polyester resin (UP): (i) the PolyLite 31520 and (ii) the PolyLite 31289 both from *Reichhold*, and the R920-axa-18 from *AOC*. The first resin (i) was accelerated with 0.2 wt% of Cobalt 12 % and 0.2 wt% of HQN 20 % from *CCP composites*. The system was then cured with 2.5 wt% of Norox 750 from *United-initiator*. The second (ii) and the third (iii) resin were pre-accelerated by the manufacturer and were simply cured adding 2 wt% of Norox Azox from *United-initiator*. Note that all these resins were formulations without LPA. The thermoplastic LPA substitute was the CAPA 6500 system from *Ingevity*, a polycaprolactone (PCL).

The graphene powder was the GrapheneBlack 3X from *NanoXplore inc.*, a low-cost industrial quality graphene with a primary particle size between 1-2 μm and an agglomerate size of $D_{50}=38 \mu\text{m}$, 6 to 10 graphene layers in thickness, a carbon to oxygen ratio of 96:1 and a bulk density of 0.2 - 0.3 g/cm^3 [23]. According to the classification framework for graphene-based material proposed by Bianco *et al.* [24], Wick *et al.* [25] and the ISO/TS 21356-1:2021, this material should be referred to as few-layer graphene microsheets. This graphene powder then stands in the middle range of graphene quality at about half of what is found for high quality graphene (C/O up to 257:1 [25]), much higher than the typical graphene oxide GO (C/O = 2:1 [25]) and reduced graphene oxide (C/O = 12:1 [25]). For simplicity, it will still be referred to as graphene for the rest of the paper.

3.2.2. Methods

Blend and sample preparation

The unsaturated polyester resin was thoughtfully weighted into a glass jar, the formulations to contain graphene were transferred into a glove box (Precise controlled Atmosphere Glove Box, *Labconco Corp.*, Mo, USA). The correct amount of graphene was then weighted and added to the resin, the jar was transferred into a hood and set in a water bath preheated at 65 °C. The right amount of PCL pellets was added, and the mixture was mechanically stirred at 1500 rpm for 20 min until the pellets were fully dissolved leading to a homogeneous system. A dispersion step was then carried on formulation with graphene by setting the jar in an ultrasonic bath at room temperature for an hour while mechanically stirring the mixture at low velocity. Note that a degassing step was performed before dispersion as dissolved air is known to reduce the cavitation effect of ultrasonic wave affecting the quality of the dispersion.

Two of these blended mixtures were observed to phase separate before cure, PolyLite 31289 and AOC R920, when the PolyLite 31520 was stable at room temperature and phase separate during the cure. From that point, two different strategies were followed: the two systems phase-separating before the cure were rested for 20min at room temperature to stabilize prior curing. The different additives were precisely added to the mixture and manually stirred in until fully dispersed. The system was then degassed for 30s to remove the remaining air bubbles and finally cast into a mould with the dimension of the toughness sample. The PolyLite 31289 and AOC R920 were cured at 50°C for 30min when the PolyLite 31520 was cured at 65 °C for 30 min according to its datasheet. A lower temperature was adopted for the two other systems to allow more time to degas and cast

the samples ($t_{gel} = 1 - 4$ min). Note that as the phase separation occurs before the cure, the curing temperature only has a minor effect on the phase separated morphology. The cured samples were then demoulded and post-cured for 2h at 120°C to increase the mechanical properties and degree of cure. As unsaturated polyester resins tend to evolve with time after post-cure, the samples were set in a 20 %RH and 20°C chamber to stabilize for at least 48 h before testing. Samples with quantity of PCL from 0 to 25 wt% and graphene from 0 to 6 wt% were produced following this method.

Toughness and compression tests

The toughness measurements were performed following the ASTM D5045 - 14 in the single-edge-notch bending (SENB) configuration. The samples coming out of the mould were 8 mm in thickness, 16 mm wide and 7cm in length, which corresponds to the dimension ratio of the ASTM. The span of the 3-point bending setup was set to $S = 4W = 6.4$ cm. A notch of approximately 7.9 mm was machined and a natural crack was initiated with a clean razor blade. At least 3 specimens were tested per conditions on an MTS 5kN universal testing machine at room temperature with a loading rate of 0.1 mm/s. The chosen loading rate is slightly lower than the suggested one to avoid the sample to break too quickly. Note that no displacement correction was done to the results as the sample broke at relatively low force with no support indentation. The conditional toughness K_Q was calculated from the test results as:

$$K_Q = \left(\frac{P_Q}{BW^{1/2}} \right) f(x) \quad (3.1)$$

where $f(x)$ ($0 < x < 1$) is defined as:

$$f(x) = 6x^{1/2} \frac{1.99 - x(1-x)(2.15 - 3.93x + 2.7x^2)}{(1+2x)(1-x)^{3/2}} \quad (3.2)$$

where P_Q is the load, B and W the thickness and the width of the specimen respectively, $x = a/W$ with a the crack length. In order to validate the measured K_Q into K_{Ic} , the test must be performed in plane strain and avoid excessive plasticity, respecting the size criteria:

$$B, a, (W - a) > 2.5 \left(\frac{K_Q}{\sigma_y} \right)^2 \quad (3.3)$$

with B the thickness of the sample, a the crack length, W the width, K_Q the measured conditional toughness and σ_y the tensile yield stress. The latter was measured taking $0.7\sigma_y^{compression}$, the compressive yield stress as suggested in the ASTM. The crack length was measured on the broken samples by microscopy.

The compression tests were conducted following ASTM D695 - 15 with a sample dimension of 8 x 8 x 16 mm. The tests were carried out at 1 mm/s at room temperature and five samples were tested per conditions. Note that the sides of the samples were thoughtfully polished to achieve yielding. The yield stress was measured from the test data following the ASTM.

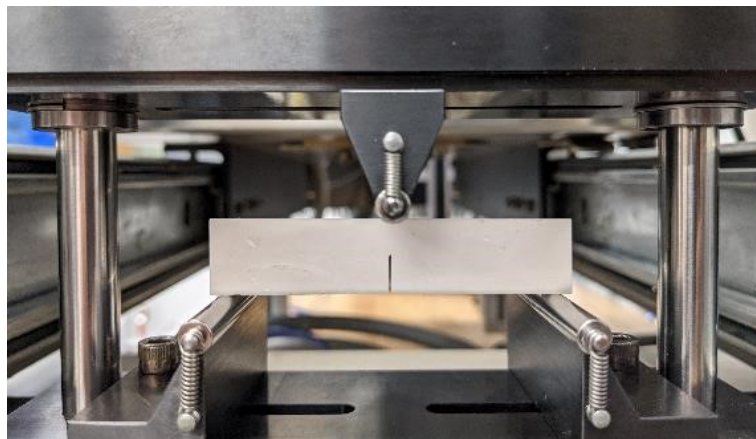


Figure 3.1: 3-point bending setup with notched sample.

Electrical conductivity measurements

Flat samples were cast in a 3mm thick mould and cut to 70 x 70 mm squares. The volume resistivity measurements were done on a Keithley – Resistivity Test Fixture Model 8009 powered by a Keithley – Electrometer Model 6517A following ASTM D-257, cleaning the samples and the electrodes with acetone between each measurement. The signal was acquired on LabView code and let to stabilize for a couple minutes. The measured value of resistance was taken as the average of the last 15 s of the stabilized signals. The corresponding volumetric resistivity was calculated as:

$$\rho_V = \frac{22.9V}{tI} = \frac{22.9}{t}R = \frac{1}{\sigma_V} \quad (3.4)$$

where ρ_V is the volumetric resistivity, t the thickness of the sample, V the applied voltage, I the current reading, R the resistance and σ_V the conductivity. The applied voltage was 100 V for compositions below the percolation threshold and 2 V for compositions above it.

3.3. Results and Discussion

3.3.1. Phase separation and resulting morphologies

The systems studied are ternary phase separating system with a mixture of PCL, unsaturated polyester chains and styrene as reactive diluent [26]. Two behaviours were observed between the three tested resins: (i) a polymerization induced phase separation (PIPS) and (ii) a temperature or time induced phase separation. In the first case the resin remains stable at room temperature and does not phase separate until the additives are

added, this is the case for the Polylite 31250. In the second case, the mixture is homogeneous but meta stable during the mixing process and phase separate before adding the additives, this is observed for the Polylite 31289 and AOC R920. The physical mechanism leading to this difference is probably linked to the molar mass of the polyester chain known to have a strong impact on the entropic contribution to the free energy of mixing [27, 28], to the fraction of styrene as reactive diluent and/or on other additives already present in the commercial systems.

Polymerization induced phase separation - Polylite 31250

The morphologies were characterized after the cure on the SENB samples; hence they also show the fracture mechanisms analyzed later. Three compositions with 5, 16.5 and 25 wt% of PCL are shown in Figure 3.2. Note that the sample at 16.5 wt% was imaged by optical microscopy (OM) because its coarse morphology, the two others were imaged by scanning electronic microscopy (SEM).

The morphologies observed in literature were usually obtained by blending unsaturated polyester with poly(methyl methacrylate) (PMMA) or poly(vinyl acetate) (PVAc) [20, 22, 28–31]. The blends obtained with PCL are comparable with the ones obtained with other thermoplastics: from low quantity and increasing the amount of thermoplastic - firstly particles of PCL embedded in a matrix of UP, a co-continuous network of PCL and UP, and finally seeing a phase inversion leading to particles of UP embedded in a matrix of thermoplastic. The presence of a co-continuous region shows a change in the growth mechanism, and a phase separation happening via spinodal decomposition rather than nucleation and growth [32]. The phase inversion is enlightened in Figure 3.3 with close-up picture of the particles as well as a secondary microstructure.

A secondary phase separation is indeed observed in the particles at low fraction of thermoplastic showing a network of $<1\mu\text{m}$ interconnected particles. The primary particles at 5 wt% PCL observed on Figure 3.2 are not composed of pure thermoplastic, but are instead composed on a blend of UP and PCL phase separating during the cure. A secondary morphology is not observed on the sample at 25 wt% of PCL. The morphology obtained at 16.5 wt% of thermoplastic shows PCL rich regions composed of the same secondary microstructure observed on Figure 3.3.a. The critical composition of the system is then approximately located around 16.5 wt% PCL. In such a case, the phase separation is initiated from the cure where the increase in molar mass of the monomer decreases the entropic contribution to the Gibb's free energy creating the primary morphology [27]. In both phases, the formation of microgels (typical curing specificities of unsaturated polyester [28, 33]) will push the PCL away and form a secondary microstructure that depends on the quantity of PCL remaining in the phase. Finally, note that as this system phase separates during the cure, the microstructures are strongly linked to its cure kinetic and changing the curing temperature and/or the amount of additives would affect the size of the morphologies [22].

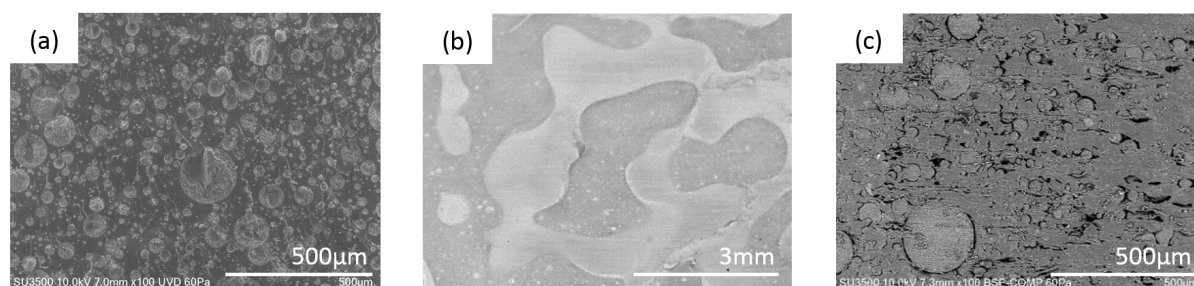


Figure 3.2: Fractured surface showing the phase separated morphologies of PolyLite 31520/PCL blends: (a) 5 wt% PCL, (b) 16.5 wt% PCL and (c) 25 wt% PCL.

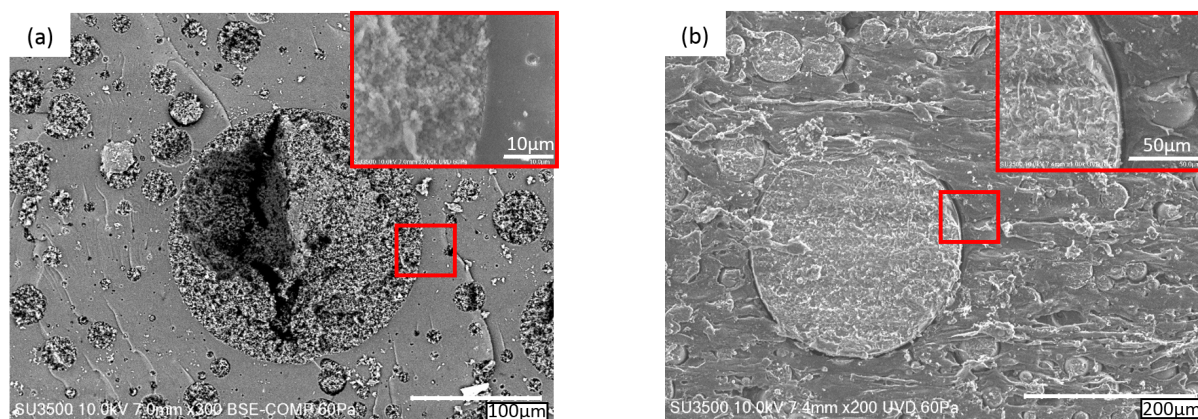


Figure 3.3: Close-up view of the fractured surface showing the morphology of the PolyLite 31520/PCL blends: (a) 5 wt% PCL and (b) 25 wt% PCL.

Temperature/time induced phase separation - PolyLite 31289 and AOC R920

The behaviour observed for the temperature/time induced phase separation is similar to what was observed for the polymerization induced phase separation, and that is true for both PolyLite 31289 and AOC R920. The morphologies obtained for the PolyLite 31289/PCL blends are shown in Figure 3.4. The main difference with what was observed in the last section is the size of the morphologies that are about five times smaller than the one observed with PolyLite 31520. This reduction in size is even more critical on the interconnected microstructure obtained from spinodal decomposition at 7 wt% PCL, where an order of magnitude is observed between the microstructure of PolyLite 31520 and PolyLite 31289. Also note the small quantity of thermoplastic needed to reach the latter morphology when 15 - 17 wt% PCL were needed for the PolyLite 31520 and AOC R920, it is also slightly lower than what is usually observed for blend of UP and PVAc [28, 34]. This difference is probably linked to the initial length of the unsaturated polyester chains, the amount of styrene and to the additives already present in the system. This, however, can hardly be verified without a detailed study of the systems composition and would be

out of the scope of this research. Close-up imaging of the morphologies is shown in Figure 3.5 for the system with 4 and 10 wt% PCL. The secondary morphology observed at 4 wt% PCL shows 3-4 μm interconnected particles in the thermoplastic-rich region. The UP-rich region is composed of thermoset phase with pin-hole thermoplastic particles. The secondary morphology observed in Figure 3.5.b for the system at 10 wt% PCL shows large particles of UP embedded in a thermoplastic-rich matrix that is composed of a secondary phase separated morphology with small particle of UP embedded in a thermoplastic matrix. In this case, it is the reduction of temperature that reduces the miscibility between the two polymers. The secondary morphology is formed during the cure, the already phase separated UP-rich phase will form microgels that will interconnect and crosslink quickly. In the PCL-rich phase, the same UP microgels will form pushing the PCL away forming microparticles of UP (network of microgels) surrounded by a PCL enriched phase. This mechanism will continue until the gel-point, creating the double microstructures seen in Figure 3.5 [28, 33].

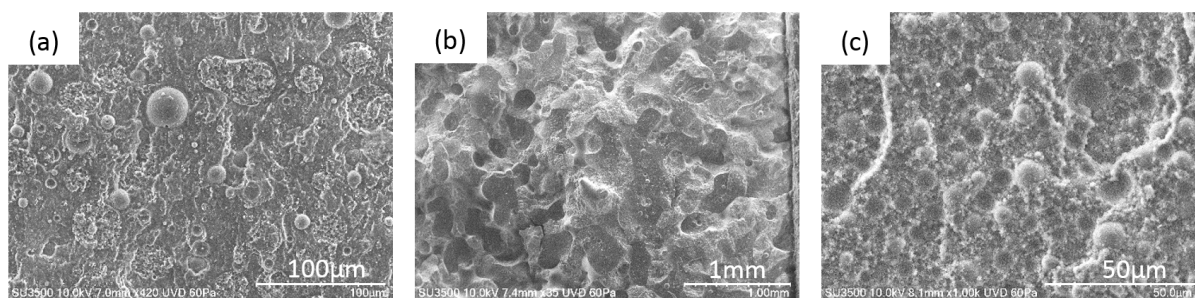


Figure 3.4: Fractured surface showing the phase separated morphologies of PolyLite 31289/PCL blends: (a) 4 wt% PCL, (b) 7 wt% PCL and (c) 10 wt% PCL.

The fraction of PCL was found to have an impact on the size of the particles, especially before the phase inversion happens. This phenomenon is enlightened in Figure 3.6 with morphologies of the AOC R920 blend at 5 and 10 wt% PCL. An increase of the quantity

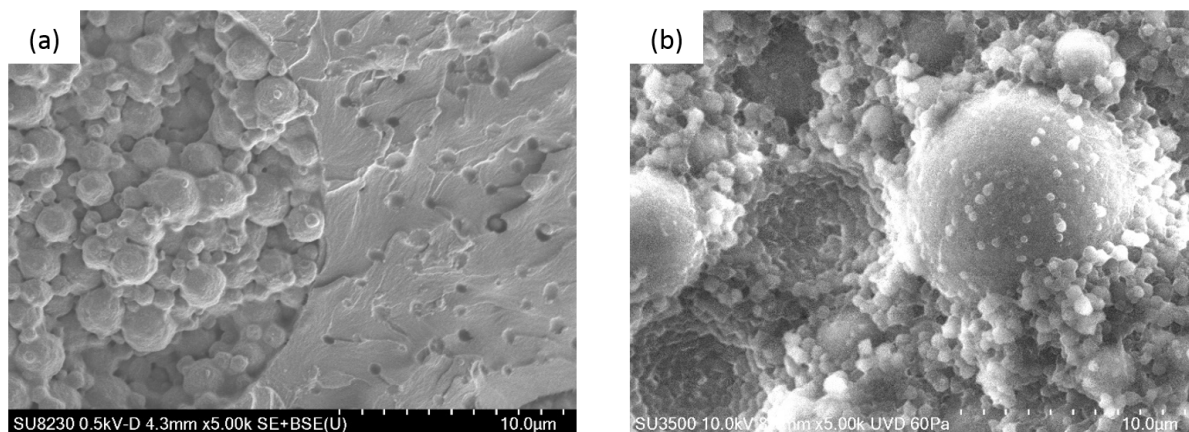


Figure 3.5: Close-up view of the fractured surface showing the morphologies of the PolyLite 31289/PCL blends: (a) 4 wt% PCL and (b) 10 wt% PCL.

of thermoplastic leads to an increase in number of particles and to a reduction in their size with an average particle size of $72 \mu\text{m}$ at 5 wt% and $36 \mu\text{m}$ at 10 wt% PCL. This effect is most probably caused by a change in viscosity reducing the average diffusion distance of the polymer chains. Such a change in scale was also observed with PolyLite 31289 and will affect the mechanical properties of the system. The critical compositions of each resin system are summarized in Table 3.1.

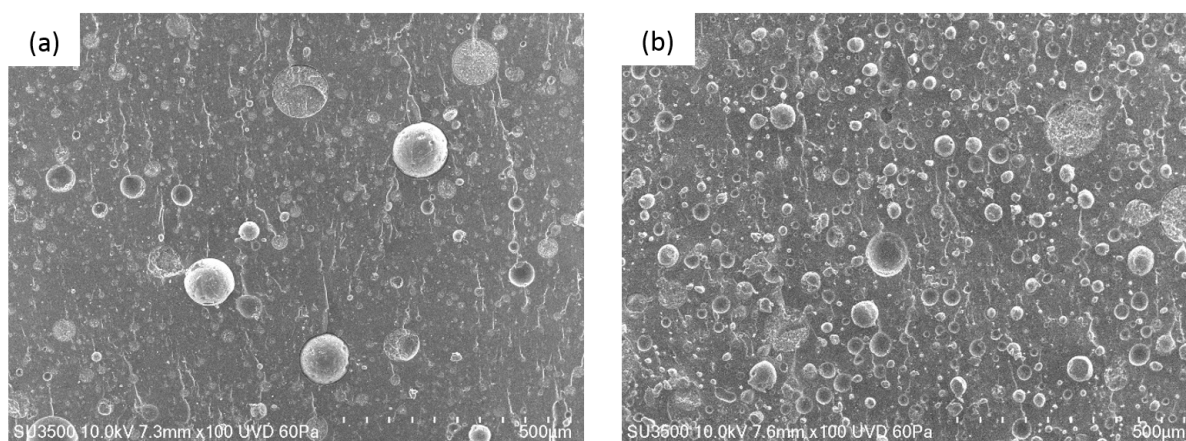


Figure 3.6: Fractured surface showing the morphologies of the AOC R920/PCL blends: (a) 5 wt% PCL and (b) 10 wt% PCL.

Table 3.1: Quantity of PCL required to reach the critical composition.

Resin system	Critical composition [wt% PCL]
Polylite 31520	16.5
Polylite 31289	7
AOC R920	15

3.3.2. SENB and compression tests

The measured toughness of the three different resin systems without graphene is shown in Figure 3.7. The analysis was separated between the polymerization (Polylite 31520) and the temperature/time (Polylite 31289 and AOC R920) induced phase separation for legibility. In the case of the PolyLite 31520, the toughening effect at low thermoplastic content is negligible before the critical composition (< 16.5 wt% PCL) and then increases to a plateau at the critical composition with the creation of an interconnected network of UP-rich and PCL-rich region. The K_{Ic} further increases after the phase inversion to roughly double at 25 wt% of PCL. Note that no tests were carried below 2.5 wt% of thermoplastic with this resin, the strong cure shrinkage fracturing the sample prior demoulding. This behaviour is the opposite of the one observed with the two other resins that show a bell curve behaviour with a strong increase of toughness at low quantity of thermoplastic with a maximum before the critical composition at 4 wt% PCL for the PolyLite 31289 and 5 wt% PCL for the AOC R920. The K_{Ic} then decreases without showing any plateau behaviour linked with a phase change. The primary morphology of the PolyLite 31520 is 3 to 4 times larger than the one observed for the PolyLite 31289, but is one order of magnitude smaller than the one measured on the AOC R920. The analysis of the primary morphology is then not sufficient to explain this difference in behaviour. Especially since the crack propagation

is clearly observed to go from particles to particles (see Figure 3.3), the toughness increase is then not only linked to an increase of tortuosity of the crack path but also to the secondary morphology observed in these particles. The secondary morphology of the particles can be observed in Figure 3.3 and 3.5 for the two Polylyte systems. The first noticeable difference is their size with larger secondary particles for the Polylyte 31289. A smaller interconnected morphology is usually linked to an increase in toughness as it increases the tortuosity of the crack path. The fractured particle in Figure 3.3 shows an evasive crack path starting from the bottom to the top removing part of the particles on its propagation path. That evasive crack path is a sign of a low toughness region with isolated particles connected only by a weak phase. This assumption is further sustained by the absence of particle pull-out on the imaged region, the cracks passing through the particles on every occasion. This is not the case for the Polylyte 31289 where part of the particles are pulled out of the matrix and part are fractured. In this case, the interconnectivity of the secondary morphology is clearly seen in Figure 3.5, explaining the increase of toughness. Here, the decrease of K_{Ic} matches the start of the spinodal decomposition. The secondary morphology of the AOC R920 is on the order of magnitude of the one observed on the Polylyte 31520. However, a change in the rupture mechanism is observed between samples at 5 and 10 wt% of PCL (see Figure 3.6). When most of the particles are sliced through at lower fraction of PCL, most of them are being pulled-out at larger fraction of thermoplastic. A close-up image of the interface between matrix and particles is shown in Figure 3.8.

The particle/matrix interface is found shallow with only a "hair" like structure linking the two regions (see Figure 3.8-red arrow). This explains the moderate increase in toughness of the AOC system compared to the Polylyte 31289. That weak and hollow

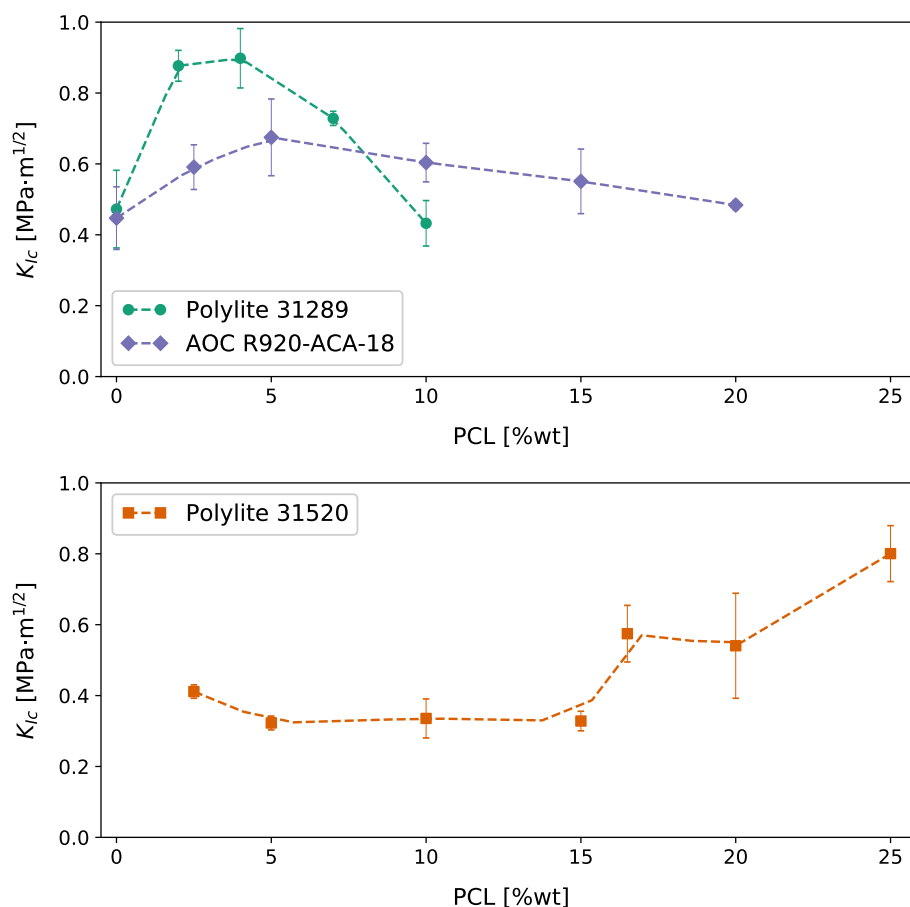


Figure 3.7: Toughness as a function of PCL content measured from SENB tests.

interface is worsened increasing the weight fraction of PCL favouring the pull-out of particles and reducing the toughness of the system even at compositions lower than the critical point. Finally, the increase in toughness obtained with the PolyLite 31289 was in the order of what was observed for an epoxy 5 wt% core-shell rubber blends [35], higher than what was obtained for an UP/Polyethylene-glycol blends at a lower fraction of LPA [36]. Also note that conventional UP/PVAc blends usually don't show any increase in toughness [37].

The compressive yield stress for the three resin systems as a function of the thermoplastic content is shown in Figure 3.9. A strong decrease of the latter is observed for each system

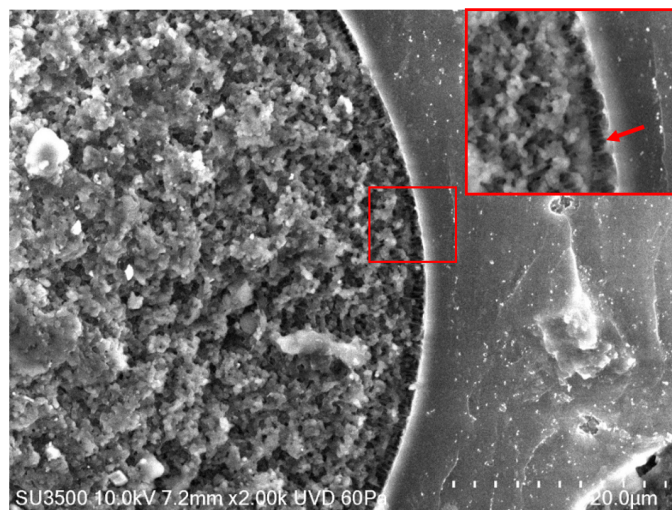


Figure 3.8: Close-up morphologies of the AOC R920 – 5 wt% PCL.

with an increase of PCL. This behaviour, far from the rule of mixture, is highly dependent on the size and homogeneity of the microstructure, the yielding being mostly carried by the PCL-rich phase. The lack of homogeneity due to the large morphology at the critical composition is clearly observed for the PolyLite 31520 with a divergence from a linear behaviour. This waviness of the curve is less observed for the two other systems, keeping in mind the larger deviation, somewhat showing a better homogeneity of the microstructure. The validity of the K_{Ic} measurements was assessed from the compressive yield stress. For all these tests, the condition shown in Equation 3.3 is respected. The tests were then performed in plane strain and measured K_{Ic} are correct. A detailed summary of the results and of the main variables are shown in Table S1, S2 and S3 of the supporting information. To reduce the size of the tables only the average values are displayed, the deviations being low.

3.3.3. Phase separation with graphene

To reduce the number of tests and focus on the effect of the graphene powder on the phase separation and toughness, the rest of the investigation was only carried on the PolyLite

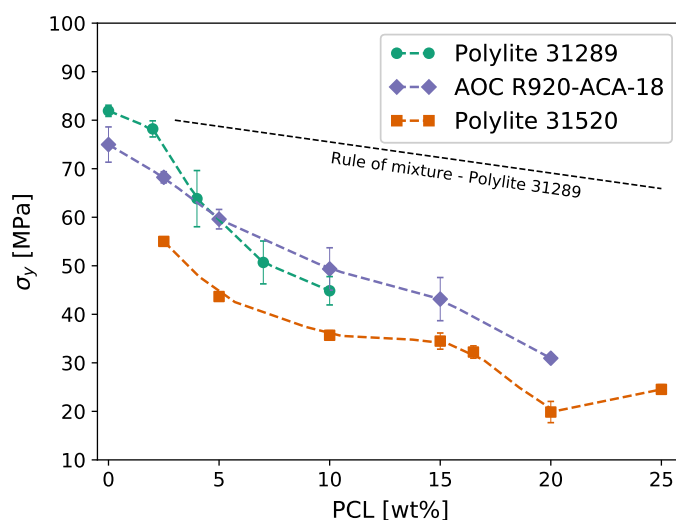


Figure 3.9: Compressive yield stress as a function of the fraction of PCL.

31289 because it was the best performing resin system in term of toughness increase with the lowest fraction of thermoplastic. The dispersion of graphene in the resin is a critical factor that affects the mechanical as well as the electrical properties of the cured system. A good dispersion is then crucial to reach the full potential of mechanical and electrical properties. Optical microscopy images of PolyLite 31289 with 7 wt% PCL before and after dispersion, and after stabilization are shown in Figure 3.10, the graphene being the darker particles. The dispersion observed after mechanical mixing shows large aggregates and a heterogeneous distribution of the graphene. The dispersion step is found effective to homogenize the particles through space and breaks most of the aggregates. Some larger particles are still observed, a closer study suggests that the larger ones are graphite residues coming from the exfoliation rather than agglomerate of primary particles (see Figure S4 and S5 of the supporting information). These larger particles could play an important role in the fracture mechanisms as the π - π interaction between the graphite sheets is weak and can be an easy way for a crack to propagate. The microstructure after stabilization phase separated by spinodal decomposition creating a similar morphology

from what was observed in Figure 3.4.b, the graphene having little to no impact on the phase separation mechanisms. The graphene flakes were observed to be mostly located in the unsaturated polyester rich phase creating a graphene-rich network. That selective distribution follows the thermodynamic approach based on the wetting coefficient proposed by Sumita *et al.* [38]. Such self-assembly network of graphene is interesting to reduce the fraction of graphene needed to reach the electrical percolation threshold and conduction.

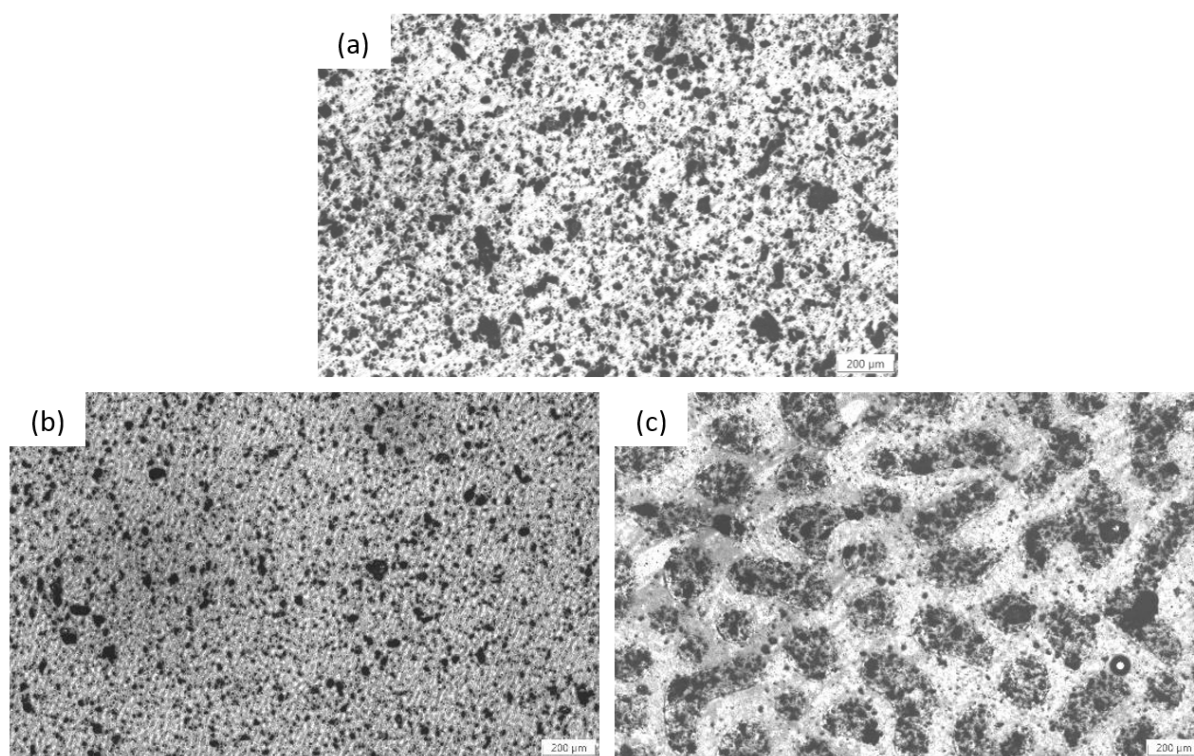


Figure 3.10: Polylite 31289 with 7 wt% PCL and 6 wt% graphene (a) before dispersion, (b) after dispersion and (c) after stabilization.

3.3.4. Coupled effect of graphene and phase separation on toughness and yield stress

Samples were cast with Polylite 31289 blended with 0 to 7 wt% PCL and 0 to 6 wt% of graphene powder to study the coupled effect of the phase separation and graphene on the toughness and yield stress. The obtained K_{Ic} results are displayed in Figure 3.11. The

system without PCL shows a 100 % increase of toughness with the added quantity of graphene going from $0.45 \text{ MPa}\cdot\text{m}^{1/2}$ for the neat resin to $0.91 \text{ MPa}\cdot\text{m}^{1/2}$ with 6 wt% of graphene. The literature usually study toughness with addition of graphene or graphene oxide at content between 0.01 and 2 wt%, showing peak increase of 30 to 100 % [11,39]. The toughness increase obtained here is then equivalent with what is observed in literature with a larger fraction of filler. Two fracture mechanisms are usually observed in a resin containing graphene: (i) crack pinning and (ii) crack deflection and separation of the graphene layers [11]. The first one, happening at low graphene content ($< 2 \text{ wt}\%$), was identified to be responsible for an increase of the crack tortuosity increasing the toughness of the system. This phenomenon can be observed on Figure 3.12 where the central graphene flake forms a clear barrier to the crack propagation. The second mechanism, facilitated at larger fraction of graphene, usually results in a reduction of toughness. The system studied here does not follow these predictions with an increase of toughness measured at higher fraction of graphene. This difference in behaviour is believed to be associated with the quality of the graphene and its rather large number of layers behaving more closely to a carbon black than high purity graphene composite. Indeed, carbon black composites usually exhibit an increase of toughness up to 7–8 wt% of filler before showing a decrease due to the formation of agglomerates [40,41].

It was shown in the previous sections that the addition of PCL was creating a morphology that would increase the cracks surface and energy dissipation increasing the toughness of the system. In the case of a mix of PCL and graphene, the increase of toughness coming from the graphene and the thermoplastic are not cumulative. The increase at low quantity of PCL is principally carried by the graphene when it is damped at

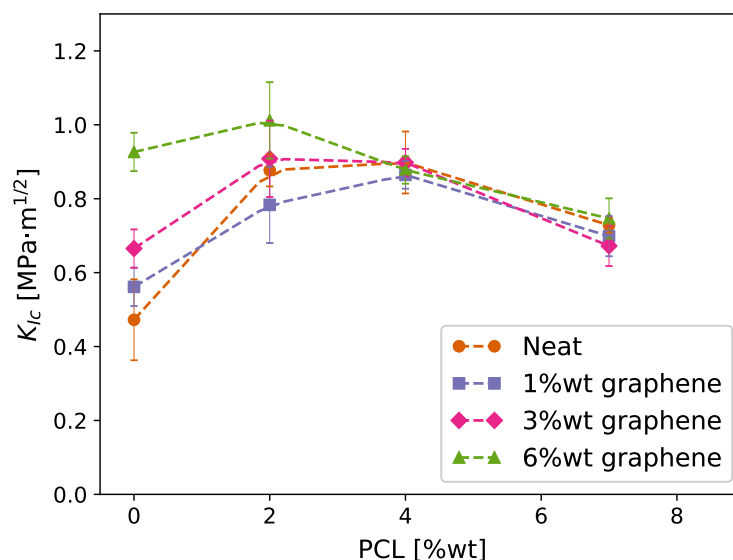


Figure 3.11: Toughness as a function of the fraction of thermoplastic and graphene.

higher fraction of thermoplastic. These observations are in line with what was expected, the UP-rich phase being largely dominant at low PCL content favorizing the graphene effect on toughness. This effect is being reduced before reaching the critical composition where both phases are present in similar quantity. This screening of the graphene's toughening effect at higher PCL content is a sign that the fracture is initiated and propagates principally in the PCL-rich or in between the two phases. The effect of graphene and PCL on the compressive yield stress is shown in Figure 3.13. The effect of graphene on σ_y is negligible up to 3 wt% of filler. At larger quantity of filler, the particles could act as a concentration region for residual stresses having a slight decreasing effect on the yield stress. Tests with larger quantity of graphene would be needed to verify this tendency. The low effect of graphene on the compressive yield stress is a sign that yielding is principally carried by the softer PCL-rich phase. These tests validate the K_{Ic} values measured by SENB according to Equation 3.3, the detailed results are shown in Table S5 of the supporting information. To reduce the size of the table only the average values are

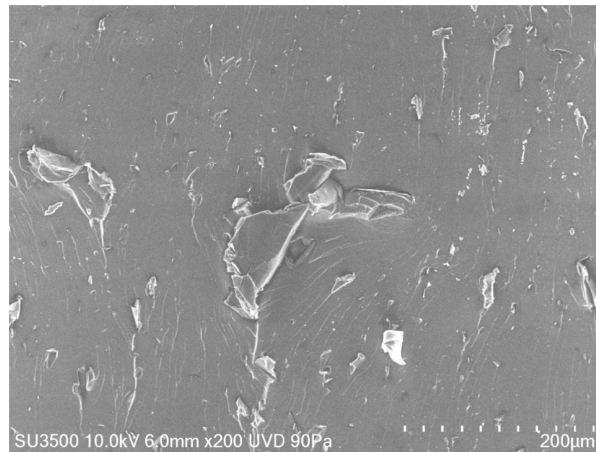


Figure 3.12: Fractured surface of neat UP with 1 wt% of graphene showing the crack pinning mechanism.

displayed, the deviations being low.

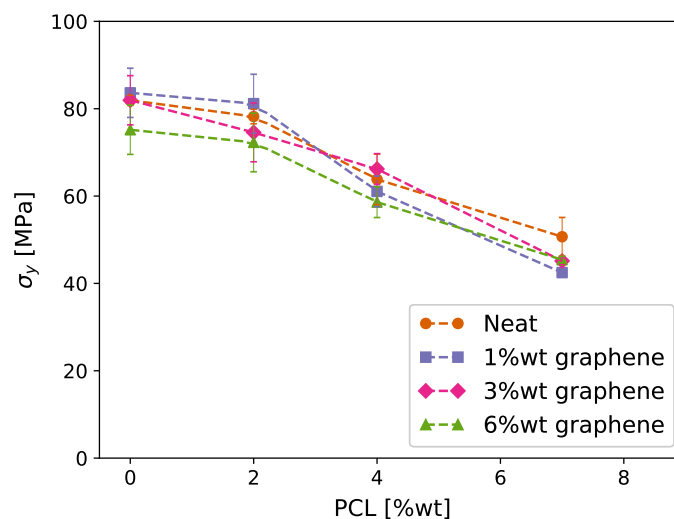


Figure 3.13: Compressive yield stress as a function of the fraction of thermoplastic and graphene.

3.3.5. Effect of graphene network on the electrical conductivity

The effect of graphene and PCL on the electrical conductivity is displayed in Figure 3.14.

Three main stages are expected: (i) insulating, where no direct network of filler is present, precluding any charge flow, (ii) percolating, where conduction happens via tunneling

between the filler and the matrix and (iii) conducting, where a direct network of filler carry the charge flow [42]. For the neat resin, the addition of graphene only affects slightly the conductivity until 8–9 wt% of graphene where the percolation threshold is observed. The conductivity then steeply increases to reach a plateau at $\sim 10^{-5}$ S/cm. This behaviour matches what was found in literature, to the exception of the quantity of filler necessary to reach the percolation threshold. The measured conductivity of graphene-based thermoset composite is usually reported ranging from 10^{-8} S/m at 0.16 vol% to 0.1 S/cm at 4 vol% of graphene [19], the value measured here is however consistent with researches conducted with similar graphene powder [43]. The behaviour of the samples with PCL is different, when the 3 wt% PCL follow the trend of the neat resin, a shift of the percolation threshold is observed for the system with 7 wt% PCL, the latter composition creating a co-continuous network of UP and PCL. The graphene being mostly located in the UP-rich phase, the quantity of filler needed for percolation is reduced. The system then shows a double percolation behaviour, a first one coming from the microstructure issued from the phase separation and the second one from the graphene network [14, 17]. This shift is clearly observed on Figure 3.14 with, for example, an electrical conductivity nine orders of magnitude higher for the sample with 7 wt% PCL at 8 wt% graphene compared to the two other compositions.

3.4. Conclusion

In this study, the toughness of three unsaturated polyester (UP) resin modified with different quantities of polycaprolactone (PCL) (0 – 25 wt%) and few-layer graphene microsheets (0 – 6 wt%) were characterized by single-edge-notch bending. A maximum

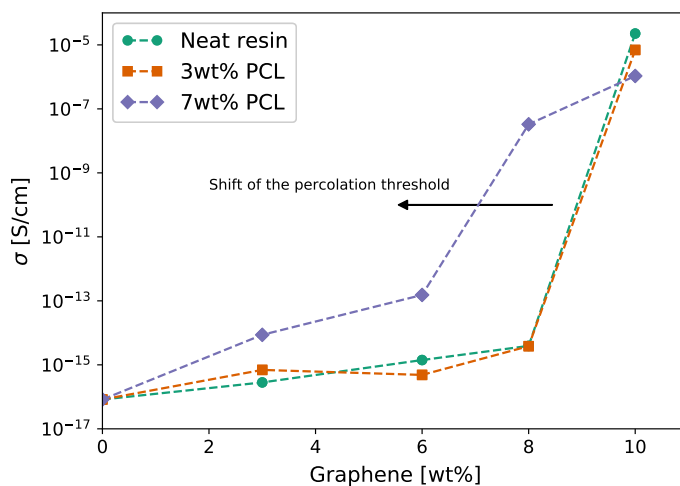


Figure 3.14: Electrical conductivity as a function of the PCL and graphene content.

toughening effect linked to the addition of the low-profile-additive was measured from $0.472 \text{ MPa}\cdot\text{m}^{1/2}$ for the neat resin to $0.898 \text{ MPa}\cdot\text{m}^{1/2}$ with the addition of 4 wt% of PCL. At this composition the phase separation occurring between the UP and PCL created a dispersion of softer PCL-rich particles in a matrix of UP. When fracture occurred, the crack went from particles to particles increasing the tortuosity of the crack path compared to the fracture of a neat UP sample leading to a higher toughness. The addition of graphene to the neat resin had a substantial impact on K_{Ic} increasing with the fraction of filler up $0.926 \text{ MPa}\cdot\text{m}^{1/2}$ with 6 wt% of graphene. This phenomenon observed even at large quantity of graphene is in opposition with what is usually seen in literature with a decrease in toughness observed at composition larger than 2 wt% due to a fracture by crack deflection. This difference was associated to the quality of the graphene and its larger number of layers compared to high purity graphene used in other studies. The latter favouring a fracture by crack pinning leading to an increase in toughness. The addition of graphene to a UP/PCL blend lead to the creation of a self-assembly network of graphene located at the UP-rich phase. Such structure showed an increase in toughness compared to

the isolated effect of PCL and graphene with a maximum K_{Ic} measured at $1.012 \text{ MPa}\cdot\text{m}^{1/2}$ with 2 wt% of PCL and 6 wt% of graphene. The effect of the PCL and graphene on the toughness were not additive, the crack propagation principally occurring between the larger graphene particles at low PCL content. At larger quantity of PCL, the effect of graphene was screen by the larger phase-separated morphology and only the impact of the PCL on the toughness was observed. The electrical conductivity was, however, strongly affected by such self-assembly network of graphene shifting the percolation from 9 to 7 wt% of graphene at 7 wt% of PCL thanks to the creation of a co-continuous microstructure of UP-rich and PCL-rich regions. Future work will be conducted regarding the processing of such resin system into glass-fibre composites and study their mechanical and electrical properties in the final goal to create self-sensing materials.

Acknowledgement

The authors thank their funding partners, NanoXplore Inc. for donating the graphene and polyester resins, and Ingevity for donating the thermoplastic. Thanks to Dr. Maryam Golozar from the McGill Electron Microscopy Research Group of Prof. Raynald Gauvin for the SEM images.

Funding

This work was supported by the Werner Graupe Fellowship, the Natural Sciences and Engineering Research Council of Canada (NSERC) grant RDCPJ 530253-18, Prima Quebec grant R16-46-005, the Research Center for High Performance Polymer and Composite Systems (CREPEC) and NanoXplore Inc..

References

- [1] P. M. Gary and M. G. Riskalla. Vought aircraft company and u.s. department of transportation, dallas and washington dc. *Vought Aircraft Company and U.S. Department of Transportation, Dallas and Washington DC*, 1997.
- [2] D. J. Lekou. *Scaling Limits and Costs regarding WT blades - EC Project UpWind*. Centre for Renewable Energy Sources, Pikermi, 2010.
- [3] MarketsAndMarkets. *Composite Repairs Market by Type (Structural, Semi-Structural, Cosmetic), Process (Hand Lay-Up, Vacuum Infusion, Autoclave), End-Use Industry (Aerospace & Defense, Wind Energy, Automotive & Transportation), and Region - Global Forecast to 2026*. 2017.
- [4] F. Mutel. *Overview of the global composites market - at the crossroads*. JEC Group, 2017.
- [5] S. Qu, Y. Dai, D. Zhang, Q. Li, T.-W. Chou, and W. Lyu. Carbon nanotube film based multifunctional composite materials: an overview. *Functional Composites and Structures*, 2020.
- [6] A. Ali and A. Andriyana. Properties of multifunctional composite materials based on nanomaterials: a review. *RSC Advances*, 2020.
- [7] D. G. Papageorgiou, I. A. Kinloch, and R. J. Young. Mechanical properties of graphene and graphene-based nanocomposites. *Progress in Materials Science*, 2017.
- [8] A. Yasmin, J.-J. Luo, and I. M. Daniel. Processing of expanded graphite reinforced polymer nanocomposites. *Composites science and technology*, 2006.
- [9] I. Zaman, T. T. Phan, H.-C. Kuan, Q. Meng, L. T. B. La, L. Luong, O. Youssf, and J. Ma. Epoxy/graphene platelets nanocomposites with two levels of interface strength. *Polymer*, 2011.
- [10] M. H. A. Kudus, M. R. Zakaria, M. B. H. Othman, and H. M. Akil. Preparation and characterization of colloidized diamine/oxidized- graphene via condensation polymerization of carboxyl groups epoxy/ oxidized-graphene nanocomposite. *Polymer*, 2017.
- [11] S. Chandrasekaran, N. Sato, F. Tölle, R. Mülhaupt, B. Fiedler, and K. Schulte. Fracture toughness and failure mechanism of graphene based epoxy composites. *Composites Science and Technology*, 97:90–99, 2014.
- [12] H. Yui, G. Wu, H. Sano, M. Sumita, and K. Kino. Morphology and electrical conductivity of injection-molded polypropylene/carbon black composites with addition of high-density polyethylene. *Polymer*, 2006.
- [13] F. Gubbels, R. Jérôme, Ph. Teyssié, E. Vanlathem, R. Deltour, A. Calderone, V. Parenté, and J. L. Brédas. Selective localization of carbon black in immiscible polymer blends: A useful tool to design electrical conductive composites. *Macromolecules*, 1994.

- [14] M. Sumita, K. Sakata, Y. Hayakawa, S. Asai, K. Miyasaka, and M. Tanemura. Double percolation effect on the electrical conductivity of conductive particles filled polymer blends. *Colloid & Polymer Science*, 270:134–139, 1992.
- [15] Y. Zhang, Y. Shen, K. Shi, T. Wang, and E. Harkin-Jones. Constructing a filler network for thermal conductivity enhancement in epoxy composites via reaction-induced phase separation. *Composites Part A*, 2018.
- [16] G. Yu and P. Wu. Effect of chemically modified graphene oxide on the phase separation behaviour and properties of an epoxy/polyetherimide binary system. *Polymer Chemistry*, 2014.
- [17] C. Guo Ma, D. Yong Xi, and M. Liu. Epoxy resin/polyetherimide/carbon black conductive polymer composites with a double percolation structure by reaction-induced phase separation. *Journal of Composite Materials*, 47:1153–1160, 2013.
- [18] H. Kishi, S. Tanaka, Y. Nakashima, and T. Saruwatari. Self-assembled three-dimensional structure of epoxy/polyethersulphone/silver adhesives with electrical conductivity. *Polymer*, 2016.
- [19] A. J. Marsden, D. G. Papageorgiou, C. Vallés, A. Liscio, V. Palermo, M. A. Bissett, R. J. Young, and I. A. Kinloch. Electrical percolation in graphene-polymer composites. *2D Materials*, 5, 2018.
- [20] C. B. Bucknall, I. K. Partridge, and M. J. Phillips. Morphology and properties of thermoset blends made from unsaturated polyester resin, poly(vinyl acetate) and styrene. *Polymer*, 32:786–790, 1991.
- [21] M. Kinkelaar, B. Wang, and L. J. Lee. Shrinkage behaviour of low-profile unsaturated polyester resins. *Polymer*, 35:3011–3022, 1994.
- [22] X. Bulliard, V. Michaud, and J. A. E. Manson. Reaction-induced phase separation in poly(vinyl acetate) /polyester blend. *Journal of Applied Polymer Science*, 102:3877–3888, 2006.
- [23] NanoXplore Inc. Technical data sheet - grapheneblack3x ds-gb3x-210803. Technical report, 2021.
- [24] A. Bianco, H.-M. Cheng, T. Enoki, Y. Gogosti, R. H. Hurt, N. Koratkar, T. Kyotani, M. Monthieux, C. R. Park, J. M. D. Tascon, and J. Zhang. All in the graphene family - a recommended nomenclature for two-dimensional carbon materials. *Carbon*, I(6), 2013.
- [25] P. Wick, A. E. Louw-Gaume, M. Kucki, H. F. Krug, K. Kostarelos, B. Fadeel, K. A. Dawson, A. Salvati, E. Vazquez, L. Ballerini, F. Tretiach, M.; Benfenati, E. Flahaut, L. Gauthier, M. Prato, and A. Bianco. Classification framework for graphene-based materials. *Angewandte Essays*, 53:7714–7718, 2014.
- [26] R. Koningsveld, W. H. Stockmayer, and E. Nies. *Polymer Phase Diagrams - A Textbook*. 2001.

- [27] R. Williams, B. Rozenberg, and J. Pascault. Reaction-induced phase separation in modified thermosetting polymers. *Advances in Polymer Science*, 128:95–156, 1997.
- [28] C. B. Bucknall, P. Davies, and I. K. Partridge. Phase separation in styrenated polyester resin containing a poly(vinyl acetate) low-profile additive. *Polymer*, 26:109–112, 1985.
- [29] Y. Hsieh and T. Yu. Phase separation of unsaturated polyester resin blended with poly(vinyl acetate). *Journal of Applied Polymer Science*, 73:2413–2428, 1999.
- [30] J.-P. Dong, J.-G. Huang, F.-H. Lee, J.-W. Roan, and Y.-J. Huang. Effects of poly(methyl methacrylate)-based low-profile additives on the properties of cured unsaturated polyester resins. i. miscibility, curing behavior, and glass-transition temperatures. *Journal of Applied Polymer Science*, 91:3369–3387, 2004.
- [31] S. Thomas, M. Hosur, and C. J. Chirayil. *Unsaturated polyester resins: blends, interpenetrating polymer networks, composites, and nanocomposites*. 2019.
- [32] L. Utracki and C. Wilkie. *Polymer blends handbook*. Springer, 2014.
- [33] L. Suspène, D. Fourquier, and Y.-S. Yang. Application of phase diagrams in the curing of unsaturated polyester resins with low-profile additives. *Polymer*, 1991.
- [34] M. Ruffier, G. Merle, J. P. Pascault, H. Bouleçane, and N. Vincent. The shrinkage compensation of unsaturated polyester resins- polyvinyl acetate blends polymerization proceeds through fractal morphologies: characterization and simulation. *Journal of material science*, 1996.
- [35] H. Kishi, S. Matsuda, J. Imade, Y. Shimoda, T. Nakagawa, and Y. Furukawa. The effects of the toughening mechanism and the molecular weights between cross-links on the fatigue resistance of epoxy polymer blends. *Polymer*, 2021.
- [36] A.B. Cherian and E. T. Thachil. Modification of unsaturated polyesters using polyethylene glycol. *Plastics, Rubber and Composites*, 2007.
- [37] J. C. Lucas, J. Borrajo, and R. J. J. Williams. Cure of unsaturated polyester resins: 2. influence of low-profile additives and fillers on the polymerization reaction, mechanical properties and surface rugosities. *Polymer*, 1993.
- [38] M. Sumita, K. Sakata, S. Asai, K. Miyasaka, and H. Nakagawa. Dispersion of fillers and the electrical conductivity of polymer blends filled with carbon black. *Polymer Bulletin*, 25:265–271, 1991.
- [39] S. He, N. D. Petkovich, K. Liu, Y. Qian, C. W. Macosko, and A. Stein. Unsaturated polyester resin toughening with very low loadings of GO derivatives. *Polymer*, 2017.
- [40] R. Dungani, I. Sumardi, E. M. Alamsyah, P. Aditiawati, T. Karliati, J. Malik, and Sulistyono. A study on fracture toughness of nano-structured carbon black-filled epoxy composites. *Polymer Bulletin*, 2020.

- [41] S. H. Kim, S. J. Park, K. Y. Rhee, and S. J. Park. Effects of ozonized carbon black on fracture and post-cracking toughness of carbon fiber-reinforced epoxy composites. *Composites Part B*, 177, 2019.
- [42] I. Balberg. *Semiconducting polymer composites: Principles, morphologies, properties and applications*, chapter Percolation theory and its application in electrically conducting materials, pages 145–169. 2013.
- [43] F. Serenari, M. Madinehei, N. Moghimian, D. Fabiani, and E. David. Development of reinforced polyester/graphene nanocomposite showing tailored electrical conductivity. *Polymers*, 12, 2020.

PREFACE – CHAPTER 4

The following chapter study the processing of blends developed in Chapter 3 into composite plates. The processing of graphene-based composite is especially challenging by compression resin transfer moulding (cRTM), as the fibre geometry can introduce filtering effects leading to a heterogeneous distribution of the graphene throughout the plate. Other factors as the rapid cure of unsaturated polyester as well as the increased viscosity due to the added graphene and thermoplastic can greatly influence the good impregnation of the fibre preform, and need to be optimized. Finally, the effect of temperature, pressure and fibres on the morphology of phase-separation need to be addressed to ensure the reliability of the processing method and homogeneity of the final part.

CHAPTER 4

Processing of a multiscale multiphase composite.

N. Hostettler, P. Hubert, Canadian-International Conference on Composites (2022)

Keywords: Graphene; Multiphase; Manufacturing

4.1. Introduction

Graphene enhanced composites are strong candidates to solve uncontrolled damage propagation in composites as they were found to increase the toughness and electrical conductivity of the matrix. The latter enabling sensing by continuous resistivity measurements, tracking the damage progression in the part [1]. When high quality graphene is too expensive for large part processing, more affordable few-layer graphene, produced at industrial volumes, would be needed in larger quantity to reach equivalent toughening and electrical properties increasing the risk of filtering effect and reaggregation during processing [2]. The increase in viscosity linked to the use of large quantity of graphene can be a challenge to the good impregnation of the fibre preform impacting the mechanical properties of the cured part. Blending the thermoset resin with a thermoplastic low-profile additive (LPA) in a control manner can create a self-assembly network of graphene and is a solution to shift the percolation threshold toward lower quantity of particles [3,4]. However, the resulting increase of viscosity could lead to fibre infiltration issues. Furthermore, phase separations can be sensible to pressure and a bad

control over the process could simply ruin the formation of a graphene network by shifting the critical point of phase separation toward lower quantity of thermoplastic [5]. In such a case, the critical concentration of graphene at the percolation threshold would increase, the graphene being trapped into isolated nodules of thermoset resin. The objective of this research is to study the effect of the processing cycle on the impregnation of the fibre preform by an unsaturated polyester resin system produced by compression resin transfer moulding (cRTM). The effect of fibres, pressure and graphene content on the phase separated morphology will be studied. The influence of the fibre architecture on the graphene filtration will be discussed. The final goal being to have an optimized processing cycle for a reliable production of quality multiscale multiphase composite plates.

4.2. Materials and Methods

Preparation of the resin system

The resin system used in this research was the PolyLite 31289, a pre-accelerated unsaturated polyester from Reichhold that was cured with 2 wt% of Norox Azox from United-initiator ($t_{gel} = 3$ min). The thermoplastic LPA was the CAPA 6500 from Ingevity a polycaprolactone (PCL) with a mean molecular weight of 50'000 g/mol. The graphene powder was the GrapheneBlack 3X from NanoXplore inc., a mass-produced industrial graphene with a primary particle size between 1–2 μm and mean agglomerates size of D50 < 30 μm . The particles are between 6 to 10 graphene-layers thick with a carbon to oxygen ratio of 96:1 and a bulk density of 0.2 – 0.3 g/cm^3 [6]. Based on the classification framework proposed by Bianco et al. [7], Wick et al. [8] and the ISO/TS 21356 – 1:2021, this graphene powder is classified as few-layer graphene nanoplatelets. The resin system

was produced as follow: (i) the desired quantity of graphene was weighted and added to the neat resin, (ii) 1 wt% of a mixture of Styrene/15 wt% Triton X100 was added to the resin as a surfactant to help dispersing the graphene, (iii) the system was dispersed with a probe sonicator (Hielscher UP400St) for two cycles of 7 min spaced by a 15 min cool down step to limit the increase in temperature, (iv) the jar was then transferred into a 65 °C preheated water bath where the desired quantity of PCL pellets was added and mixed for 20 min at 1500 rpm until fully dissolved, (v) the system was let to rest at room temperature for 20 min to stabilize the phase separated morphology, (vi) 2 wt% of initiator was incorporated in the system before degassing for 1–2 min to be ready for processing.

Fibre and compression moulding

To understand the influence of the moulding parameters on the apparition of defects, several moulding cycles were tested on a bidirectional-glass-complex 0/90/Mat preform with a nominal superficial density of 910 g/m² from SAERTEX. To put in perspective the observations of the fibre architecture's effect on the filtering of graphene particles, other tests were performed on a twill weave from Hexcel with a nominal superficial density of 295 g/m². The details of the stacking configuration as well as the target thickness is shown in Table 4.1. The processing of the plates was conducted by compression resin transfer molding on an MTS 250 kN press in a 100x100 mm open square mould (see Figure 4.1). The surface of the mould was cleaned with isopropanol and robbed with Chemlease 2752W from ChemTrend to help with the demoulding process. The compression was conducted as follow: (i) the empty mould was closed to set the zero distance, it was then open back to the starting position, (ii) Teflon tape was applied on the junction in the bottom of the mould to avoid any resin leakage, the fibre perform was then set in the

mould, (iii) the resin system was poured on top of the fibres and the system was compressed at 0.05 mm/s (last 10 mm) until reaching a thickness corresponding to a volume fraction of fibre equal to $V_f = 0.4$. Note that 1.3 times the theoretical amount of resin was used to counterbalance the resin leakage during processing. The plates were then post-cured at 120 °C for 2 h to finish the cure. The optimization of the cure cycle was performed looking at optical microscopy of polished samples.

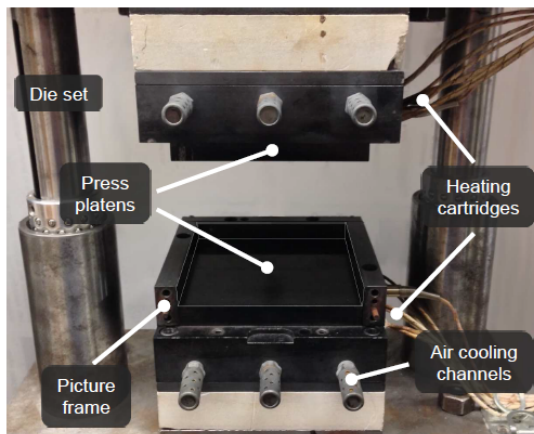


Figure 4.1: Square mould used for the processing of the plates (the front part was removed for the picture). [9]

Table 4.1: Details of the fibre nominal superficial density, stack and target thickness for $V_f = 0.4$.

	ρ_s [g/cm ²]	Stack	t_{target}
Complex	910	[Mat,90,0] _s	1.78
Weave	295	[0,90] _{3s}	1.73

4.3. Results and Discussion

Optimization of the moulding cycle and fibres impregnation

The used compression method has several issues when it comes to compression resin transfer moulding. Firstly, the use of an open mould allows for the resin to escape the cavity, the effective moulding pressure is then mostly uncontrolled. Therefore, the moulding cannot be conducted with a control in force but with a control in the final thickness of the plate only. The first tests were conducted with the complex fibres and a mould at 40 °C, the pressure profile as well as an optical microscopy of the samples are

shown in Figure 4.2. The pressure profile shows a peak at 0.55 MPa resulting in mostly dry fibre tows, when the space between the tows is adequately filled with resin. In order to increase the effective moulding pressure, a metallic shim was added to create a pinching zone surrounding the fibre bed. The shim was a 3.8 mm thick steel frame with an outer and inner length of 100 and 80 mm respectively. This low permeability region should help the resin stay in the mould and help impregnating the fibre tows. The pressure profile as well as an optical microscopy of the samples are shown in Figure 4.2.a and 3c respectively. The first difference with the shim-less configuration (Figure 4.2.b) is the moulding pressure that was increased with the shim to 0.85 MPa. This is resulting in a better impregnation of the fibre tows visible in Figure 4.2.c; however, when some regions are well impregnated, some others are still containing numerous voids. This is a sign that the applied pressure is still too low and/or that the resin is curing too quickly, not letting for the resin to reach the center of each tow before the gel point. A tow impregnation model was used to have an insight of the time required to impregnate the fibre preform [10]:

$$\frac{d\beta}{dt} = \frac{K}{\mu R_{tow}^2 (1 - V_f)} \left(\frac{P_\infty - P_f}{(1 - \beta) \ln(1/(1 - \beta))} \right) \quad (4.1)$$

with β is the degree of impregnation ($0 \leq \beta \leq 1$), R_{tow} is the circular equivalent tow radius, K is the permeability of the preform, μ is the viscosity of the resin system, V_f is the fibre volume fraction in the tow, P_∞ is the applied pressure and P_f is the internal pressure.

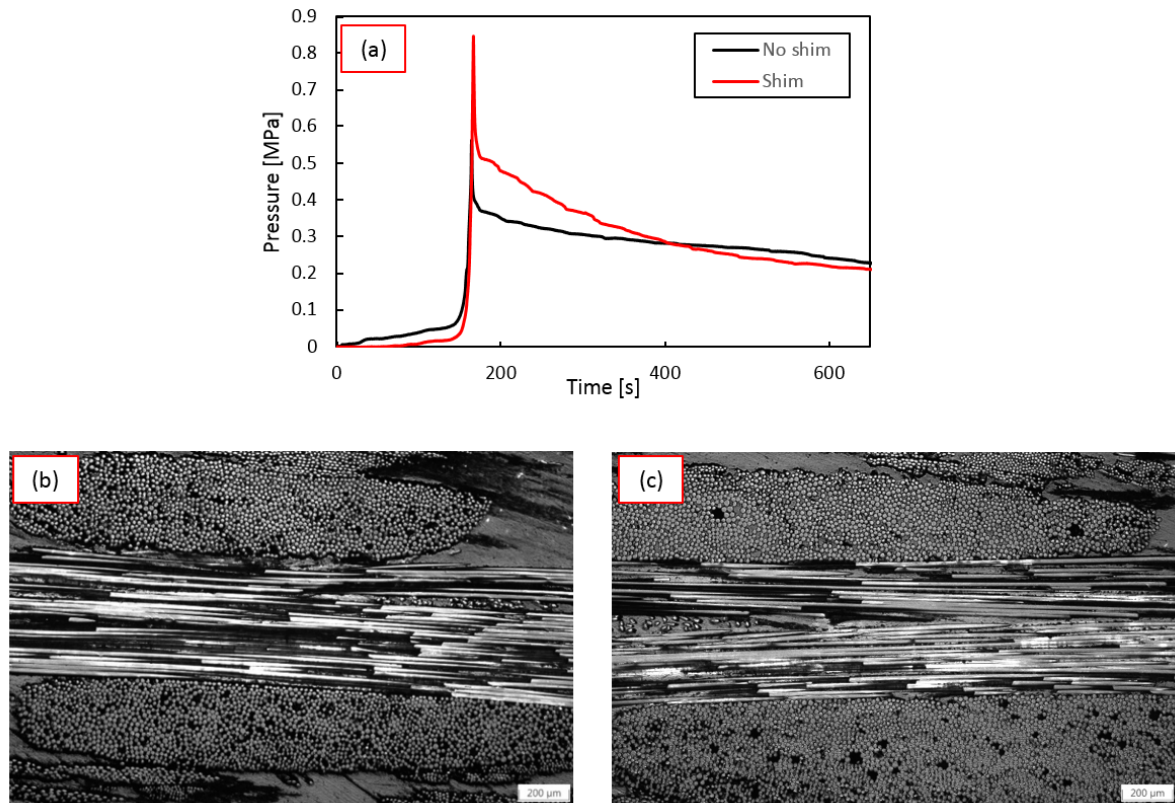


Figure 4.2: (a) pressure evolution during processing and optical microscopy images of the plate (b) 40 °C without shim, (c) 40 °C with shim.

For simplicity, the capillary pressure contribution was omitted and P_f was considered to be the atmospheric pressure, giving a worst-case scenario configuration where the resin doesn't wet the fibres. The increase of viscosity coming from the cure of the resin was also omitted and the tow transverse permeability was estimated from analytical equations proposed by Gebart et al. [11], for simplicity. The equivalent fibre tow radius was calculated as follow:

$$R_{tow} = \sqrt{2} \frac{a_0 b_0}{\sqrt{a_0^2 + b_0^2}} \quad (4.2)$$

Figure 4.3 is a schematic diagram of a fiber tow. It is an oval shape filled with a grid of small circles representing individual fibers. Two red arrows indicate the dimensions: a horizontal arrow labeled a_0 representing the tow width and a vertical arrow labeled b_0 representing the tow height.

Figure 4.3: Schematic for the measurement of R_{tow} .

where a_0 and b_0 is the tow width and high respectively (Figure 4.3). The values used in

equation 4.1 are summarized in Table 4.2, the evolution of the degree of impregnation with time and applied pressure are shown in Figure 4.4. The system pressed at 0.55 MPa would require 6 min to be fully impregnated. When this value does not seem excessive, it is dramatic for the resin system studied here that reaches its gel point in approximately 3 min. The compression with the shim at 0.85 MPa would need 3.5 min to be fully impregnated. This value, close to the experimental gel time, is in line with what can be observed in Figure 4.2.c with region fully impregnated (mostly at the top of the plate) and others containing lots of voids (mostly at the bottom of the plate). In such configurations, the applied pressure is then not high enough to have a full impregnation of the fibre. In a second step, the moulding pressure was increased by setting a much higher pressure during the zeroing of the thickness before the moulding (step (i) of the moulding process). Indeed, it was noticed that using a higher pressure during this zeroing step allows to reach high pressure during the moulding step, due to the configuration of the mould. The same tests were then conducted reaching a pressure of 12 MPa (1 MPa previously) during the zeroing step. Such pressure would impregnate the fibre tows in a few seconds according to the tow impregnation model (see Figure 4.4).

Table 4.2: Parameters used in the tow impregnation model.

K [m ²]	$1.5 \cdot 10^{-14}$
R_{tow} [m]	$2.5 \cdot 10^{-4}$
μ [Pa·s]	0.17
V_f	0.7
P_f [Pa]	10^5

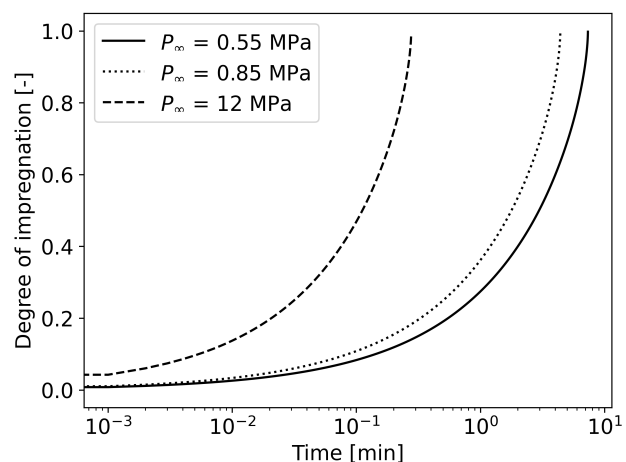


Figure 4.4: Degree of impregnation as a function of time and applied pressure.

Two temperature cycles were tested, the first one with a hot moulding at 40 °C and another one moulding at room temperature leaving the system to “rest” for 15 min and then cure the system at 50 °C for 10 min. The goal of such comparison was to verify that the quality of the plates cured with a hot mould are equivalent with the “perfect” plates moulded at room temperature. The pressure evolution in each case and optical microscopy images of the samples are shown in Figure 4.5. The red arrow in Figure 4.5.a shows the bump linked with the start of the cure.

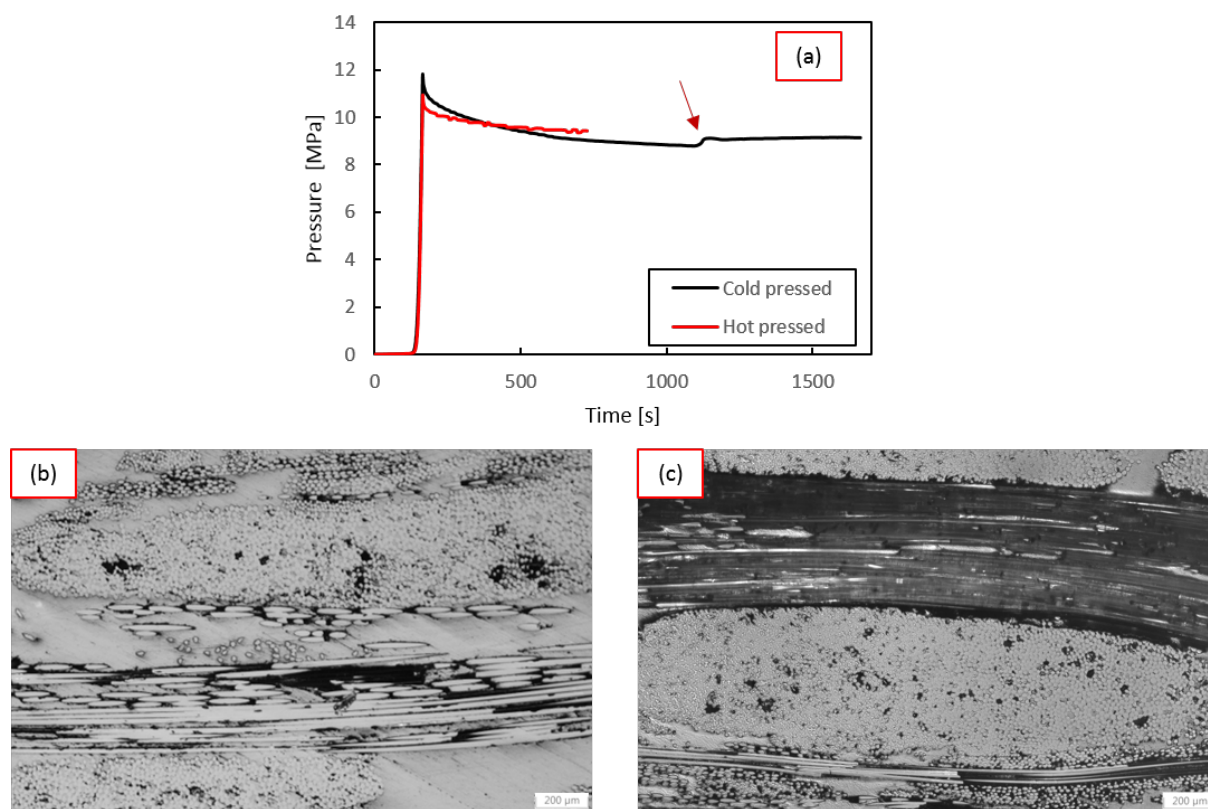


Figure 4.5: (a) pressure evolution during processing and optical microscopy images of the plate with a zero-thickness at 12 MPa (b) cold pressed with shim, (c) 40 °C with shim.

Increasing the target load setting the zero thickness indeed increased the moulding pressure. The resulting impregnation is also well improved compared to the lower pressure case shown previously. The center of the tow in each case is well impregnated, following the prediction from the tow impregnation model. Some voids are, however, still observed

but they are attributed to the open mould setup where it is difficult to process void free plates. The hot-pressed sample shows a dark transverse fibre tow (see Figure 4.5.c). This most probably comes from the polishing of the sample that pullout out the longitudinal fibres. Both strategies look equivalent and can be used to have a full impregnation of the fibre preform. The cold-pressed strategy was chosen for the rest of the tests because it integrates better into the resin preparation workflow.

Effect on the phase separation

Two possible phenomena could have an influence on the phase separation during the compression process: (i) the increase of pressure affecting the thermodynamic of phase separation (shift of critical point), changing the resulting morphology and (ii) the selective suction of either polymers by the fibre tows that could locally increase/decrease the fraction of thermoplastic in between the tows, as well changing the phase-separated morphology. To have a better understanding of the effect of fibres on the phase separation, Figure 4.6 shows the microstructure of a UP – 8 wt%PCL blend. The fibre tows are surrounded by the UP-rich region, the PCL-rich region showing no wetting of the fibre. However, there still PCL-rich region in between the fibres (see Figure 4.6 red arrow). The repartition of the phase in the fibre tows seems to reflect what was observed in the space in between the tows. There is then no local change in composition effecting the phase separation.

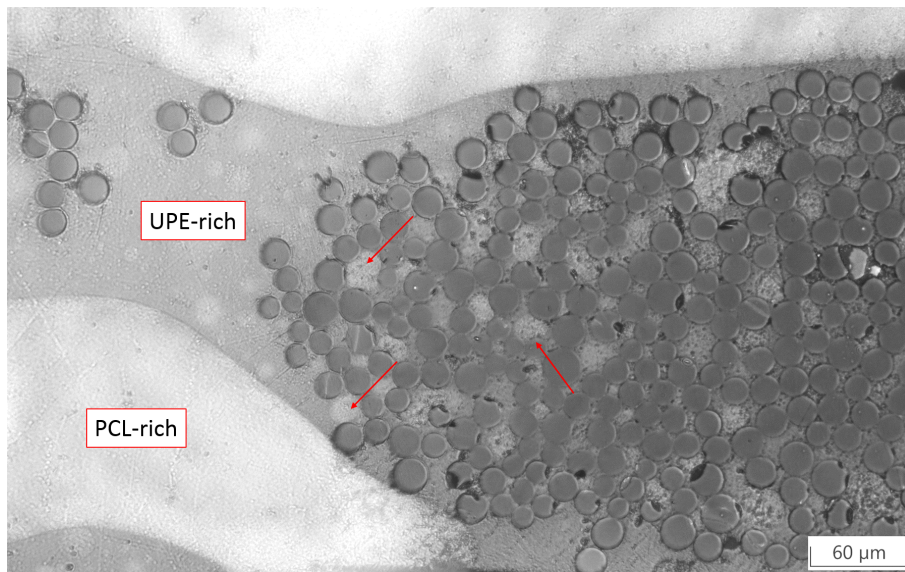


Figure 4.6: Microscopy image of a UP – 8 wt%PCL.

A comparison between two blends with 4 and 7 wt%PCL with and without fibres is shown in Figure 4.7. The phase separated morphology was similar between the systems with and without fibres, confirming that the presence of fibre and the high moulding pressure was not visibly affecting the thermodynamic of phase separation.

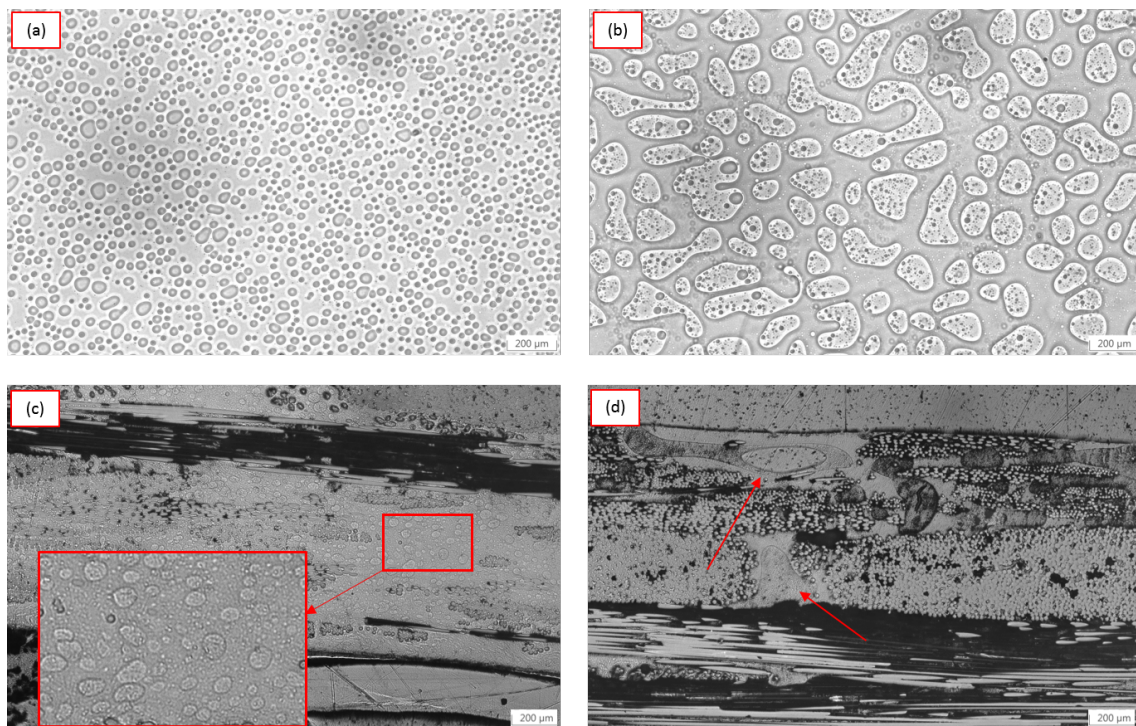


Figure 4.7: Microscopy images (a) UP – 4 wt% PCL without fibres, (b) UP-7 wt% PCL without fibres, (c) UP - 4 wt% PCL with fibres, (d) UP - 7 wt% PCL with fibres.

Effect of graphene on fibres impregnation and phase separation

The presence of a large quantity of graphene in the resin increases the viscosity of the system and could influence the impregnation of the fibre tows. To study this effect, plates with 8 wt% of graphene were produced following the optimized cycle discussed above. An optical microscopy of the polished sample is shown in Figure 4.8.a. Firstly, the impregnation of the fibre tows was not affected by the presence of graphene, only few voids being observed in the fibre tows. Secondly, no filtering effect was observed throughout the sample. The graphene forming a continuous path between the fibre tows with only few graphene particles entering the fibre tow. This behaviour was attributed from the non-crimp complex fibre architecture that leaves large channel for the graphene to migrate through the fibre preform. The same test was performed on the weave fibre architecture and is shown Figure 4.8.b. In this case, the graphene particles were completely filtered and left at the surface of the preform. No graphene particles were observed inside the cured preform. There is then a critical distance between the fibre tows to avoid any filtration of particles. A quick image analysis of each system shows an average distance between the tows of $\sim 53 \mu\text{m}$ and $126 \mu\text{m}$ for the weave and complex fibre architecture, respectively. The average agglomerate size of the graphene powder being close to $30 \mu\text{m}$, the distance between the tows for the weave architecture is then too small for the particles to flow freely in the preform. An educated guess would be to have at least three times the average particles size to avoid any filtration effects. In this case, a distance of at least $\sim 90 \mu\text{m}$ between the fibre tows would then be necessary to obtain a homogeneous distribution of the graphene through the plate.

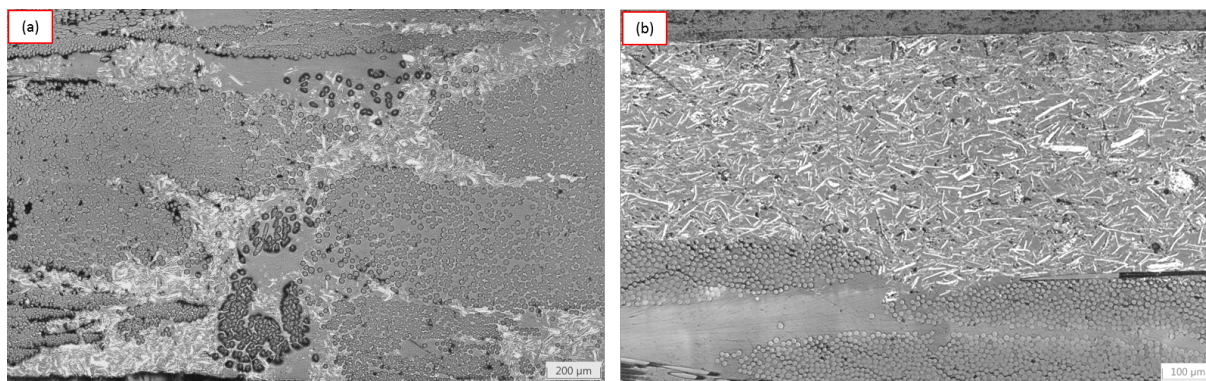


Figure 4.8: Microscopy images (a) UP–8 wt% gf with the complex fibre architecture (b) UP–8 wt% gf with the weave fibre architecture.

Figure 4.9 shows a microscopy of a plate with 4 wt% of PCL and 8 wt% of graphene. When added to a phase separating system, the graphene will stay in the UP-rich region, leaving the PCL-rich phase totally free of graphene particles. That creates a self-assembly network of graphene rich phase in the matrix. This network could have a positive impact on the fraction of graphene needed to reach the percolation threshold. The phase separated morphology is similar to what was observed in Figure 4.7c, the addition of graphene has then no substantial effect on the dynamic of phase separation.

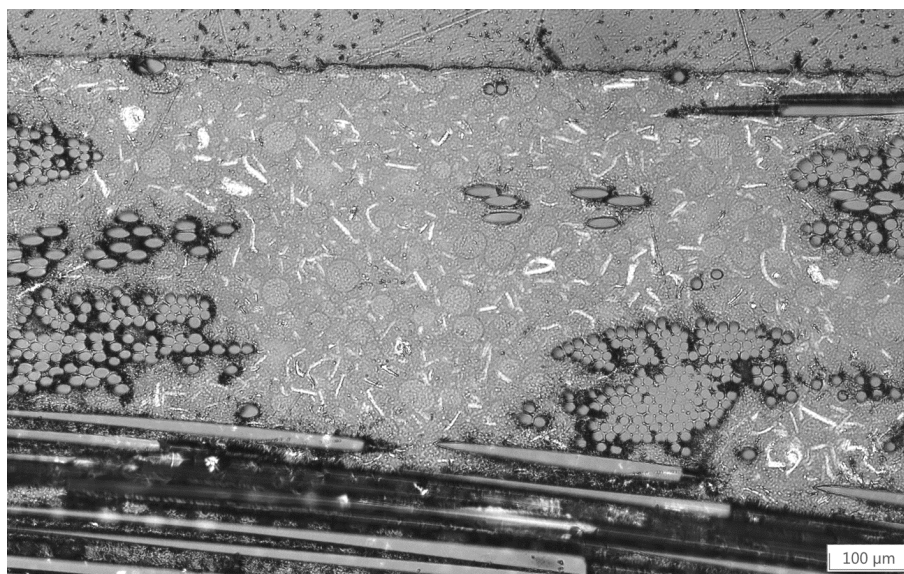


Figure 4.9: Microscopy image of UP – 4 wt% PCL and 8 wt% gf.

4.4. Conclusion

The impact of the processing parameters on the impregnation of the fibre preform was studied with unsaturated polyester and a complex fibre architecture. The use of an open mould was found to leave the applied pressure too low to have a good impregnation of the fibre bed. A partial solution was to use a metallic shim in order to trap the resin in the mould and increase the effective pressure on the resin. When the resulting part showed some improvements, the quick cure of the resin was the factor limiting for a good impregnation of the fibre tows. A simple tow impregnation model showed that a pressure of 12MPa would infiltrate the fibre tows in a couple seconds. To reach such pressure, the target pressure when setting the zero thickness of the mould was increased to 12MPa. The resulting plates were of required quality, fully impregnated with only a few residual voids. The optimized moulding cycle was tested on phase separating blends and showed no effect on the morphology of phase separation. The obtained morphology being similar to what was observed at low pressure and without fibres. The addition of large quantity of graphene particles to the complex fibre preform showed no filtration effect and resulted on a homogeneous distribution of the particles in between the fibre tows. The same test was conducted on a denser twill weave showing a full filtration of the graphene particles at the surface of the sample. The distance between the fibre tows being too close to the average graphene agglomerates size. The addition of graphene in a blend of unsaturated polyester and polycaprolactone showed a selective localisation of the graphene in the UP-rich phase leaving the PCL-rich phase totally free of graphene particles. Such composition then creates a self-assembly network of graphene-rich phase reducing the quantity of graphene needed to reach the percolation threshold for electrical conduction. The optimized

processing parameters then allows for the production of fully impregnated multiscale multiphase graphene-based composite with promising properties self-sensing properties.

Acknowledgements

The authors would like to thank their funding partners, The Werner Graupe Fellowship, the Natural Sciences and Engineering Research Council of Canada (NSERC) grant RDCPJ 530253-18, Prima Quebec grant R16-46-005, NanoXplore Inc., the Research Center for High Performance Polymer and Composite Systems (CREPEC) and the McGill Engineering Doctoral Awards program (MEDA) for their support.

References

- [1] Hu Liu, Qianming Li, Shuaidi Zhang, Rui Yin, Xianhu Liu, Yuxin He, Kun Dai, Chongxin Shan, Jiang Guo, Chuntai Liu, Changyu Shen, Xiaojing Wang, Ning Wang, Zicheng Wang, Renbo Wei, and Zhanhu Guo. Electrically conductive polymer composites for smart flexible strain sensors: a critical review. *Journal of Materials Chemistry C*, 6(45):12121–12141, 2018.
- [2] Simon Baril-gosselin. Investigation of the resin film infusion process for multi-scale composites based on the study of resin flow , void formation and carbon nanotube distribution. 2018.
- [3] Yuwei Zhang, Yucai Shen, Kunxiang Shi, Tingwei Wang, and Eileen Harkin-Jones. Constructing a filler network for thermal conductivity enhancement in epoxy composites via reaction-induced phase separation. *Composites Part A: Applied Science and Manufacturing*, 110(January):62–69, 2018.
- [4] Ihor Sahalianov and Olexandra Lazarenko. Enhancement of electroconductivity and percolation threshold by the morphology of dielectric network in segregated polymer/nanocarbon composites. *Materials Research Express*, 6(9), 2019.
- [5] Roberto J.J. Williams, Boris A. Rozenberg, and Jean Pierre Pascault. Reaction-Induced Phase Separation in Modified Thermosetting Polymers. *Advances in Polymer Science*, 128:95–156, 1997.
- [6] NanoXplore Inc. Technical Data Sheet - GrapheneBlack3X DS-GB3X-210803. 2021.
- [7] Alberto Bianco, Hui Ming Cheng, Toshiaki Enoki, Yury Gogotsi, Robert H. Hurt, Nikhil Koratkar, Takashi Kyotani, Marc Monthieux, Chong Rae Park, Juan M.D. Tascon, and Jin Zhang. All in the graphene family - A recommended nomenclature for two-dimensional carbon materials. *Carbon*, 65:1–6, 2013.

- [8] Peter Wick, Anna E. Louw-Gaume, Melanie Kucki, Harald F. Krug, Kostas Kostarelos, Bengt Fadeel, Kenneth A. Dawson, Anna Salvati, Ester Vázquez, Laura Ballerini, Mauro Tretiach, Fabio Benfenati, Emmanuel Flahaut, Laury Gauthier, Maurizio Prato, and Alberto Bianco. Classification framework for graphene-based materials. *Angewandte Chemie - International Edition*, 53(30):7714–7718, 2014.
- [9] Benoit Landry. Experimental Study and Numerical Simulation of Defect Formation During Compression Moulding of Discontinuous Long Fibre Carbon/PEEK Composites. page 174, 2015.
- [10] T. Centea and P. Hubert. Modelling the effect of material properties and process parameters on tow impregnation in out-of-autoclave prepregs. *Composites Part A: Applied Science and Manufacturing*, 43(9):1505–1513, 2012.
- [11] B. R. Gebart. Permeability of Unidirectional Reinforcements for RTM. *Journal of Composite Materials*, 26(8):1100–1133, 1992.

PREFACE – CHAPTER 5

The following chapter study how the electron flow is affected by the multiscale and multiphase nature of the system. Firstly the DC conductivity evolution with the amount of graphene and thermoplastic is studied in the transfers and longitudinal direction. A behavioural model is developed to understand the coupled effect of graphene and phase-separated morphology on the observed percolation threshold and conductivity. To further understand the influence of such microstructure on the electron flow, the AC conductivity was investigated and compared to the "universal dielectric response". Finally, the sensing capabilities of these materials were studied in compression, where the piezoresistive nature of the system is highlighted.

CHAPTER 5

Electrical characterization and sensing capabilities of self-assembly multi-scale multi-phase graphene-based composites.

N. Hostettler, P. Hubert, Carbon (2023).

DOI: <https://doi.org/10.1016/j.carbon.2023.03.005>

Keywords: Graphene composite; Self-assembly; Multi-phase; Electrical characterization; Strain Sensing

Abstract

The addition of graphene particles to a thermoset resin strongly enhances its electrical properties, opening the use of such system for damage and strain tracking. This increase is, however, proportional to the amount and purity of the graphene particles, usually at high costs. Using a high amount of filler leads to a decrease in processability as well as a possible drop in mechanical properties. In order to reduce the quantity needed for conduction with few-layer graphene (FLG), a self-assembly network of graphene particles in the polymeric structure was created using blends of unsaturated polyester and polycaprolactone, using FLG and fibreglass reinforcement. The DC and AC electrical conductivities were strongly enhanced by the coupled effect of phase separation and fibre preform, effectively reducing the percolation threshold. An impressive shift was measured from 8.2 wt% of graphene for the neat resin to 1.4 wt% of graphene for the optimized composition. These materials also showed strong strain sensing capabilities at low applied

voltage. Therefore, these systems are reliable and cost effective candidates for self-sensing and damage tracking application.

5.1. Introduction

The addition of carbon based particles, and more specifically graphene, to a thermoset resin is known to greatly increase its electrical properties. Research has shown different magnitudes of increase in conductivity depending on the media and purity of the filler. For example, a four order of magnitude increase with 12 wt% of graphene nanoplatelet [1] or seven order of magnitude with 0.2 wt% of higher quality graphene [2], and many others in between [3–7]. The use of graphene filler offers a greater flexibility in comparison to metallic particles mainly because of its lower mass, allowing to process light conductive structures. Other advantages of using graphene particles instead of other carbon-based filler include safer handling [8] compared to nano-carbon black, and ease to disperse and process compared to carbon nanotube (CNTs). As a results of the aforementioned advantages of graphene-based composite, significant interest has been generated in its potential uses. Such uses included actuators, fuel cells, photo-detectors or mechanical sensors [9]. The latter is of particular interest since it would allow a direct tracking of the strain and damages during a part's life. Several papers were published in this scope [2, 10–13] showing encouraging results. However, it typically uses either monolayer chemical vapor deposition (CVD) graphene or advanced processing method to process a real size part (fibre coating, filament winding, etc...). The alternative few-layer graphene is required in larger amounts to reach the conductivity threshold. Prior research has shown that by blending the thermoset resin with a thermoplastic, it was possible to create a

self-assembly network of nanoparticles, lowering the quantity of particles needed for conduction (the percolation threshold) [14–16]. It would then be possible to produce cost-effective self-sensing composite materials that would reduce the maintenance costs and increase the intrinsic conditions of a part in service. In a previous work, the morphology and mechanical properties of several phase-separating unsaturated polyester (UP)/polycaprolactone (PCL) blends were studied with different quantity of graphene filler showing strong increases in toughness [17]. The objectives of this paper is to study the AC and DC electrical properties of unsaturated polyester glass fibre composites with different quantities of graphene and polycaprolactone, and access their sensing capabilities in compression.

5.2. Materials and Methods

5.2.1. Materials

The resin system was the PolyLite 31289 from *Reichhold*, a pre-accelerated unsaturated polyester (UP) cured with 2 wt% of Norox Azox from *United-initiator*. It was blended with varying quantities (0 – 8 wt%) of CAPA6500 a polycaprolactone (PCL) from *Ingevity* to achieve different morphologies of phase separation, and between 0 and 10 wt% of graphene powder. The graphene was the GrapheneBlack 3X from *NanoXplore inc.*, an industrial grade graphene with a primary particle size between 1–2 μm and an agglomerate size of $D_{50} = 38 \mu\text{m}$, 6 to 10 graphene layers in thickness, a carbon to oxygen ratio of 96:1 and a bulk density of 0.2 – 0.3 g/cm^3 [18]. According to the classification framework for graphene-based materials proposed by Bianco *et al.* [19], Wick *et al.* [20] and the ISO/TS 21356-1:2021, this material should be referred to as

few-layer graphene (FLG) nanoplatelets. For simplicity, it will be referred to as "graphene" or "gf" for the rest of this paper. To achieve a higher degree of dispersion, 1 wt% of Triton X100 diluted 15:1 in styrene to reduce its viscosity, both from *SigmaAldrich*, was used as a surfactant. Finally, the resin was reinforced with a bidirectional-E glass-complex 0/90/Mat preform from *SAERTEX* with a superficial density of 910 g/m².

5.2.2. Methods

Blend and Plate Processing

The unsaturated polyester resin was weighted into a glass jar, the formulations to contain graphene were transferred into a glove box where the target amount of graphene was incorporated. The surfactant was added and the mixture was dispersed at room temperature with a probe sonicator (*Hielscher UP400St*) for two cycles of 7 min spaced by a 15 min cool down step to limit the temperature increase below 70°C. The jar was then transferred into a 65°C pre-heated water bath where the desired quantity of PCL pellets was added and mechanically stirred for 20 min at 1500 rpm until fully dissolved. Once homogeneous, the system was let to rest at room temperature for 20 min to cool down and stabilize the phase-separated morphology. The initiator was incorporated in the system before degassing for 1–2 min for the resin to be ready for processing.

The processing of the plates was conducted by compression resin transfer moulding on a MTS 250 kN press with a 100x100 mm² open square mould. Beforehand, the surface of the mould was cleaned with isopropanol and coated with a mould release agent, Chemlease 2752W from *ChemTrend*, to ease the demoulding. The compression sequence

was as follows: (i) the empty mould was closed to set the zero distance and opened back to the starting position; (ii) Teflon tape was applied on the junction at the bottom of the mould to reduce resin leakage; (iii) two layers of E-glass preform were set in the mould [Mat/90/0]_s (target thickness of $t = 1.8$ mm and $V_f = 0.4$), topped by a 3.8 mm thick metallic shim frame (outer and inner size of 100 and 80 mm respectively) to create a pinching zone at the extremity of the mould; (iv) the resin was poured directly on top of the fibres and compressed at 0.05 mm/s (last 10 mm) to the target thickness. Next, the mould was kept at room temperature for 15 min to impregnate the fibre preform, from which the temperature was increased to 50°C for an additional 10 min to cure the system. The plate was then demoulded and post-cured in an oven at 120°C for 2 h to complete the cure.

DC – Electrical Characterization

Two types of DC electrical characterizations were conducted on the plates: one through their thickness, or transverse (perpendicular to the fibres) and one along their length, or longitudinal (parallel to the fibres). The transverse measurements were conducted on 70 x 70 mm² square plates on a *Keithley* - Resistivity Test Fixture Model 8009 powered by a *Keithley* - Electrometer Model 6517A following ASTM D-257. The current, I , was acquired on a LabView code and its value was taken as the average of the last 15 s of the stabilized signal. The corresponding average volumetric resistivity was calculated as:

$$\rho_V = \frac{22.9V}{It} = \frac{22.9}{t}R = \frac{1}{\sigma_V} \quad (5.1)$$

where ρ_V is the volumetric resistivity, t [cm] the thickness of the sample, V the applied

voltage, I the current reading, R the resistance and σ_V the conductivity. The applied voltage was adapted from 100 V for samples below the percolation threshold to 2 V for the samples above it.

The longitudinal resistivity measurements were conducted on rectangular 20 x 70 mm² samples with a *Keithley 6517A*, the voltage was directly applied on each side of the sample. To ensure good contact, 3 mm wide silver paint electrode (*SPI-supplies*) were painted on each end of the sample. The resistivity was then calculated as:

$$\rho_V = \frac{RA}{l} = \frac{1}{\sigma_V} \quad (5.2)$$

where $A = t \cdot w$ is the cross section of the sample, and l its effective length corrected for the width of the silver electrodes. The same voltages were used as the transverse measurement. The current-voltage behaviour was analyzed by varying the voltage from 0.5 to 100 V depending on the samples. All measurements were done at room temperature.

AC – Electrical Characterization

A frequency sweep was performed longitudinally applying a sinusoidal current (1 mA above and 100 μ A below the percolation threshold) with a *Keithley 6221 AC/DC* current source at a max voltage compliance of 95 V. The frequency of the signal was varied each 15 s by a LabView code from 10² to 10⁶ Hz. The applied voltage was measured on a *Keithley 2701* multimeter on another LabView instance. The AC conductivity was calculated as:

$$\sigma_{AC} = \frac{Il}{VA} = \frac{1}{Z} \frac{l}{A} = Y \frac{l}{A} \quad (5.3)$$

where I is the current amplitude, l the length of the sample corrected for the length of

the silver electrode, V is the measured voltage, A is the cross section, Z is the impedance and Y the admittance. All measurements were done at room temperature.

Piezoresistive Behaviour - Gauge Factor

The evolution of the resistance with an applied strain was studied longitudinally with the DC setup described above and a 2 V electrical potential. The samples were placed between two steel blocks electrically isolated with Teflon tape mounted in a MTS 100 kN. A pre-charge of 0.2 kN was applied to stabilize the system and a strain of $\varepsilon = 0.05$ was applied for six cycles at 0.01 mm/s and 15 s waiting time between each cycles. The changes in resistance and the applied strain are used to calculate the gauge factor (GF) as follows:

$$GF = \frac{\Delta R}{R_0 \varepsilon} \quad (5.4)$$

where $\Delta R = R - R_0$ is the instantaneous change in resistance, R_0 is the initial resistance and ε the real applied strain measured from the displacement data. Note that the first cycle was discarded from the average as its change in resistance is usually highly asymmetric and non-representative of the actual behaviour.

5.3. Results and Discussion

5.3.1. Phase-separation morphology with fibres and graphene

The morphologies and mechanical properties obtained with UP/PCL phase-separating systems without fibres were described in detail in a previous study [17]. The morphologies of a selection of samples with fibres are displayed in Figure 5.1. In all cases, no filtering of graphene was observed. This phenomenon can be seen when the space in between the

fibre tows is too small for the graphene to flow with the resin, leading to a heterogeneous distribution of particles through the thickness of the plate. It is not observed here due to the complex fibre architecture of the preform that leaves large channels for the particles to flow in between the fibre tows. The graphene was found to stay in these channels with only few particles observed in the tows (see Figure 5.1.a). When processing a blend of UP and PCL, the fibre tows were found to be largely surrounded by UP-rich regions, the PCL-rich phase showing no wetting of the fibres (see Figure 5.1.b). Some occurrences of PCL-rich phases were, however, still found in the fibre tows showing that no local changes in compositions, which could affect the local morphologies, were happening. The phase separation morphologies are therefore not affected by the presence of fibres and are similar to what was found in the systems without fibres [17]. Processing a system with both graphene and PCL creates a self-assembly network of particles that are preferably located in the UP-rich phase (see Figure 5.1.c). The coupling effect of this graphene-rich and -poor regions on the electrical properties was studied in what follows.

5.3.2. DC electrical characterization

Effect of graphene and PCL on the electrical conductivity

The evolution of the electrical conductivity as a function of the quantity of PCL and graphene is shown in Figure 5.2. The transverse behaviour is displayed in Figure 5.2.a, up to a fraction of 2 wt% of graphene only little effects were observed on the conductivities which stay in the insulating range between 10^{-17} and 10^{-13} S/cm. The graphene particles being too far from each other to allow an electron flow by tunnelling. As the quantity of graphene was increased, a characteristic large change in conductivity was observed with a

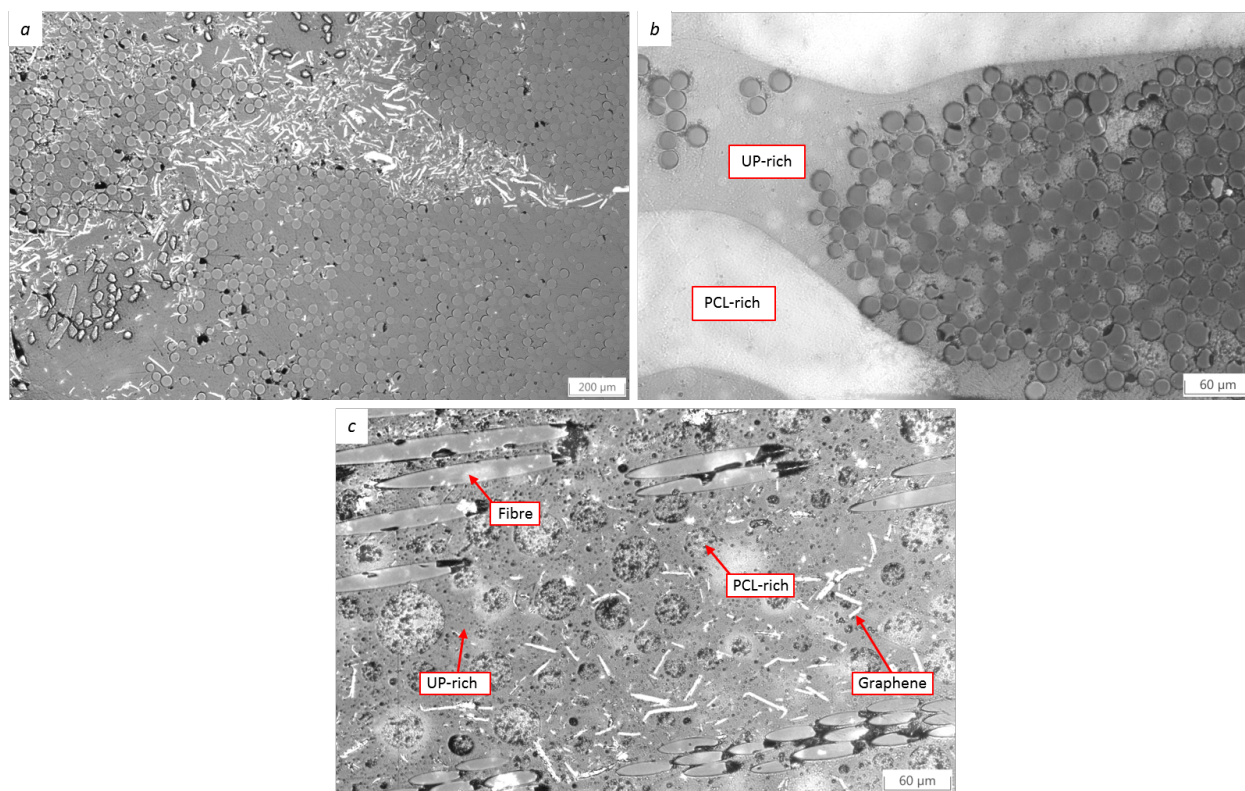


Figure 5.1: Optical microscopy of polished samples: (a) UP 8 wt% graphene (b) UP 8 wt% PCL and (c) UP 6 wt% graphene and 4 wt% PCL. (A high-resolution version of these images for use with the Virtual Microscope is available as eSlide: (a) VM06778 (b) VM06779 (c) VM06781)

jump of more than eight orders of magnitude to reach a plateau at around 10^{-5} S/cm with 4–6 wt% of graphene (threshold of conductivity). The conductivity in this range is usually dominated by tunnelling with only few electrons flowing through direct contact between graphene particles. The conduction by direct contact increases with the graphene content until reaching a plateau where most of the electrons flow directly between the graphene particles. This is observed in Figure 5.2, where the conductivity only marginally increases at larger quantity of graphene. An equivalent behaviour was observed with the longitudinal characterization (see Figure 5.2.b). In this case, however, the conductivity appears to be numerous order of magnitude higher throughout the all range of compositions with a maximum at ~ 0.03 S/cm with 8 wt% of graphene and 2 wt% of

PCL. These conductivity values correlate to those found in similar studies relating to graphene based composites [21]. The difference in magnitude between the transverse and longitudinal conductivity was observed in previous research [1], where it was attributed to the filtering of graphene resulting from the hand-layup processing. In the current study, no filtering of the graphene was observed. To better understand this phenomena, a validation of the transverse conductivity measurement was conducted using the same method as the one used for the longitudinal characterization. The measured conductivities were of the same order of magnitude as the ones measured with the 8009 test fixture, the difference was therefore unrelated to the measurement apparatus. It was assessed that the lower conductivity in the transverse direction was related to the orientation of the fibre preform, perpendicular to the current flow reducing the possible number of electron paths. For this assumption to be validated, the transverse percolation threshold would be slightly lower than the longitudinal, the presence of glassfibre creating a network of graphene-rich regions in between the tows (see Figure 5.1.a). To further investigate this assumption, the percolation threshold was determined by fitting a sigmoidal-Boltzmann model to the experimental data as described in [22–24]:

$$\sigma = \sigma_2 + \frac{\sigma_1 - \sigma_2}{1 + \exp\left[\frac{\phi - \phi_c}{\Delta\sigma}\right]} \quad (5.5)$$

where σ is the conductivity of the composite, σ_1 and σ_2 are fitting parameters corresponding to the minimal and maximal conductivity of the composite, ϕ is the quantity of filler, $\Delta\sigma$ the slope at the inflection point and ϕ_c percolation threshold. The obtained fit is shown in Figure 5.3 with experimental data and the double derivative of the conductivity used to determine the percolation threshold. The detailed values of ϕ_c for

each fraction of PCL are displayed in Table 5.1. Note that a sigmoidal model was preferred to the more common power law: $\sigma \propto (\phi - \phi_c)^t$ used in most studies [21] since it was found more precise fitting over a full range of data. Indeed, using the usual definition, changes of more than 1 wt% were observed for ϕ_c depending on the data included in the fitting procedure with an $R^2 > 0.98$. This ambiguity was removed using the sigmoidal-Boltzmann model. The percolation thresholds obtained in the transverse direction were always lower than the longitudinal, due to the fibres concentrating the graphene in the inter-tow region. This also reduces the number of electron paths, leading to a reduction of the global conductivity compared to the longitudinal. This is even more evident when comparing the values of ϕ_c obtained for the same system without fibre with a percolation threshold at 8.20 wt% [17] compared to 2.28 wt% of graphene with the fibres. This difference being larger than the one expected from the volume fraction of fibre ($V_f = 0.4$), few graphene particles should be found within the fibre tows (this is illustrated in Figure 5.1.a).

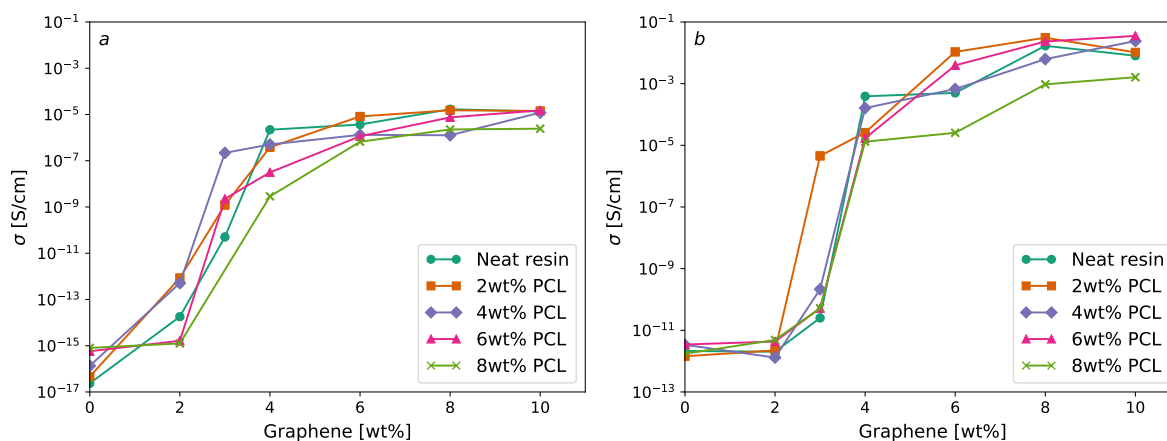


Figure 5.2: (a) Transverse and (b) longitudinal DC electrical conductivity.

As the addition of PCL creates a self-assembly network of graphene in the resin, it is reducing the percolation threshold of the system [17]. The largest shift of the percolation

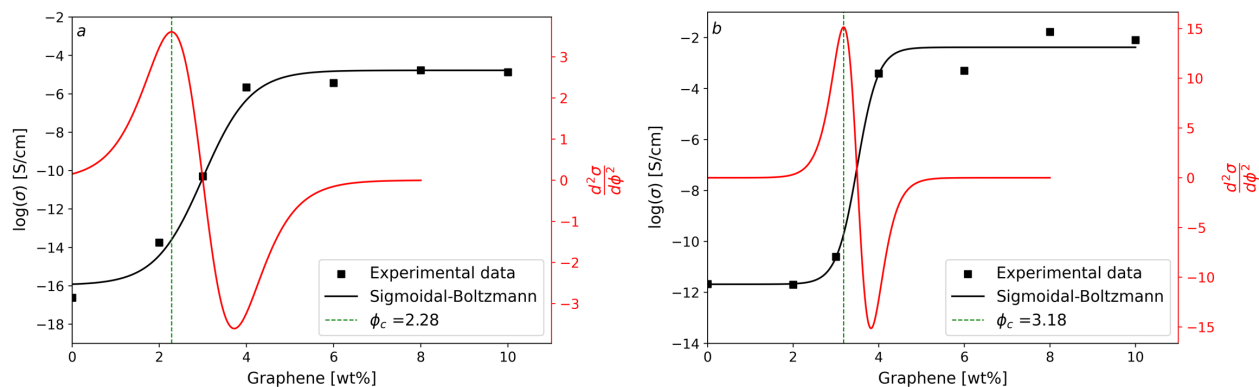


Figure 5.3: Fitted DC electrical conductivity and its second derivative for a sample without PCL measured in the (a) transverse and (b) longitudinal direction.

threshold was observed at 2 wt% of PCL with a difference of $\sim 38\%$ and 31% in the transverse and longitudinal direction compared to the system without PCL. Interestingly, the composition at 4 wt% of PCL performed better than the latter in the transverse but worst on the longitudinal direction. This difference is attributed to the size of the morphologies. The compositions at 2 wt% of PCL were composed on a very fine dispersion of PCL-rich particles (see Figure 5.4.a). These particles are also found in other compositions with larger PCL content accompanied with coarser particles, as is the case for the samples with 4 wt% of PCL. These larger particles were found to be unstable in inter-tow regions, leaving them mostly located in the space in-between fibre layers (see Figure 5.4.b). As they are numerous and about the same size as the graphene particles, they do not create an effective interconnected path of graphene, the effective interparticle pathway being small (see Figure 5.5.b). As these resin rich regions are mostly located along the longitudinal direction, this reduces the observed shift in percolation threshold. On the transverse direction however, the path is mostly filled with fine particles, thus the shift in percolation threshold is more effective. The same effect is observed with compositions containing a larger amount of PCL only with larger PCL-rich region (see Figure 5.5). Note that these system then have

a double percolation threshold, one from the graphene and another one arising from the phase separation morphology.

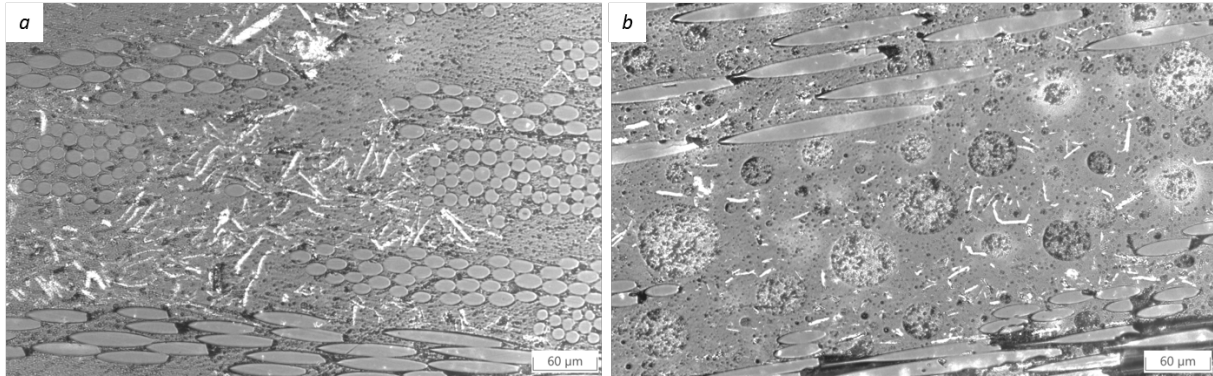


Figure 5.4: Optical microscopy images: (a) UP 6 wt% graphene and 2 wt% PCL - the fine darker dots are the PCL-rich phase and the lighter round are the glassfibres [17], (b) UP 6 wt% graphene and 4 wt% PCL. (A high-resolution version of these images for use with the Virtual Microscope is available as eSlide: (a) VM06782 (b) VM06783)

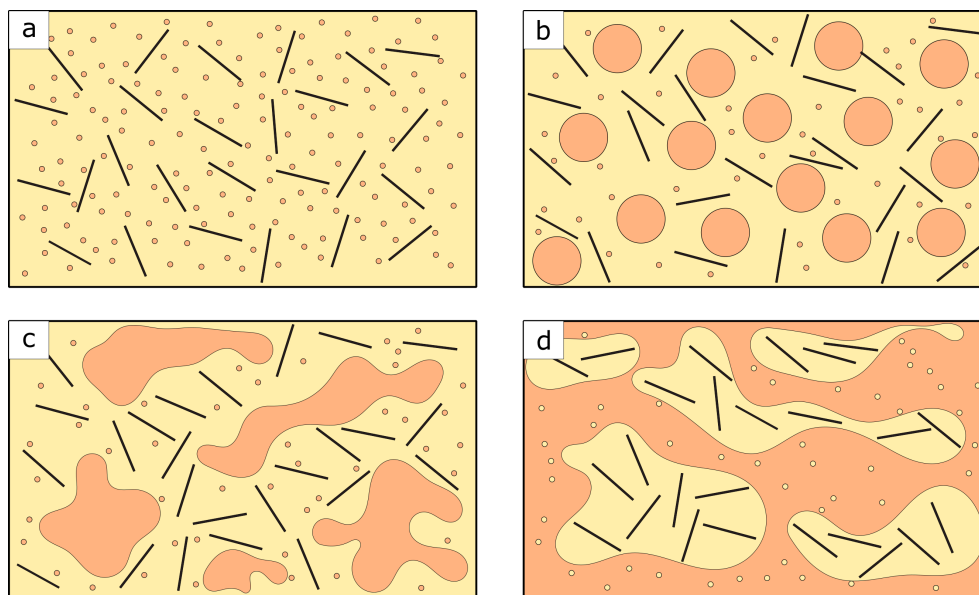


Figure 5.5: Schematic of the phase separated microstructure of UP blends with (a) 2 wt% (b) 4 wt% (c) 6 wt% and (d) 8 wt% of PCL. The PCL-rich phase is orange, the UP-rich phase yellow and the graphene black.

Table 5.1: Transverse and longitudinal percolation threshold as a function of the PCL content.

PCL [wt%]	ϕ_c^{Trans}	ϕ_c^{Long}
0	2.28	3.18
2	1.4	2.21
4	1.39	3.06
6	2.27	2.96
8	2.07	3.08

Voltage – Current dependency

The evolution of longitudinal conductivity with applied voltage for the neat resin with increasing quantity of graphene is shown in Figure 5.6.a. Linear regressions were added to each data family along with coefficient of determinations (R^2) to help assess the linearity of the behaviour. For these compositions above the percolation threshold, the linear behaviour of the current with voltage is characteristic of an ohmic material, the constant slope being the resistivity. The value of R^2 also converges to unity while increasing the quantity of graphene, which shows there has been creation of more electron path and that the material is behaving as a homogeneous resistor. Such linearity of the I-V behaviour is a sign that electron flow is carried by "direct contact" between graphene particles. In reality, however, there are still polymer molecules surrounding the graphene particles. This is possible as the layer is thin enough, and the barrier potential is low enough, to allow the direct flow of electrons [3, 25, 26]. At compositions near the percolation threshold, electron flow is mainly occurring via tunnelling that has a characteristic non-linear I-V behaviour [3]. This can be observed on Figure 5.6.b (I_0 is the current measured at 0.5 V). In this case, two samples at 3 wt% gf with 2 and 4 wt% PCL were tested. The first composition was above the percolation threshold ($\phi_c^{2wt\%PCL} = 2.21$) and

has an ohmic behaviour indicating a conduction mostly happening via "direct contact". The composition at 3 wt% gf - 4 wt% PCL was slightly under the percolation threshold ($\phi_c^{4wt\%PCL} = 3.06$), and depicted a clear non-linear I-V behaviour sign that electrons flow was mainly occurring via tunnelling. These observations are in line with the definition of the percolation threshold, as the first occurrence of a direct electron path through the material. The effects of PCL on the conduction mechanism are shown in Figure 5.6.c, where samples with 6 wt% of graphene were tested with varying quantity of PCL. As discussed above, in relation to the percolation threshold, a fine dispersion of PCL helps in reducing the distance between graphene particles. This was not observed for compositions with 8 wt% of PCL, where the quantity of thermoplastic is over the critical point for phase inversion creating isolated graphene-rich regions [17] (see Figure 5.5.d). In such a case, the main phase was the PCL-rich phase blocking the creation of a self-assembly network of graphene and increasing the distance between particles leading to a reduction in the linearity of the I-V behaviour.

5.3.3. AC electrical characterization

The frequency sweep of σ_{AC} for neat UP with increasing quantity of graphene, and for blends of UP – 8 wt% gf with increasing quantity of PCL, are shown in Figure 5.7. A typical "universal dielectric response" is observed in both cases where σ_{AC} can be written as a power law [27, 28]:

$$\sigma_{AC}(\omega) = \sigma_0 + A\omega^n \quad (5.6)$$

with $\omega = 2\pi f$ the angular frequency and f the frequency of the AC current, σ_0 the

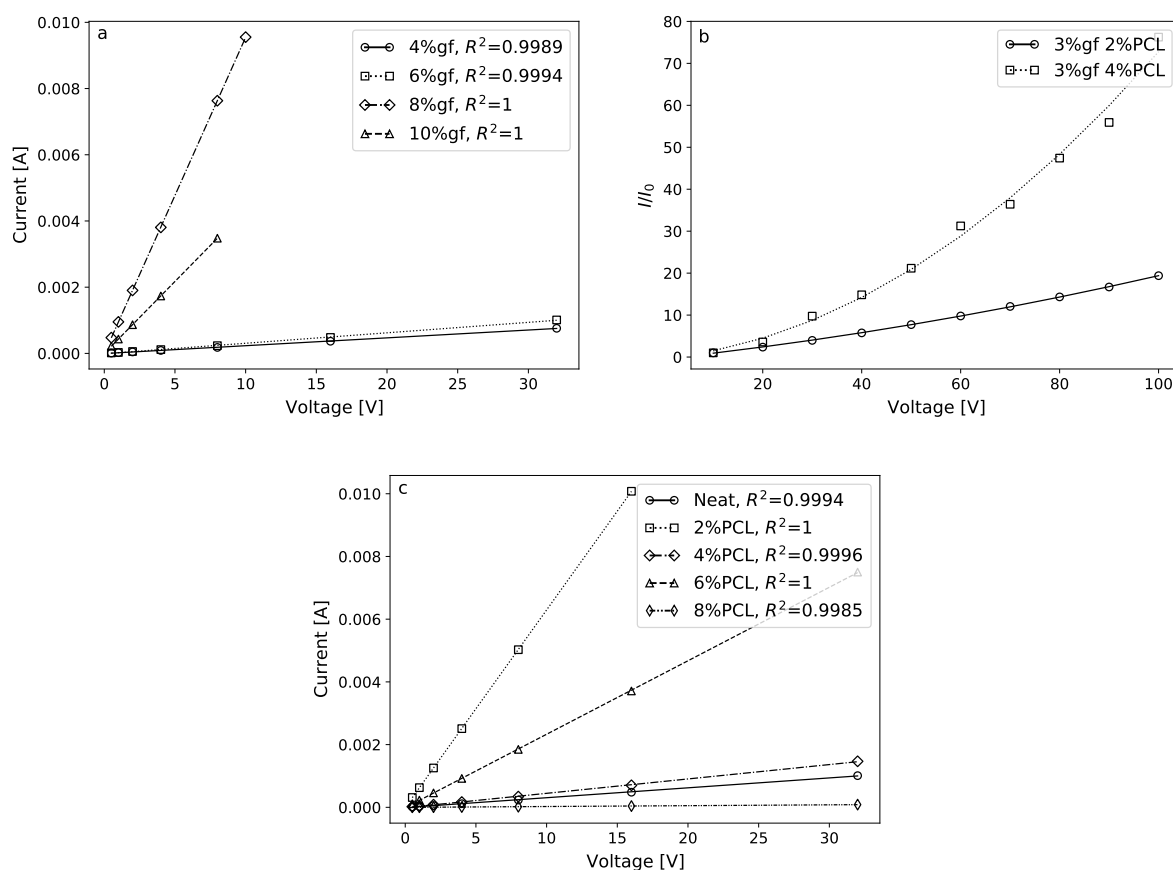


Figure 5.6: Evolution of the measured current as a function of the applied voltage: (a) neat UP with increasing quantity of graphene. (b) Blend of UP – 3 wt% gf with 2 and 4 wt% PCL slightly above and below the percolation threshold, respectively. (c) UP – 6 wt% gf with increasing quantity of PCL.

conductivity at low frequencies, A a constant and n the conductivity exponent. According to this representation, at low frequencies ($\sigma_0 \gg A\omega^n$), σ_{AC} is frequency independent and converges to σ_0 equal to the DC electrical conductivity. This is in agreement with what was observed in Figure 5.7.a in relation to compositions above the percolation threshold ($\phi > 2.28$) and with a frequency independent region at $\sigma_0 = \sigma_{DC}$ up to a threshold frequency ω_0 . This behaviour is characteristic of a non-dielectric material [29]. Visualizing the resin-graphene system as a series of resistors (graphene) surrounded by an insulating capacitor (resin), the current preferentially flows through the resistors in such regime [28]. At compositions below the percolation threshold, σ_{AC} is frequency dependent over the all range of frequencies with a slope close to unity, which is in agreement with the dielectric conductivity response to an AC current $\sigma_{AC} = \omega\varepsilon''\varepsilon_0$, with ε'' the imaginary part of the dielectric constant and ε_0 the vacuum permittivity [29, 30]. Note that in this work, the conductivity at lower frequency does not converge to σ_{DC} and was measured at several orders of magnitude higher. When small differences were observed in other research, they were usually attributed to regions of network where AC transport was preferential to DC conduction throughout the whole network, avoiding large energy barriers. However, σ_0 was still within one order of magnitude of σ_{DC} [29, 31, 32]. As all these systems were only composed of polymer and conductive filler without fibreglass, the reinforcement is thought to be the source of the larger σ_{AC} measured at low frequencies for samples below the percolation threshold. To verify this assumption, a sample of pure neat resin was tested without fibres to assess if $\sigma_0 = \sigma_{DC}$ at low frequencies and for composition below the percolation threshold. AC transport could then be helped by the presence of fibres the electron hopping at the resin-fibre interface. The tests showed two

orders of magnitude between a sample with and without fibres, only partially justifying the observed difference. The difficulty to have precise measurements on samples with such high resistivity is a possible reason for this difference; as this range of conductivity is not the one of interest, no further tests were conducted to explain in depth this discrepancy. For compositions higher than the percolation threshold, Equation 5.6 predicts a frequency dependent regime at frequencies larger than ω_0 with a conductivity exponent $0 < n < 1$. This is observed for compositions with 4 wt% and 6 wt% of graphene with a conductivity exponent $n = 0.92$ in both cases. It was shown that conductivity exponent in the range $0.8 < n < 1$ is characteristic of conduction carrying via electron hopping mechanisms in a disordered material of randomly varying energy barrier [29], which is a good representation of graphene particles separated by resin layers of varying thicknesses. In such regime, current flows through both the resistors and capacitors. The samples with larger fraction of graphene did not show frequency dependent conductivities at the tested frequencies. A similar behaviour would most likely be observed if the testing apparatus could reach higher frequencies (GHz) [33]. The effect of the phase separated morphology on the AC conductivity is shown in Figure 5.7.b, where blends of UP – 8 wt% gf with varying quantities of PCL were tested. As previously observed for the DC conductivity, the dispersion and size of the PCL-rich phase is significant. Once again, the composition with 2 wt% PCL had the highest measured conductivity with a morphology composed of a thin dispersion of PCL-rich particles (see Figure 5.1.a). At 4 wt%, the size of the PCL-rich phase was on the order of magnitude of the graphene sheets, reducing the shift in percolation threshold observed at 2 wt% PCL. At 6 wt% PCL a less dispersed larger regions of PCL-rich phase help getting the graphene sheet closer leading to a higher

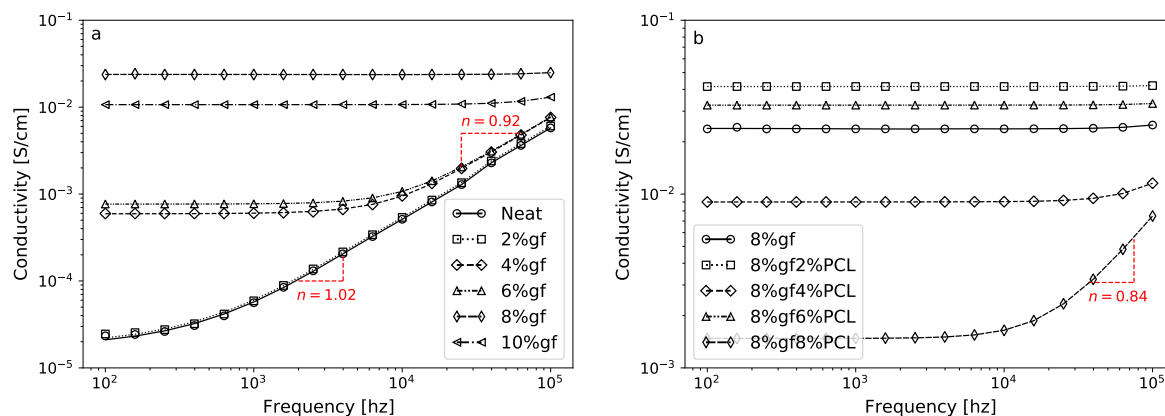


Figure 5.7: AC frequency sweep: (a) neat UP with increasing quantity of graphene. (b) blend of UP-8 wt%gf with increasing quantity of PCL.

conductivity. Interestingly, the effect observed on the 8 wt% PCL, with a PCL-rich dominating phase pulling graphene sheets away from each other leading to a non-linear current-voltage behaviour (see Figure 5.5.d), is even more apparent with an AC current. It was indeed the only composition with 8 wt% of graphene that showed a frequency dependent region, an indicator of a much lower electrical conductivity. The conductivity exponent ($n = 0.84$) was also lower compared to those measured for samples without or with lower quantity of PCL, illustrating a longer random walk throughout the network for the charge carrier and reduced number of electron paths [29].

5.3.4. Sensing and gauge factors

Cyclic compression sensing tests were performed on the samples used for the longitudinal electrical characterization with 6 wt% gf and above. The group with lower quantities of graphene was not explored further due to a conductivity signal dominated by the background noise making them less reliable to measure. The characteristic evolution of deformation, force, and resistivity for a sample of UP – 6 wt% gf 2 wt% PCL is displayed in Figure 5.8.a. The resistivity of the sample evolves with the applied deformation, the

compression pushing the graphene particles closer to each other creating new electron paths leading to a drop in resistivity [2]. Interestingly, the resistivity signal is extremely close to the measured force; with the relaxation peaks post-compression clearly visible on the resistivity measurements. Note that the maximal applied force for every sample was ~ 0.9 kN, with sensing capabilities being measured at much lower forces, compressing the sample by hand. The gauge factors were calculated with the average strain and changes in resistivity according to Equation 5.4, its evolution as a function of the quantity of graphene and PCL is shown in Figure 5.8.b. On average, all of the samples tested had a gauge factor in the same order of magnitude, except the composition at 6 wt% gf 2 wt% PCL which was measured at a much larger gauge factor. This difference was attributed to the optimal composition of the sample at very start of the conductivity plateau increasing the possibility of creating new electron paths when deformed. This is less observed for samples with 8 wt% gf where the network is already saturated and less electron path can be created by compression. This composition would, however, most likely show a higher gauge factor under traction, for example, where the destruction of electron paths dominates. The gauge factors increases again at 10 wt% gf as the dispersion becomes less stable, reducing the number of electron path as observed previously. Note that for these samples, the gauge factor was independent of the applied voltage since, as observed in Figure 5.6.c, their I-V behaviour was mostly linear with a resistivity independent of the applied voltage. The measured gauge factor was on the order of magnitude of what was observed with thermoplastic polyurethane (TPU) graphene composites [2] but one to two order of magnitudes below what was observed for carbon nanotubes [34] or high quality graphene [13].

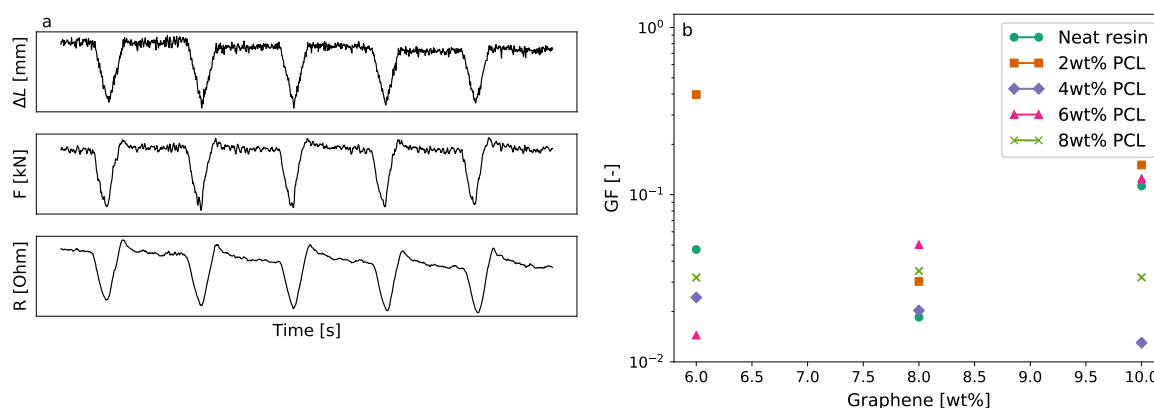


Figure 5.8: (a) Evolution of the deformation, force and resistivity during a cyclic sensing tests in compression for UP – 6 wt%gf 2 wt%PCL. (b) Gauge factor as a function of graphene and PCL content.

5.4. Conclusion

The electrical properties of unsaturated polyester glass fibre composites with different quantities of graphene and polycaprolactone were studied. The DC measurements showed a large increase in conductivity going from an insulating to a conductive regime increasing the quantity of graphene. The fibres orientation was found to influence the measured conductivity, and more specifically the composition at the percolation threshold. The high density of fibre tows in the transverse direction creates channels with higher local graphene content slightly shifting the percolation threshold toward lower quantities of graphene compared to the longitudinal direction. The addition of PCL has a similar effect on the percolation threshold creating graphene rich region in the UP-phase leaving the PCL-rich phase graphene-free. With the combination of these two effects, the percolation threshold was effectively reduced from 8.2 wt% of graphene for the system without fibre and PCL to 1.4 wt% of graphene with a fibre volume fraction of $V_f = 0.4$ and 2 wt% of PCL. The quantity and distribution of PCL also have significant impact on the electrical

behaviour. It was found that a fine dispersion of PCL-rich particles is more effective to reduce the percolation threshold compared to larger particles as it reduces the size of the effective electron paths. The current-voltage behaviour of these samples was of ohmic type above the percolation threshold with a strong linear dependency and a constant resistivity, indicating a direct contact conductivity. Conversely, it was found that at a composition just below the percolation threshold, where a non-linear behaviour was observed, conductivity was dominated by tunnelling. These trends were confirmed by AC frequency sweeps measurements where samples were found to conduct mainly through tunneling. A strong frequency dependent conductivity throughout the whole range of frequencies was observed. This behaviour was absent from the samples above the percolation threshold where the AC conductivity at lower frequency was constant and equal to the measured DC conductivity. These compositions showed good sensing capabilities by compression where the evolution of the resistivity with the applied strain followed closely the applied force. The electrical characterization and the compression tests confirm the potential to use multi-phase graphene composites as strain and damage sensors.

Acknowledgement

The authors thank their partners, Dr. Giovanna Gutiérrez and Dr. Abdou Khadri Diallo from NanoXplore Inc. for their helpful insights and feedback, NanoXplore Inc. for donating the graphene and the polyester resin, Ingevity for donating the thermoplastic, the Natural Sciences and Engineering Research Council of Canada (NSERC), Prima Quebec, the Research Center for High Performance Polymer and Composite Systems (CREPEC)

and Alexandra Brown for her help editing the final manuscript.

Funding

This work was supported by the Werner Graupe Fellowship, the Natural Sciences and Engineering Research Council of Canada (NSERC) grant RDCPJ 530253-18, Prima Quebec grant R16-46-005, the Research Center for High Performance Polymer and Composite Systems (CREPEC) and NanoXplore Inc..

References

- [1] R. Moriche, M. Sánchez, A. Jiménez-Suárez, S. G. Prolongo, and A. Ureña. Electrically conductive functionalized-GNP/epoxy based composites: From nanocomposite to multiscale glass fibre composite material. *Composites Part B: Engineering*, 98:49–55, 2016.
- [2] Hu Liu, Yilong Li, Kun Dai, Guoqiang Zheng, Chuntai Liu, Changyu Shen, Xingru Yan, Jiang Guo, and Zhanhu Guo. Electrically conductive thermoplastic elastomer nanocomposites at ultralow graphene loading levels for strain sensor applications. *Journal of Materials Chemistry C*, 4(1):157–166, 2015.
- [3] Heng Yang, Li Yuan, Xue Feng Yao, and Dai Ning Fang. Piezoresistive response of graphene rubber composites considering the tunneling effect. *Journal of the Mechanics and Physics of Solids*, 139, 2020.
- [4] Milad Madinehei, Scheyla Kuester, Tatiana Kaydanova, Nima Moghimian, and Éric David. Influence of graphene nanoplatelet lateral size on the electrical conductivity and electromagnetic interference shielding performance of polyester nanocomposites. *Polymers*, 13(15), 2021.
- [5] Federico Serenari, Milad Madinehei, Nima Moghimian, Davide Fabiani, and Eric David. Development of reinforced polyester/graphene nanocomposite showing tailored electrical conductivity. *Polymers*, 12(10):1–10, 2020.
- [6] Mohammad Sabzi, Masoud Babaahmadi, and Mohammadreza Rahnama. Thermally and Electrically Triggered Triple-Shape Memory Behavior of Poly(vinyl acetate)/Poly(lactic acid) Due to Graphene-Induced Phase Separation. *ACS Applied Materials and Interfaces*, 9(28):24061–24070, jul 2017.
- [7] Rajatendu Sengupta, Mithun Bhattacharya, S. Bandyopadhyay, and Anil K. Bhowmick. A review on the mechanical and electrical properties of graphite and modified graphite reinforced polymer composites. *Progress in Polymer Science (Oxford)*, 36(5):638–670, 2011.

- [8] Nima Moghimian and Soroush Nazarpour. The future of carbon: An update on graphene's dermal, inhalation, and gene toxicity. *Crystals*, 10(9):1–6, 2020.
- [9] Reza Taherian and Ayesha Kausar. *Introduction*. Elsevier, 2018.
- [10] Sabu Thomas, Mahesh Hosur, and Cintil Jose Chirayil, editors. *Unsaturated Polyester Resins: Fundamentals, Design, Fabrication and Applications*. Elsevier, 2019.
- [11] Jingwen Chu, Alexander J. Marsden, Robert J. Young, and Mark A. Bissett. Graphene-Based Materials as Strain Sensors in Glass Fiber/Epoxy Model Composites. *ACS Applied Materials and Interfaces*, 11(34):31338–31345, 2019.
- [12] Hu Liu, Qianming Li, Shuaidi Zhang, Rui Yin, Xianhu Liu, Yuxin He, Kun Dai, Chongxin Shan, Jiang Guo, Chuntai Liu, Changyu Shen, Xiaojing Wang, Ning Wang, Zicheng Wang, Renbo Wei, and Zhanhu Guo. Electrically conductive polymer composites for smart flexible strain sensors: a critical review. *Journal of Materials Chemistry C*, 6(45):12121–12141, 2018.
- [13] Jun Wei Zha, Bo Zhang, Robert K.Y. Li, and Zhi Min Dang. High-performance strain sensors based on functionalized graphene nanoplates for damage monitoring. *Composites Science and Technology*, 123:32–38, 2016.
- [14] Xue Wang, Weizhen Li, Zhao Zhang, Kaimin Chen, and Wenjun Gan. Selective localization of multi-walled carbon nanotubes in epoxy/polyetherimide system and properties of the conductive composites. *Journal of Applied Polymer Science*, 136(35):1–10, 2019.
- [15] Emna Helal, Rafael S. Kurusu, Nima Moghimian, Giovanna Gutierrez, Eric David, and Nicole R. Demarquette. Correlation between morphology, rheological behavior, and electrical behavior of conductive cocontinuous LLDPE/EVA blends containing commercial graphene nanoplatelets. *Journal of Rheology*, 63(6):961–976, 2019.
- [16] Hajime Kishi, Sanae Tanaka, Yasuaki Nakashima, and Takashi Saruwatari. Self-assembled three-dimensional structure of epoxy/polyethersulphone/silver adhesives with electrical conductivity. *Polymer*, 82:93–99, 2016.
- [17] Nathan Hostettler and Pascal Hubert. A phase separation strategy for enhanced toughness self-assembly graphene-network composites. *Composites Science and Technology*, 225(March):109503, 2022.
- [18] NanoXplore Inc. Technical Data Sheet - GrapheneBlack3X DS-GB3X-210803. 2021.
- [19] Alberto Bianco, Hui Ming Cheng, Toshiaki Enoki, Yury Gogotsi, Robert H. Hurt, Nikhil Koratkar, Takashi Kyotani, Marc Monthieux, Chong Rae Park, Juan M.D. Tascon, and Jin Zhang. All in the graphene family - A recommended nomenclature for two-dimensional carbon materials. *Carbon*, 65:1–6, 2013.
- [20] Peter Wick, Anna E. Louw-Gaume, Melanie Kucki, Harald F. Krug, Kostas Kostarelos, Bengt Fadeel, Kenneth A. Dawson, Anna Salvati, Ester Vázquez, Laura Ballerini, Mauro Tretiach, Fabio Benfenati, Emmanuel Flahaut, Laury Gauthier, Maurizio Prato, and Alberto Bianco. Classification framework for graphene-based materials. *Angewandte Chemie - International Edition*, 53(30):7714–7718, 2014.

- [21] A. J. Marsden, D. G. Papageorgiou, C. Vallés, A. Liscio, V. Palermo, M. A. Bissett, R. J. Young, and I. A. Kinloch. Electrical percolation in graphene-polymer composites. *2D Materials*, 5(3), 2018.
- [22] I. Y. Forero-Sandoval, F. Cervantes-Alvarez, J. A. Ramirez-Rincon, J. D. Macias, N. W. Pech-May, J. Ordonez-Miranda, and J. J. Alvarado-Gil. Percolation Threshold of the Thermal, Electrical and Optical Properties of Carbonyl-Iron Microcomposites. *Applied Composite Materials*, 28(2):447–463, 2021.
- [23] Mostafizur Rahaman, Ali Aldalbahi, Periyasami Govindasami, Noorunnisa P. Khanam, Subhendu Bhandari, Peter Feng, and Tariq Altalhi. A new insight in determining the percolation threshold of electrical conductivity for extrinsically conducting polymer composites through different sigmoidal models. *Polymers*, 9(10):1–17, 2017.
- [24] Abdelhafid Merzouki and Naceredine Haddaoui. Electrical Conductivity Modeling of Polypropylene Composites Filled with Carbon Black and Acetylene Black. *ISRN Polymer Science*, 2012:1–7, 2012.
- [25] I. Balberg, D. Azulay, D. Toker, and O. Millo. Percolation and tunneling in composite materials. *International Journal of Modern Physics B*, 18(15):2091–2121, 2004.
- [26] Yang Yuan, Qingguo Wang, Xiaoning Sun, Wenjie Dong, and Zhaoming Qu. Regulatable I–V behaviors of graphene nanoplatelets-carbon nanotubes/epoxy resin composite. *Materials Research Express*, 8(4):045302, apr 2021.
- [27] A. K. Jonscher. The 'universal' dielectric response. *Nature*, 267(June):673–679, 1977.
- [28] Chris R. Bowen, Sam Buschhorn, and Vana Adamaki. Manufacture and characterization of conductor-insulator composites based on carbon nanotubes and thermally reduced graphene oxide. *Pure and Applied Chemistry*, 86(5):765–774, 2014.
- [29] B. E. Kilbride, J. N. Coleman, J. Fraysse, P. Fournet, M. Cadek, A. Drury, S. Hutzler, S. Roth, and W. J. Blau. Experimental observation of scaling laws for alternating current and direct current conductivity in polymer-carbon nanotube composite thin films. *Journal of Applied Physics*, 92(7):4024–4030, 2002.
- [30] Elsayed Elbayoumy, Nasser A. El-Ghamaz, Farid Sh Mohamed, Mostafa A. Diab, and Tamaki Nakano. Dielectric permittivity, AC electrical conductivity and conduction mechanism of high crosslinked-vinyl polymers and their Pd(OAc)₂ composites. *Polymers*, 13(17), 2021.
- [31] Frank Gardea and Dimitris C. Lagoudas. Characterization of electrical and thermal properties of carbon nanotube/epoxy composites. *Composites Part B: Engineering*, 56:611–620, 2014.
- [32] Lilong Yang, Shuling Zhang, Zheng Chen, Yunliang Guo, Jiashuang Luan, Zhi Geng, and Guibin Wang. Design and preparation of graphene/poly(ether ether ketone) composites with excellent electrical conductivity. *Journal of Materials Science*, 49(5):2372–2382, 2014.

- [33] D. Nuzhnyy, M. Savinov, V. Bovtun, M. Kempa, J. Petzelt, B. Mayoral, and T. McNally. Broad-band conductivity and dielectric spectroscopy of composites of multiwalled carbon nanotubes and poly(ethylene terephthalate) around their low percolation threshold. *Nanotechnology*, 24(5), 2013.
- [34] Ning Hu, Takaomi Itoi, Taro Akagi, Takashi Kojima, Junmin Xue, Cheng Yan, Satoshi Atobe, Hisao Fukunaga, Weifeng Yuan, Huiming Ning, Surina, Yaolu Liu, and Alamusu. Ultrasensitive strain sensors made from metal-coated carbon nanofiller/epoxy composites. *Carbon*, 51(1):202–212, 2013.

PREFACE – CHAPTER 6

After having a deeper understanding of the electrical behaviour of the developed system from the previous chapter, the following chapter study the strain sensing capabilities of the optimized material system by direct resistivity measurement. The shape and direction of the resistivity response to traction, 3–point and 4–point bending are investigated and linked to the internal stress and strain. From this, a direct link between resistivity and elastic modulus is exposed. The evolution of the gauge factor with the solicitation mode and with the speed of testing is finally tested, showing the good potential of such system to be used as a strain self–sensor.

CHAPTER 6

Sensing capabilities and gauge factor of a multiscale multiphase graphene-based composite.

N. Hostettler, P. Hubert, International Conference on Composite Materials (2023)

Keywords: Self-sensing; multiscale composite; health monitoring

Abstract

The brittle nature of composite material makes them prone to failure, leading to high repair and maintenance costs. By adding graphene to a multiphase resin system, it is possible to create a self-assembly network of graphene leading to self-sensing properties through a measure of resistivity. For such material to be adopted into real applications, a characterization of its sensing capabilities is needed in several different loading mode to study its behaviour. This was done by reinforcing the resin system with a fibreglass preform and testing it in traction, 3- and 4-point bending. The resistivity change was recorded during each of these tests to assess its relation to stress and strain, and to calculate the gauge factor. In each case, the evolution of resistivity was found linearly linked with the applied stress and strain. That allowed to have a direct calculation of the elastic modulus from the resistivity and either the stress or strain. The gauge factors were found different between traction and bending. This was shown to be an effect of the traction/compression load superposition in bending. The reliable changes obtained in

resistivity with strain and stress together with high gauge factor makes this material a strong candidate for future self-sensing application.

6.1. Introduction

The addition of graphene to fibre reinforced plastics (FRPs) has many well-known advantages as the increase of toughness and electrical conductivity [1, 2]. This improvement in electrical properties unlock interesting applications for such system as actuators, fuel cells, photodetectors or mechanical sensors [3]. The latter is of interest since it allows direct tracking of the deformation and damage during a part's life by simply probing its resistivity, optimizing the part maintenance and repair [4]. Several studies were published in this scope [5–7]; however, it usually uses high purity chemical vapor deposition (CVD) graphene or carbon nanotubes (CNTs) that are expensive and comes at low production volumes. The alternative few-layers graphene (FLG) is required in larger amount to reach the conductivity threshold, decreasing the processability of the part. It is possible to create a self-assembly continuous network of graphene particles by blending the thermoset resin with a thermoplastic which shifts the percolation threshold [1]. This reduces the quantity of FLG needed for conduction and increases the toughness of the system. It is then possible to produce cost-effective self-sensing composite parts. When other research have shown the efficiency of such system, it was almost always on non-reinforced system and either in traction or compression. This paper focuses on the study of the electrical response of such system to different loading modes, its link to the elastic modulus, and the evolution of the “gauge factor” probing the sensing sensibility of the system.

6.2. Materials & Methods

6.2.1. Materials

The resin system was composed on a blend of PolyLite 31289 from Reichhold, a pre-accelerated unsaturated polyester (UP) and 2 wt% of CAPA6500, a polycaprolactone (PCL) from Ingevity. This system was cured with 2 wt% of Norox Azox from United-initiator. To this was incorporated 6 wt% of GrapheneBlack3X from NanoXplore, an industrial grade few-layer graphene (FLG) with a primary particle size between 1-2 μm and an agglomerate size of $D_{50} = 38 \mu\text{m}$, 6 to 10 graphene layers in thickness and a carbon to oxygen ratio of 96:1 [8]. This specific blend composition leads to a phase separated morphology with a preferential localisation of the graphene particles in the UP-rich region. This configuration strongly enhances the toughness of the system and reduces its percolation threshold [1]. The dispersion of the graphene was optimized by incorporating 1 wt% of Triton X100 diluted 15:1 in styrene as a surfactant, both from SigmaAldrich. Finally, the resin system was reinforced with a bidirectional-E glass-complex 0/90/Mat preform with a superficial density of 910 g/m^2 from SAERTEX.

6.2.2. Methods

Processing of the plates

The unsaturated polyester resin was weighted into a glass jar, the correct amount of graphene was added together with the surfactant and dispersed with a probe sonicator (Hielscher UP400St) for two cycles of 7 min spaced by a 15 min cool down step to limit the temperature increase below 70°C . The jar was then transferred into a 65°C water bath

where the PCL was added and was mechanically stirred for 20 min until homogeneous. The system was then let to rest at room temperature for 20 min to cool down and stabilize the phase-separated morphology. Next the initiator was incorporated, and the system was degassed for a 1–2 minutes to be ready for processing. The processing was conducted by compression resin transfer moulding on an MTS 250 kN servo-hydraulic testing machine with a 100x100 mm picture frame mould. The surface of the mould was prepared with Chemlease 2752W from ChemTrend to ease demoulding. The fibreglass preform [Mat/90/0]s was set into the mould topped with a 3.8 mm thick metallic shim frame (outer and inner size of 100 and 80 mm respectively) to create a pinching zone and favour the impregnation of the fibre tows. The plates were pressed to a target thickness of 1.8 mm ($V_f = 0.4$) at 0.05 mm/s and let to rest (mould closed to help impregnation of the fibre) for 7min before increasing the temperature to 50°C for an additional 7 min to cure the resin. The plates were demoulded and post-cured in an oven at 120°C for 2 h to complete the cure.

Mechanical tests and sensing capabilities

The sensing capabilities were investigated with three different loading mode: (i) 3-point bending, (ii) 4-point bending and (iii) traction. They were conducted on 20x70 mm coupons (0° fibres at the neutral axis) on an MTS 5 kN universal testing machine at room temperature. Each test consisted of 5 load/unload cycles separated by a 15s. waiting period; the first cycle was discarded from the analysis as it is usually highly asymmetric. The span for the 3- and 4-point bending were selected according to the ASTM D7264. The traction tests were conducted according to ASTM D3039, the displacement was probed with an MTS extensometer. To reduce the influence of the grips and to electrically

isolate the sample from the testing machine, 10x20 mm composite tabs (UP Neat and fibreglass) were glued on each side and at each end of the traction sample. For the bending tests, 3 mm wide silver paint electrode (SPI-supplies) were painted on each end of the sample. Similar electrodes were painted on the traction sample but after the tabs leaving a ~ 30 mm distance between each electrode. The resistivity was probed during the mechanical tests with a Keithley 6517A with a 10 V voltage directly applied on the silver electrodes. The resistivity was then calculated as:

$$\rho = \frac{RA}{l} = \frac{1}{\sigma} \quad (6.1)$$

where $A = t \cdot w$ is the cross section of the sample, R the measured resistance, l the distance in-between the electrodes and σ the conductivity. The sensibility of the sensing capabilities was measured with the gauge factor calculated as:

$$GF = \frac{\Delta R}{R_0 \varepsilon} \quad (6.2)$$

where $\Delta R = R - R_0$ is the instantaneous change in resistivity, R_0 is the initial resistance and ε is the applied strain measured from the displacement data. Two types of tests were conducted: (i) an amplitude study where the shape of the resistivity response was studied depending on the loading mode and load amplitude at a constant testing rate of 0.1 mm/s, and (ii) a strain rate study in traction, where the sample was loaded to 0.5 kN at different strain rate to assess the impact of the testing speed on the gauge factor.

6.3. Results & Discussion

6.3.1. Sensing capabilities

The evolution of the resistance during cycling is shown for each loading mode in Figure 6.1. The electric response is strong and consistent between each cycle confirming a deformation in the elastic region. As a plastic deformation would be characterized by a reduction of the number of electron paths leading to an increase of the baseline towards higher resistance. Two different behaviours are observed, both 3- and 4-point bending resulted in a decrease in the overall resistance of the system while the traction resulted in an increase in resistance. This is explained by the type of stress distribution in each loading mode. It is according to literature for the traction case [5, 9]. In traction the graphene particles are pulled away from each other breaking direct electron paths and increasing the tunneling distance which resulted in an overall increase of the resistance (see Figure 6.1.c). For the bending case, literature predicts a behaviour similar to traction with an increase in resistivity [10, 11], the tests were, however, performed on non-reinforced system. The presence of fibre then strongly effects the resistivity vs. strain behaviour and leads to a decrease in resistivity (see Figure 6.1.a and .b). In bending, the stress is composed on a coupling of traction (bottom half of the sample) and compression (upper half of the sample). A decrease in resistance is a sign that the graphene particles were pushed closer to each other, creating new conducting paths and lowering the tunneling distance [5, 12]. In the regime tested here, the deformation was then dominated by the compression of the upper surface of the sample. This can be shown calculating the strain in the upper and lower part of the sample. Under the assumption that the upper and bottom half part of the sample have a homogeneous compression and traction modulus E_C

and E_T , respectively (measured on the traction sample). From the force equilibrium of the system, the position of the neutral axes from the bottom of the sample h_b can be calculated as:

$$h_b = \frac{h}{1 + \left(\frac{E_t}{E_c}\right)^{1/2}} \cong 0.86 \text{ mm} \quad (6.3)$$

with $h = 1.8$ mm the thickness of the sample. Due to the different behaviour of the sample in traction and compression, the neutral axis is slightly shifted downward, the bottom half of the sample being stiffer than the upper part. From this the strain at the top and bottom of the sample can be calculated as:

$$\varepsilon_t = \frac{FLE_c(h - h_b)}{4D} \quad (6.4)$$

$$\varepsilon_b = \frac{FLE_t h_b}{4D} \quad (6.5)$$

where F is the applied force, L the span length and D the flexural stiffness defined as:

$$D = \frac{h}{3}(h_b^3 E_t + (h - h_b)^3 E_c) \quad (6.6)$$

Doing so, we find a compression strain ≈ 7.44 % larger with 3- and 4-point bending, following a similar approach, both independent from the applied load. This difference explains the dominant loss in resistivity in the bending loading modes. A characteristic second upward peak is, however, observed during each cycle in both 3- and 4-points bending, sign that the traction compression superposition is also present in the

resistivity data.

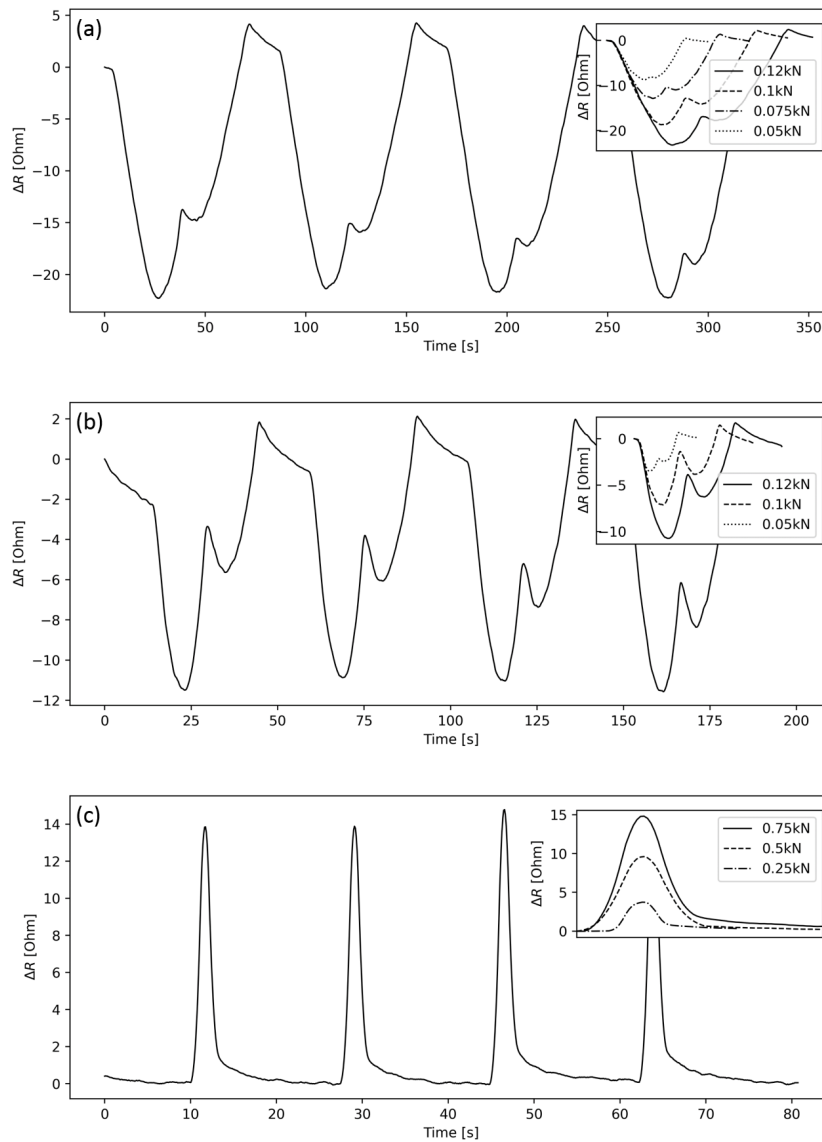


Figure 6.1: Resistance evolution with an applied load of 0.75kN and different load amplitudes (top right inserts) for: (a) 3-point bending, (b) 4-point bending and (c) traction.

The evolution of the resistivity with the applied force and applied strain is shown in Figure 6.2. Note that for readability, the absolute values of the data are depicted. The behaviour for each loading mode follows a close linear trend. The relation of the resistivity is similar between the force and strain, sign that a measure of resistivity could be used to indirectly measure either the force or strain, or the elastic modulus. This is shown in the

following equations:

$$\begin{aligned} \sigma(\Delta\rho) &= n_{\Delta\rho}\Delta\rho, \\ \Delta\rho(\varepsilon) &= n_\varepsilon\varepsilon, \\ \Rightarrow \sigma(\varepsilon) &= n_{\Delta\rho}n_\varepsilon\varepsilon \stackrel{?}{=} E_y\varepsilon \end{aligned} \tag{6.7}$$

where σ is the stress, $n_{\Delta\rho}$ the slope of the stress vs. resistivity curve, n_ε the slope of the resistivity vs. strain curve and E_y the slope of the stress vs. strain curve (the elastic modulus).

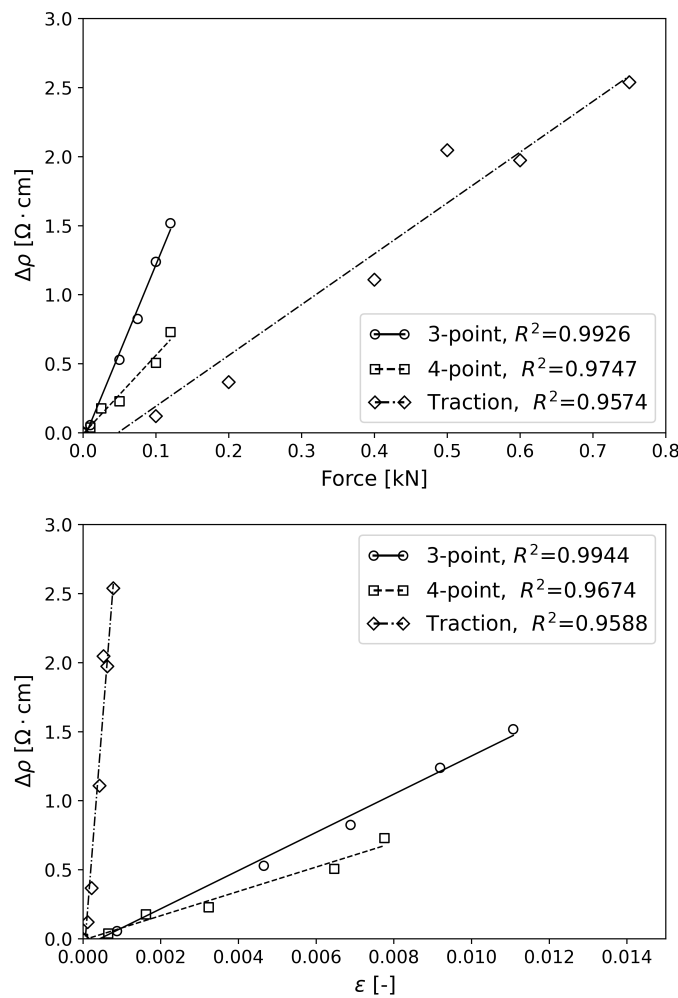


Figure 6.2: Resistivity evolution with (a) applied load and (b) applied strain.

The resulting modulus calculated from the resistivity data, $n_{\Delta\rho}n_\varepsilon$, and from the usual stress vs. strain data, E_y , are compared in Table 6.1. Both methods lead to similar values

of modulus confirming the possibility to use such materials as a reliable intrinsic stress or strain sensor.

Table 6.1: Comparison between the elastic modulus calculated from the resistivity and from the strain data.

	$n_{\Delta\rho} \cdot n_{\varepsilon}$ [GPa]	E_y [GPa]
3-point	4.4321	4.4327
4-point	4.3092	4.3091
traction	26.255	27.402

6.3.2. Gauge factor

The average gauge factor from each load amplitude and strain rate were calculated from equation 6.2 and are displayed in Table 6.2. The gauge factor measured in traction appear larger than the one in 3- and 4-point bending. This is explained by the dual traction/compression observed in flexion. Assuming the effect on the resistivity to be similar in traction and compression, in 3-point only 7 % of the strain is contributing to the “apparent” gauge factor. The real gauge factor in compression can then be estimated by scaling the apparent gauge factor to 100 % as follow:

$$GF_c = \frac{GF_a}{\left(1 - \frac{\varepsilon_t}{\varepsilon_c}\right)} \quad (6.8)$$

Doing so, it gives $GF_c = 16.16$ for 3-points and $GF_c = 11.14$ for 4-point bending, which is close to the actual compression gauge factor of the system. The proposed assumption on competing creation/destruction of electron paths is then validated. Note that these gauge factor are on the order of what is found in literature [5].

Table 6.2: Average gauge factor over the whole force range for the three-loading mode.

	GF
3-point	1.12 ± 0.29
4-point	0.83 ± 0.19
traction	22.19 ± 6.28
compression	17.31 ± 4.65

6.3.3. Gauge factor vs. strain rate

The strain rate influence on the gauge factor is vital in determining the suitability of using such material in real conditions. The evolution of the gauge factor as a function of the strain rate on the traction sample is shown in Figure 6.3. Both traction and compression were performed. In both cases, the gauge factor is linearly decreasing as the strain rate is increased. This is a viscoelastic effect reducing the strain at higher test speed which in its turn reduces the measured change in resistivity. The difference in slopes between the two cases is again due to the different behaviour of the material in traction and compression.

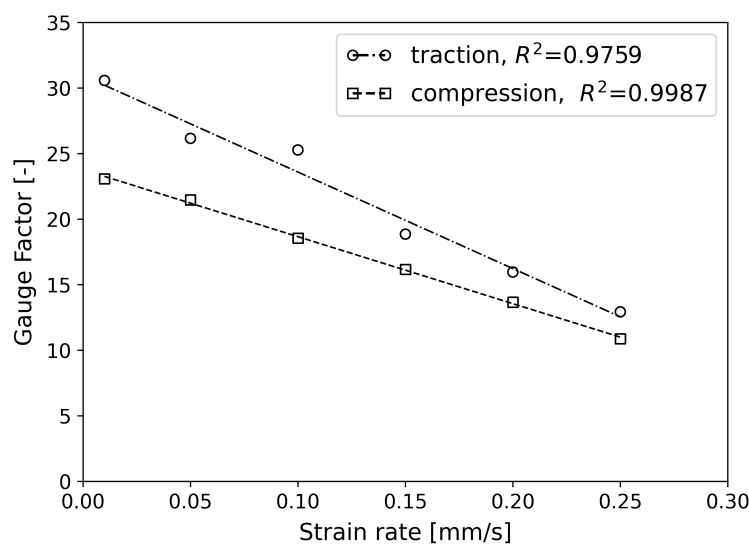


Figure 6.3: Evolution of the gauge factor as a function of the strain rate for the traction sample both in traction and compression.

6.4. Conclusion

The sensing capabilities of multiscale multiphase graphene-based composites was studied for three loading mode: traction, 3-point and 4-point bending. For each of them the shape as well as the influence of the load amplitude was studied. A clear link between the shape and the strain distribution through the sample thickness was found, exposing the coupled loading mode of bending (traction/compression). This observation was found to also apply to the gauge factor where the gauge factor in traction was retrieved from the bending tests. It was also demonstrated that such material can be used as strain/stress sensor, and successfully estimate the elastic modulus from the resistivity data. An increased strain rate was found to reduce the measured gauge factor due to the viscoelasticity nature of the system. However, this material system can be reliably used either as a strain sensor or as a force sensor in the elastic region with all three loading modes, or a coupling of them.

Acknowledgements

The authors thank their partners, Dr. Giovanna Gutiérrez and Dr. Abdou Khadri Diallo from NanoXplore Inc. for their helpful insights and feedback, NanoXplore Inc. for donating the graphene and the polyester resin, Ingevity for donating the thermoplastic, the Natural Sciences and Engineering Research Council of Canada (NSERC), Prima Quebec, the Research Center for High Performance Polymer and Composite Systems (CREPEC).

References

- [1] Nathan Hostettler and Pascal Hubert. A phase separation strategy for enhanced toughness self-assembly graphene-network composites. *Composites Science and Technology*, 225(March):109503, 2022.

- [2] Nathan Hostettler and Pascal Hubert. Electrical characterization and sensing capabilities of self-assembly multi-scale multi-phase graphene-based composites. *Carbon*, (xxxx), 2023.
- [3] Reza Taherian and Ayesha Kausar. *Introduction*. Elsevier, 2018.
- [4] R. Y.F. Liu, T. E. Bernal-Lara, A. Hiltner, and E. Baer. Polymer interphase materials by forced assembly. *Macromolecules*, 38(11):4819–4827, 2005.
- [5] A. J. Marsden, D. G. Papageorgiou, C. Vallés, A. Liscio, V. Palermo, M. A. Bissett, R. J. Young, and I. A. Kinloch. Electrical percolation in graphene-polymer composites. *2D Materials*, 5(3), 2018.
- [6] Christina Buggisch, Abedin Gagani, and Bodo Fiedler. Capacitance measurements on integrated conductors for detection of matrix cracks in GFRP. *Functional Composite Materials*, 2(1), 2021.
- [7] Christina Buggisch, Dennis Gibhardt, Nils Felmet, Yannick Tetzner, and Bodo Fiedler. Strain sensing in GFRP via fully integrated carbon nanotube epoxy film sensors. *Composites Part C: Open Access*, 6, 2021.
- [8] NanoXplore Inc. Technical Data Sheet - GrapheneBlack3X DS-GB3X-210803. 2021.
- [9] Sensen Han, Qingshi Meng, Aron Chand, Shuo Wang, Xiaodong Li, Hailan Kang, and Tianqing Liu. A comparative study of two graphene based elastomeric composite sensors. *Polymer Testing*, 80(September):106106, 2019.
- [10] A. Tamburrano, F. Sarasini, G. De Bellis, A. G. D'Aloia, and M. S. Sarto. The piezoresistive effect in graphene-based polymeric composites. *Nanotechnology*, 24(46), 2013.
- [11] P. Costa, J. Nunes-Pereira, J. Oliveira, J. Silva, J. Agostinho Moreira, S. A.C. Carabineiro, J. G. Buijnsters, and S. Lanceros-Mendez. High-performance graphene-based carbon nanofiller/polymer composites for piezoresistive sensor applications. *Composites Science and Technology*, 153:241–252, 2017.
- [12] Heng Yang, Li Yuan, Xue Feng Yao, and Dai Ning Fang. Piezoresistive response of graphene rubber composites considering the tunneling effect. *Journal of the Mechanics and Physics of Solids*, 139, 2020.

PREFACE – CHAPTER 7

Now that the strain sensing capabilities are well understood from last chapter, the final step of this research is to study the damage sensing capabilities of the developed system. For this two different methods are used: (i) direct resistivity measurement to study the damage progression during traction–traction fatigue testing, where the resistivity is directly compared to the crack prorogation during the test, and (ii) electrical impedance tomography (EIT) to reconstruct a 2D map of the conductivity distribution on two types of damaged plates (drilled holes and impacted).

CHAPTER 7

Multiphase multiscale graphene-based composite as intrinsic damage sensors.

N. Hostettler, P. Hubert

Keywords: Self-sensing; Damage sensing; multiscale composite; health monitoring

Abstract

The brittleness of fibre reinforced plastics (FRPs) make them prone to easy crack propagations. The tracking of such damage is of interest in order to reduce repair costs, and to prevent catastrophic damages which have significant environmental impacts. The use of few-layers graphene (FLG) as a conductive filler in composite system is seen as one of the possible solutions, creating intrinsic sensing materials through a local change in resistivity. The sensing capabilities of such a system was investigated, first in tension-tension fatigue probed by a direct measurement of the resistivity, and secondly on damaged plates using electrical impedance tomography (EIT) to reconstruct 2D maps of the damages. The system was found efficient to probe the damage in both of these scenario, with a change in resistivity directly related to the crack propagations in fatigue and adequately localized and quantified different types of damage (holes and impact) by EIT. These multiscale multiphase system were found to be strong candidates for self-sensing applications.

7.1. Introduction

The most significant issue in the use of fibre-reinforced plastics (FRPs) is damage control. Their natural brittleness leads to uncontrolled crack propagations, and difficulties to localize and quantify damages. There exists several nondestructive testing (NDT) methods to probe a composite part and identify its damage such as Ultrasonic C-scans, Thermography or Shearography [1, 2]. However, these methods usually either involve removing the composite part from service or having trained technicians scan the whole part on-site, which is not always possible. To solve this issue, efforts were made to include sensors directly in the composite part, for example, with embedded fibre optics [3, 4], but despite being efficient to track damage, they introduce non-structural defects in the material that can act as a preferential site for crack growth. Another strategy is the use of conductive fibres and nano-materials, the damage is then probed via a change in the local conductivity. This approach was successful with carbon fibres and allowed to identify the location of a damage [5, 6]. The detection was, however, limited to the fibre damages. The use of nano-materials like graphene, carbon nanotubes (CNTs) or carbon black (CB) were found successful in tracking the strains and damages in the polymer matrix, allowing a direct monitoring of its conditions during a static or cyclic solicitation by direct resistivity measurement [7–11] or after an impact by Electrical Impedance Tomography (EIT) [12–15]. The use of graphene in such cases has several advantages compared to CNTs and CB including its safer handling [16], ease of processing and dispersion. However, sensing applications typically use monolayer chemical vapor deposition (CVD) graphene or advanced processing techniques to process real size composite parts. Few-layer graphene (FLG) is the proposed alternative, specifically when used in a

phase-separating system. Such systems were found to create a self-assembly network of particles lowering the percolation threshold as well as increasing its toughness [17, 18]. The objectives of this paper is to investigate the capabilities of such a composite system to probe damage under cyclic solicitations and to localize impacts via EIT.

7.2. Experimental methods

7.2.1. Materials and Manufacturing

The resin system was the PolyLite 31289, a pre-accelerated unsaturated polyester (UP) from *Reichhold* and was cured with 2 wt% of Norox Azox from *United-initiator*. To create a toughened matrix system, 2 wt% of polycaprolactone (PCL) from *Ingevity* was blended in the UP resin leading to a two-phase system. To this was dispersed, with a probe sonicator (*Hischler* UP400St), 6 wt% of GrapheneBlack 3X from *NanoXplore inc.*, an industrial grade graphene with a primary particle size between 1 – 2 μm and an agglomerate size of $D_{50}=38 \mu\text{m}$ with 6 to 10 graphene layers in thickness [19]. This materials was classified as a few-layer graphene (FLG) nanoplatelets [20,21], this will be referred to as "graphene" for the remainder of this paper. To increase the degree of dispersion, 1 wt% of Triton X100 diluted 15:1 in styrene, to reduce its viscosity, was used as a surfactant. This system was pressed into a bidirectional-E glass-complex [MAT/90/0]_s using an MTS 250 kN in a 100 x 100 mm² open square mould for the impact samples and using a Wabash Genesis in a 280 x 280 mm² open mould for the fatigue samples. In both instances, 3.8 mm thick metallic shim frames (20 mm wide and at the dimension of the mould) were used to create a pinching zone at the extremity of the mould and increase the impregnation of the fibres. The initial cure was conducted at 50°C for 10 min followed by a 2 h post-cure at 120°C. The final

plates were 1.8 mm thick with a volume fraction of fibre $V_f = 0.4$. The exact procedure for each of these steps is detailed in our previous works [17, 18]. This process leads to a fine dispersion of the PCL in UP with graphene only located in the UP phase, leading to a strong increase in toughness and shift of the percolation threshold.

7.2.2. Fatigue testing and damage sensing

Tension-tension fatigue tests were conducted to study the sensing performance of the material system under a cyclic solicitation. According to ASTM D3479 and ASTM D3039, the samples were 250 x 25 mm with a gauge length of 120 mm tested on a MTS 100 kN. The samples were gripped with MTS 647 Hydraulic Wedge Grips at 10 MPa, avoiding the use of tabs or emery cloths. The ultimate fracture stress, σ_f , was measured on three samples at 2 mm/min until failure. This value was used to calculate the stress amplitude σ_a during the fatigue testing. They were performed at 1hz with an arbitrary amplitude of $\sigma_a/\sigma_f = 0.7$. The evolution of the resistivity was probed during the fatigue tests on a *Keithley 6517A* with an applied voltage of 10 V. To ensure good contact, 3 mm wide silver paint electrodes (*SPI-supplies*) were painted at a 10 mm distance from the grip, leaving a 100 mm active sensing region between the two electrodes. Additional tests were conducted to investigate the influence of the testing frequency and stress amplitude on the sensing performance, measured with the "gauge factor" (GF) defined as:

$$GF = \frac{\Delta R}{\epsilon R_0} \quad (7.1)$$

with ΔR the change in resistivity, R_0 the initial resistivity and ϵ the applied strain.

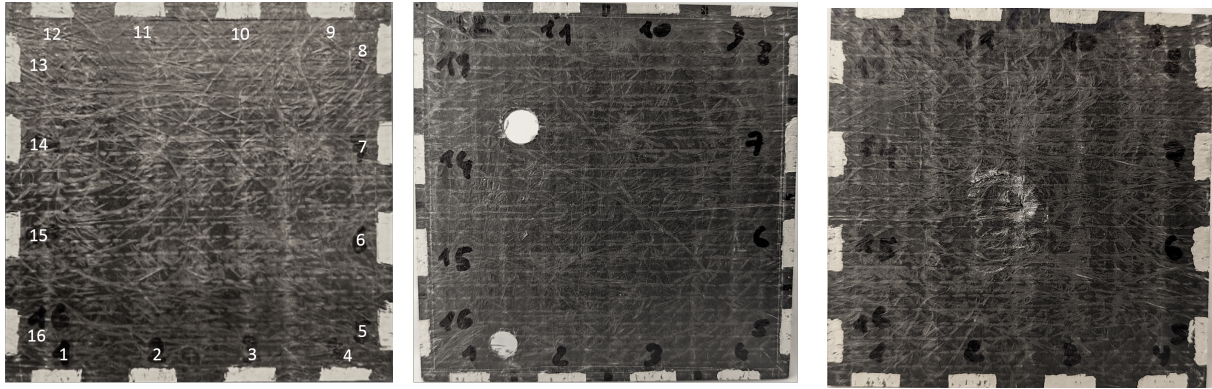


Figure 7.1: Plate investigated by electrical impedance tomography (from left-to-right): reference plate, drilled and impacted.

7.2.3. Electrical Impedance Tomography

EIT reconstructs the conductivity distribution of a body from known boundaries, and voltages at boundaries. For this, four silver electrodes (*SPI-supplies*) were painted on each plate sides (see Figure 7.1) and used as current injection points. An adjacent current injection method was chosen (see Figure 7.2), as it was previously reported to give reliable results in damage localization [12, 14]. A direct current (DC) of 10 mA was applied using a *Keithley 6221* with a maximum voltage compliance of 10V, the resulting voltage was probed on a *Keithley 2701* between each of the adjacent electrodes (excluding the injection ones). This was repeated for each group of adjacent electrodes. The results were used as boundary conditions in the MATLAB EIDORS toolbox (Electrical Impedance and Diffused Optical Reconstruction Software) using a Gauss-Newton EIT reconstruction approach. This method uses a regularized model of the EIT inverse problem and represents it as a linear reconstruction matrix [22]. For known conductivity, the boundary voltage response \mathbf{y} can be linearly solved as (EIT forward model): $\mathbf{y} = \mathbf{J}\mathbf{x} + \mathbf{n}$, where \mathbf{J} is the sensitivity matrix, \mathbf{n} is the noise and \mathbf{x} the conductivity distribution [5, 6, 22]. Note that the difference between neat and damaged plates were taken for \mathbf{x} to isolate the defects

contribution. The calculation of the voltage response from the boundary conditions is an inverse problem and is solved numerically. This is done by solving the one-step inverse solution [22]: $\hat{\mathbf{x}} = (\mathbf{J}^T \mathbf{V}^{-1} \mathbf{J} + \lambda^2 \mathbf{P}^{-1})^{-1} \mathbf{J}^T \mathbf{V}^{-1} \mathbf{y}$, where \mathbf{V} models the measurement accuracy, λ is the regularization hyperparameter - chosen by trial and error, and \mathbf{P} the regularization matrix - here the NOSER algorithm was used to minimize the noise at boundaries [22]. The 2D finite element model of the plate (FEM) was generated via EIDORS built-in Netgen package (see Figure 7.2). The meshing quality was checked via EIDORS mesh quality package and was deemed adequate. EIT was performed on two damaged plates, one with two drilled holes of different diameters (4 and 5 mm), and one with an impact created in an uncontrolled way. These plates are displayed in Figure 7.1. The EIT was compared to ultrasonic C-scans to assess its performance. They were conducted to compare the EIT results with a trusted damage investigation method. Measurement were first performed on the reference plate to calibrate the system and then on the two damaged plates to visualize the defects. The imaging was done on a TOPAZ 32 from Zetec with a Zetec ZPA probe¹ used at 2.25 MHz with a 0.6 mm step.

¹Zetec ZPA-PB1D-LM2.25-REX-2.5M-ZPAC

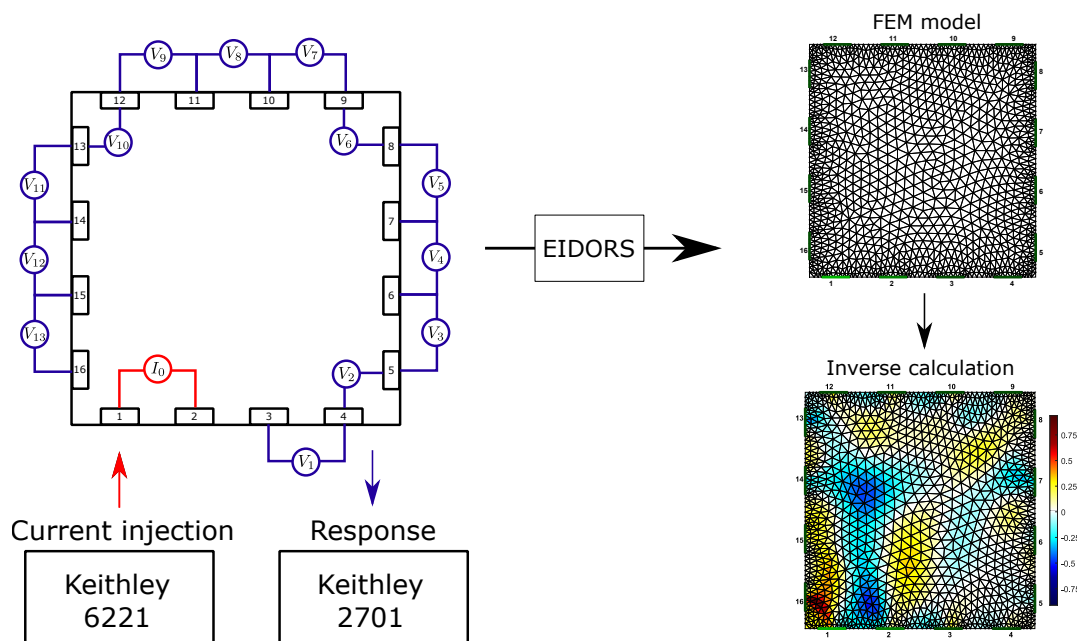


Figure 7.2: Current injection method, FEM and EIT concept.

7.3. Results and discussion

7.3.1. Tension-tension fatigue

The stress applied during fatigue tests was defined as a ratio of the maximal static stress, σ_f . A typical stress vs time curve is shown for such a test in Figure 7.3.a, together with the corresponding relative change of the sample's resistivity. As expected, the stress first increases linearly in a mostly elastic regime to finally see several quick drops corresponding to the propagation of cracks and finally a total mechanical failure. These drops are highlighted by vertical dashed lines and show corresponding increase in resistivity. The relative change in resistivity had a similar behaviour, first an elastic regime with a linear increase in resistivity, corresponding to the temporary destruction of electron paths through the system, followed by a plastic regime where the propagation of cracks lead to a quick and permanent increase of the resistivity. These jumps directly correspond

to the crack propagations observed on the stress curve. Interestingly the mechanical fracture did not directly correspond to the drop in resistivity. The majority of the stress was carried by the UD fibres, when the electrons flow through the matrix only. The stress curve then shows the fracture of the fibres, when the resistivity shows the fracture of the matrix. The fatigue tests were first conducted at $\sigma_a/\sigma_f = 0.7$ to investigate the cyclic sensing properties of the system. The stress vs. strain hysteresis for selected cycles is shown in Figure 7.3.b with corresponding resistivity change in Figure 7.3.c. The elastic modulus, E , along with the resistivity change for each cycle are displayed in Table 7.1. The modulus decreases during testing, as damages to the matrix and fibres are slowly growing. The baseline of the resistivity increases, as expected from the static tests, the crack propagation breaking the electron paths. In a similar way, a change in strain can also be reliably probed during testing, as shown in Figure 7.3.d, where the local average evolution of the strain is compared to the local relative average of the resistivity as a function of the number of cycle. The similar behaviour of the resistivity compared to stress and strain allows to have precise understanding of the condition of the part with simple resistivity measurements.

Table 7.1: Elastic modulus and relative change in resistivity at different testing cycles.

Cycle	1	250	500
Modulus [GPa]	13.78	12.96	12.33
$\Delta R/R_0$	1.56	2.26	2.38

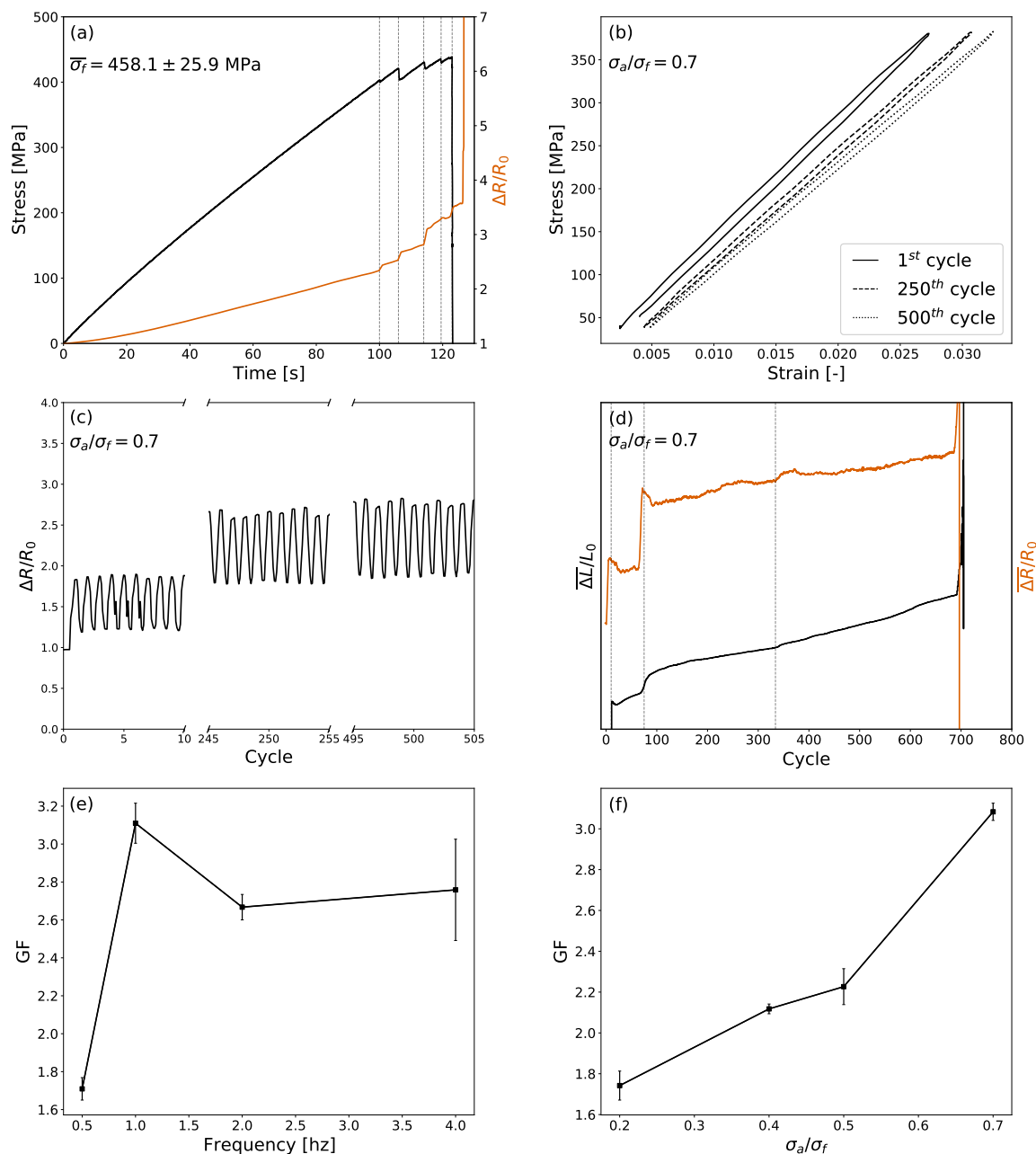


Figure 7.3: (a) Static tensile testing of the system showing the Stress vs. time curve (black) and the relative change in resistivity (orange) during the test, vertical dashed lines show crack propagations. (b) Fatigue Stress vs. Strain hysteresis comparing the change in slope between the 1st, 250th and 500th cycle. (c) Relative evolution of the resistivity around the 1st, 250th and 500th cycle. (d) Evolution of the local average resistivity and local average strain during fatigue testing, the vertical lines show the crack propagation. (e) Effect of the testing frequency in the gauge factor (GF). (f) Effect of the relative stress amplitude on the gauge factor.

The evolution of the gauge factor with the testing frequency and the stress amplitude is shown in Figure 7.3.e and .f. The gauge factor was fairly constant with the testing frequency with an exception at low frequencies where the materials had time to relax leading to a lower value of GF. At high frequencies, however, a higher error was recorded, which is likely due to the the viscoelastic behaviour of the matrix. Regarding the impact of stress, GF was found to linearly increase with the stress amplitude, which would make it a reliable stress and strain sensor. An interesting point to consider is the evolution of the gauge factor with the propagation of damage. There is an ambiguity, here, in the definition of the gauge factor as it is, normalized by the initial resistivity R_0 , for damage sensing. With this definition, GF will increase with the extent of damage, ΔR artificially increasing with the resistivity baseline while cracks propagate. This can be solved by simple redefining R_0 as the conductivity at the beginning of each cycles. By doing so, GF does not increase with the extent of damage anymore and stays fairly constant throughout the fatigue test.

7.3.2. 2D Damage localization

The EITs of the damaged plates were compared to ultrasonic C-scans to assess its performance and accuracy (see Figure 7.4). On C-scans, the colour contrast reflects the thickness of the plate: from dark blue when thin to dark red when thicker. On the EIT, the colour contrast represent a relative change in resistivity, blue indicates a loss and red a gain of conductivity. For the drilled plate (Figure 7.4.a), the two holes are easily found on the C-scan with two white dots corresponding to regions without signals, as expected for traversing holes where there is no interface to reflect the wave. The position as well as the size of the holes are accurately captured and directly match the measured plate. On the EIT, two zones of lower electrical conductivities are found (in blue) with positions close to

the actual holes positions but somewhat shifted. It would indicate that their positions are slightly affected by one-another, each zone slightly shifted toward the other, which could be an effect of the current injection pattern [12]. Their size, however, was adequately captured by the EIT and equivalent to the size of the holes. For the impacted plate (Figure 7.4.b), the C-scan showed a large zone affected by the impact: white regions corresponding to a total loss of signal, sign and highly damaged region, and green regions corresponding to smaller delaminations. The EIT captures adequately the directionality of the damage with a clear low conductivity zone spread toward the left of the plate. Closer to the side of the plate, the EIT measures a spread of the damage into two arms leaving a zone less damaged at the centre. This is also observed on the C-scan with a small orange region found far left of the plate in the middle of the delamination.

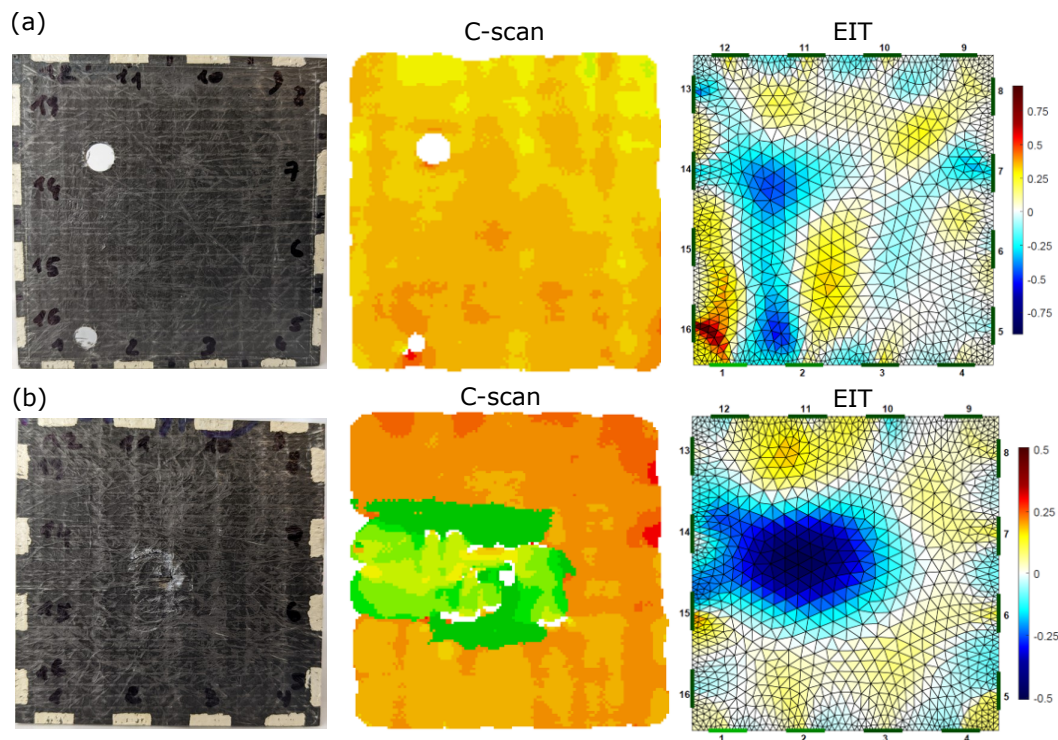


Figure 7.4: Comparison between ultrasonic C-scan and EIT for (a) drilled and (b) impacted plate.

7.4. Conclusion

The use of FLG as conductive filler in a phase-separating system was found successful for use as an intrinsic damage sensor. Tension-tension fatigue testing showed the capacity of such system to show crack propagation from a direct measurement of resistivity. A drop of the force signal was found to directly correspond to an increase of the measured sample resistivity. The effect of the testing frequency on the gauge factor is low. There is a loss in sensing capabilities at low frequency due to relaxation and an increase of the measurement error at high frequency. The gauge factor was found to be linearly linked with the stress amplitude. Electrical impedance tomography (EIT) was used on two types of damaged plates, one impacted and the other drilled with two holes of different diameters. The position as well as the size of these defect were successfully identified matching corresponding C-scans. The use of a multiscale multiphase system enables interesting intrinsic damage sensing properties that would allow a better tracking conditions during operation.

Acknowledgement

The authors thank their partners, Dr. Giovanna Gutiérrez and Dr. Abdou Khadri Diallo from NanoXplore Inc. for their helpful insights and feedback, NanoXplore Inc. for donating the graphene and the polyester resin, Ingevity for donating the thermoplastic, the Natural Sciences and Engineering Research Council of Canada (NSERC), Prima Quebec, the Research Center for High Performance Polymer and Composite Systems (CREPEC), Julien Walter and Olivier Arès from the Aerospace Technology Centre (CTA) for the ultrasonic C-scans.

References

- [1] R. H. Bossi and V. Giurgiutiu. *Nondestructive testing of damage in aerospace composites*. Elsevier Ltd, 2015.
- [2] S. Gholizadeh. A review of non-destructive testing methods of composite materials. *Procedia Structural Integrity*, 1:50–57, 2016.
- [3] Bo Hun Choi and Il Bum Kwon. Strain pattern detection of composite cylinders using optical fibers after low velocity impacts. *Composites Science and Technology*, 154:64–75, 2018.
- [4] Manjusha Ramakrishnan, Ginu Rajan, Yuliya Semenova, and Gerald Farrell. Overview of fiber optic sensor technologies for strain/temperature sensing applications in composite materials. *Sensors (Switzerland)*, 16(1), 2016.
- [5] Helena Rocha, Christophe Fernandes, Nelson Ferreira, Ugo Lafont, and João P. Nunes. Damage localization on CFRP composites by electrical impedance tomography. *Materials Today Communications*, 32(July), 2022.
- [6] Susanne Nonn, Martin Schagerl, Yingjun Zhao, Sandra Gschossmann, and Christoph Kralovec. Application of electrical impedance tomography to an anisotropic carbon fiber-reinforced polymer composite laminate for damage localization. *Composites Science and Technology*, 160(February):231–236, 2018.
- [7] Pawan Verma, Jabir Ubaid, Kartik M. Varadarajan, Brian L. Wardle, and S. Kumar. Synthesis and Characterization of Carbon Nanotube-Doped Thermoplastic Nanocomposites for the Additive Manufacturing of Self-Sensing Piezoresistive Materials. *ACS Applied Materials and Interfaces*, 14(6):8361–8372, 2022.
- [8] Ayako Yoshida, Yi-Fei Wang, Tomohito Sekine, Yasunori Takeda, Daisuke Kumaki, and Shizuo Tokito. Printed Low-Hysteresis Stretchable Strain Sensor Based on a Self-Segregating Conductive Composite. *ACS Applied Engineering Materials*, 2022.
- [9] Hu Liu, Yilong Li, Kun Dai, Guoqiang Zheng, Chuntai Liu, Changyu Shen, Xingru Yan, Jiang Guo, and Zhanhu Guo. Electrically conductive thermoplastic elastomer nanocomposites at ultralow graphene loading levels for strain sensor applications. *Journal of Materials Chemistry C*, 4(1):157–166, 2015.
- [10] Jingwen Chu, Alexander J. Marsden, Robert J. Young, and Mark A. Bissett. Graphene-Based Materials as Strain Sensors in Glass Fiber/Epoxy Model Composites. *ACS Applied Materials and Interfaces*, 11(34):31338–31345, 2019.
- [11] Hu Liu, Qianming Li, Shuaidi Zhang, Rui Yin, Xianhu Liu, Yuxin He, Kun Dai, Chongxin Shan, Jiang Guo, Chuntai Liu, Changyu Shen, Xiaojing Wang, Ning Wang, Zicheng Wang, Renbo Wei, and Zhanhu Guo. Electrically conductive polymer composites for smart flexible strain sensors: a critical review. *Journal of Materials Chemistry C*, 6(45):12121–12141, 2018.
- [12] A. J. Thomas, J. J. Kim, T. N. Tallman, and C. E. Bakis. Damage detection in self-sensing composite tubes via electrical impedance tomography. *Composites Part B: Engineering*, 177(June):107276, 2019.

- [13] Hongbo Dai and Erik T. Thostenson. Large-Area Carbon Nanotube-Based Flexible Composites for Ultra-Wide Range Pressure Sensing and Spatial Pressure Mapping. *ACS Applied Materials and Interfaces*, 11(51):48370–48380, 2019.
- [14] Fuchao Hao, Shaokai Wang, Fei Xing, Min Li, Tianshu Li, Yizhuo Gu, Wei Zhang, and Jiahui Zhang. Carbon-Nanotube-Film-Based Electrical Impedance Tomography for Structural Damage Detection of Carbon-Fiber-Reinforced Composites. *ACS Applied Nano Materials*, 4(5):5590–5597, 2021.
- [15] Jinwon Oh, Jun Chang Yang, Jin Oh Kim, Hyunkyu Park, Se Young Kwon, Serin Lee, Joo Yong Sim, Hyun Woo Oh, Jung Kim, and Steve Park. Pressure insensitive strain sensor with facile solution-based process for tactile sensing applications. *ACS Nano*, 12(8):7546–7553, 2018.
- [16] Nima Moghimian and Soroush Nazarpour. The future of carbon: An update on graphene’s dermal, inhalation, and gene toxicity. *Crystals*, 10(9):1–6, 2020.
- [17] Nathan Hostettler and Pascal Hubert. A phase separation strategy for enhanced toughness self-assembly graphene-network composites. *Composites Science and Technology*, 225(March):109503, 2022.
- [18] Nathan Hostettler and Pascal Hubert. Electrical characterization and sensing capabilities of self-assembly multi-scale multi-phase graphene-based composites. *Carbon*, (xxxx), 2023.
- [19] NanoXplore Inc. Technical Data Sheet - GrapheneBlack3X DS-GB3X-210803. 2021.
- [20] Alberto Bianco, Hui Ming Cheng, Toshiaki Enoki, Yury Gogotsi, Robert H. Hurt, Nikhil Koratkar, Takashi Kyotani, Marc Monthieux, Chong Rae Park, Juan M.D. Tascon, and Jin Zhang. All in the graphene family - A recommended nomenclature for two-dimensional carbon materials. *Carbon*, 65:1–6, 2013.
- [21] Peter Wick, Anna E. Louw-Gaume, Melanie Kucki, Harald F. Krug, Kostas Kostarelos, Bengt Fadeel, Kenneth A. Dawson, Anna Salvati, Ester Vázquez, Laura Ballerini, Mauro Tretiach, Fabio Benfenati, Emmanuel Flahaut, Laury Gauthier, Maurizio Prato, and Alberto Bianco. Classification framework for graphene-based materials. *Angewandte Chemie - International Edition*, 53(30):7714–7718, 2014.
- [22] Andy Adler, John H. Arnold, Richard Bayford, Andrea Borsic, Brian Brown, Paul Dixon, Theo J.C. Faes, Inéz Frerichs, Hervé Gagnon, Yvo Gärber, Bartłomiej Grychtol, Günter Hahn, William R.B. Lionheart, Anjum Malik, Robert P. Patterson, Janet Stocks, Andrew Tizzard, Norbert Weiler, and Gerhard K. Wolf. GREIT: A unified approach to 2D linear EIT reconstruction of lung images. *Physiological Measurement*, 30(6), 2009.

CHAPTER 8

Conclusion

8.1. Original Contributions

Advancements in self-sensing graphene-based composites allow a better control of strain and damage in a part, by simple resistivity measurements. However, the current approaches usually use high quality CVD graphene in a non-reinforced matrix, far from any industrial composite applications. Therefore, the main objective of this research was to develop a self-sensing system based out of few-layer graphene (FLG), needed in larger amount to get the matrix conductive, and optimize the matrix microstructure to concentrate the particles in one region to reduce the percolation threshold. This was achieved by blending the unsaturated polyester (UP) resin with polycaprolactone (PCL), creating a self-assembly network of FLG by phase-separation and reinforced by a non-crimp fibreglass preform. The impact of these on the mechanical, electrical and sensing capabilities were studied, and the main conclusion and contributions resulting from this research are the following:

1. The toughness and electrical conductivity of the resin system are strongly impacted by the addition of graphene and polycaprolactone (cf. Chapter 3).

The addition of PCL to the UP was found to increase up to 90 % the toughness with only 4 wt% of PCL. This effect was found linked, not only to the primary

morphology of phase-separation and the inter-phase region, but to the secondary phase-separated morphologies as well. The smaller these morphologies the higher the toughness increase, due to the increased crack path during fracture. Similarly, the addition of graphene led to a 98 wt% increase with 6 wt% gf. The individual effect of graphene and PCL on the toughness was found non directly cumulative, but still leading to an increase of 114 % compared to the neat resin. From this combination, a self-assembly network of graphene was created in the UP-rich region leaving the PCL-rich region graphene free. This strongly shifted the electrical percolation threshold toward lower quantity of graphene. Such phase-separated structure interestingly showed a double percolation behaviour, one coming from the graphene and one from the interconnectivity of the UP-rich phase.

Original contribution:

A novel self-assembly resin system toughened by graphene and PCL with reduced electrical percolation threshold, and a deepened understanding of the fracture mechanisms in such multiphase system.

2. Optimized processing conditions and fibre geometry are key to manufacture multiphase resin system into composite plates by compression resin transfer moulding (cRTM) (cf. Chapter 4).

Several issue are encountered when processing a graphene-based multiphase system in a fibreglass preform by cRTM in an open mould, starting with the impregnation of the fibres tows. The addition of graphene and PCL increase the viscosity of the resin system leading to less impregnated fibre tows. The use of a metallic shim frame was found highly effective to solve this issue by creating a region of lower permeability

around the part, forcing the resin in the preform. The phase-separation was found unaffected by the glassfibres and moulding pressure, leaving the morphology studied in Chapter 3 unchanged and equivalent in the reinforced system. Filtering of graphene particles by the reinforcement, usually found in the other research, was avoided by a clever choice of non-crimped fibre geometry which leaved large inter-tows channel for the graphene to flow through. These channels also create graphene-rich region, the graphene particles being too large to enter the fibre tows.

Original contribution:

Development of the processing method as well as identification and optimization of important processing parameters when manufacturing multiphase multiscale graphene-based composites.

3. The percolation threshold in the transverse and longitudinal direction as well as the AC/DC conductivity (and electron paths) are strongly impacted by the phase-separated morphology, graphene and glassfibres (cf. Chapter 5).

The DC conductivity was first dominated by tunnelling at low graphene content before sharply reaching a plateau at higher graphene content, where a direct electron flow is carried between graphene particles. The transverse conductivity was found two order of magnitudes lower than the longitudinal one, due to the perpendicular orientation of the fibre to the electron flow, limiting the number of electron paths. Consequently, these regions were saturated faster than the longitudinal direction, leading to an overall lower percolation threshold in the transverse direction. The presence of graphene-rich region in between the fibre tows, together with the self-assembly network of graphene, strongly reduced the percolation threshold down

to 1.4 wt% gf (2 wt% PCL) compared to 8.2 wt% gf for the neat resin (cf. Chapter 3). The ratio between the size of the morphology and size of the graphene flakes was identified as a critical factor to create effective electron paths and optimize the shift of the percolation threshold as well as the final electrical conductivity. These systems were always of ohmic type above the percolation threshold, with a linear I-V behaviour. This was lost below the percolation threshold where larger distance between graphene particles promote an electron flow by tunnelling leading to a parabolic I-V behaviour. This validated the definition of the percolation threshold as the first occurrence of direct electron flow in the material. A low quantity of PCL, leading to a fine dispersion of PCL-rich phase, was found to be the most effective to reduce the distance between the particles and helped creating more direct electron paths. The opposite was found above the phase inversion composition, where the UP-rich phase is segregated by PCL-rich region. The AC conductivity showed a typical universal dielectric response above the percolation threshold where the frequency dependence of the conductivity behaves as a power law. At lower graphene content, the conductivity was frequency independent as expected from a dielectric material. The resulting conductivity exponent matched the definition of a disordered material of randomly varying energy barrier, which is a good representation of a multiscale multiphase system.

Original contribution:

Development of a behavioural model for the electron flow in a multiphase multiscale material depending on the added quantity of PCL and graphene.

4. The piezoresistive behaviour of the resin system can be used for sensing and is closely linked to the applied strain and damage present in the part (cf. Chapter 5, 6 and 7).

The resistivity response was found dependent on the direction of the applied stress, compression pushing the graphene particles closer and decreasing the resistivity, when the opposite was observed in traction. The highest gauge factor, or sensing capacity, was found for compositions at the beginning of the conductivity plateau, just above the percolation threshold (6 wt%gf and 2 wt%PCL). With this composition, a linear behaviour was observed between resistivity and strain, allowing the accurate measurement of the elastic modulus from resistivity measurements. The traction compression superposition observed in bending were also identified in the resistivity curves with a superposition of upward and downward peaks. The capacity to probe damage was tested in traction-traction fatigue where the propagation of cracks during the tests was directly linked to sharp increase in resistivity. Finally, this material was successfully used to reconstruct 2D conductivity maps and localized damage by electrical impedance tomography (EIT).

Original contribution:

Sensing capabilities investigations of a reinforced self-sensing system capable of monitoring strain and damages in different sollicitation modes by simple resistivity measurement.

All these helped identify the "magic composition" UP – 6 wt%gf 2 wt%PCL that maximizes the toughness (cf. Chapter 3), shift in percolation threshold and electrical conductivity (cf. Chapter 3 and 5), and gauge factor (cf. Chapter 5 and 6). This using the lowest quantity of

graphene and PCL possible. The presented research also stands as a proof of concept that can be adapted to other type of resin systems, opening a wide range of possible applications.

8.2. Publications in Referred Journals

1. N. Hostettler and P. Hubert, "A phase separation strategy for enhanced toughness self-assembly graphene-network composites." *Composites Science and Technology*, 225:109503, (2022), DOI: <https://doi.org/10.1016/j.compscitech.2022.109503>
2. N. Hostettler and P. Hubert, "Electrical characterization and sensing capabilities of self-assembly multi-scale multi-phase graphene-based composites." *Carbon*, vol 208, pp.131-139, (2023), DOI: <https://doi.org/10.1016/j.carbon.2023.03.005>

8.3. Suggestions for Future Work

The presented research provides a strategy to use few-layer graphene in reinforced multiphase system for self-sensing applications. There are several interesting opportunities to further study with these type of systems:

1. The strain sensing capabilities need to be further investigated for complex loading modes to understand the influence of electrodes position and spacing on the local sensing precision.
2. The damage sensing capabilities was demonstrated with impacts and holes of simple geometries. However, the capabilities to localize more complex damages as well as non-traversing holes needs to be assessed further. A closer study of the signal and how it could be used to quantify the extend of damage should also be conducted.

3. The demonstrated capabilities need to be verified on larger and more complex structures. Especially how the parts size influences the voltage needed to have an efficient sensing and overcome the background noise.
4. The influence of temperature and humidity on the electrical properties is another key point that needs to be further investigated. Especially, the possibility to decouple the contributions of strain and temperature to the resistivity. If done properly, resistivity measurements could give maps of the applied strain and of the local internal temperature of the system.
5. The electrical properties of the developed system open the doors to numerous applications. The multi-functionality of such system can be extended further as electromagnetic shielding and deicing structures, for example.
6. Finally, this work can be seen as a proof-of-concept and the same development should be done with different resin system and thermoplastic in order to reach larger panel of applications.

Appendices

PREFACE – CHAPTER A

The COVID-19 pandemic gave us some forced time-off at the beginning of 2020. This time was allocated to a side project with the idea of using molecular dynamic simulation as a tool to create polymer phase-diagrams and better understand the impact of temperature, molar mass and degree of cure on the evolution of the Gibbs free energy. This chapter can be seen as a simulation extension of Chapter 3. Even if a complete study of the subject was far from being achieved, the obtained results were interesting enough to be included as a bonus chapter in the appendix.

CHAPTER A

Molecular dynamic approach to the calculation of solubility and interaction parameters - A first look into building phase-diagrams.

A.1. Introduction

Polymer blends are commonly used in industry to adjust the properties and increase the toughness of the resin system [1, 2]. These blends also offer advantages such as creating self-assembly networks of particles through preferential localization [3, 4]. However, the mechanisms behind these phenomena are not well understood and development is often done through trial and error. This can be improved by using simulation to complement experimental trials. The Flory-Huggins free energy model is often used to study phase separation and compute enthalpic and entropic contributions to Gibbs free energy [5]. One important parameter in this model is the Flory-Huggins interaction parameter χ , which represents the miscibility of the polymers. This parameter is difficult to measure and is often fitted to experimental data. Molecular dynamic (MD) simulations have shown potential in predicting polymer properties [6–9], but direct simulation of phase separation is usually not feasible due to computational limitations. An indirect approach using Hildebrand solubility parameters can be used to estimate Gibbs free energy [10–13], this was successfully conducted by a selection of studies but usually on solvent-polymer systems [14]. This study aims: (i) to simulate the interaction parameters for

polycaprolactone (PCL) and styrene to validate the simulation framework, (ii) to study the evolution of the interaction parameter for unsaturated polyester (UP) with molar mass, temperature and degree of cure, involving a simulation of the curing process and (iii) the creation of UP/PCL phase-diagram based on simulated interaction parameters.

A.2. Methodology

A.2.1. Hildebrand solubility parameters

The Hildebrand solubility parameter δ provides a description on the miscibility of a mixture. It is defined as the square root of the cohesive energy density (CED), the energy needed to bring a substance from solid to vapour [12]:

$$\delta^2 = \frac{\Delta H_v - RT}{V_m} \quad (\text{A.1})$$

with ΔH_v the heat of vapourization, R the perfect gas constant, T the temperature and V_m the molar volume. It can be used to estimate the interaction parameters χ in a mixture of polymers according to the so called *Hildebrand-Scott* equation [13]:

$$\chi_{AB} = \frac{\sqrt{V_A V_B}}{RT} (\delta_A - \delta_B)^2 \quad (\text{A.2})$$

Note that in this form, it is assumed that χ_{AB} is independent from the composition of the blend. This parameter is widely used when studying polymer blends, and is needed to create phase-diagrams using the Flory-Huggins definition of Gibb's free energy.

A.2.2. Flory-Huggins free energy model

Phase separations are highly dependent on the components miscibility. In order to observe such phenomena in a mixture of two components, the system must reach a state of homogeneous equilibrium where the initially immiscible component becomes miscible. That can be done using several levers as temperature or pressure, but also by adapting the molecular weight of the polymers. Increasing the molar mass of a chain at constant composition or mass would lead to a decrease of the entropy of mixing. In polymeric systems where this value is already typically small, a change in the chain length can be enough to observe a change in phase behaviour [15]. This observation is also true in a system containing a mixture of thermoset and thermoplastic where the initially dissolved thermoplastic will eventually phase separate during the cure of the thermoset. Here, it is a quick increase of the molar mass that will create a strong enough local perturbation to move the system out of equilibrium, this is called a reaction induced phase separation [5]. In such a case, the curing rate is highly influencing the final morphology of the system, principally quickly reducing the coefficient of auto-diffusion of the thermoplastic. There is then a balance between a strong reaction that will trap the thermoplastic chains in the thermoset structure and a weak reaction that won't create a strong enough perturbation for the phase separation to take place.

The polymer thermodynamic representation of phase separation is commonly done by the classical Flory-Huggins model for the free energy of mixing [16]:

$$\frac{\Delta G_{mix}}{kT} = \frac{\phi_A}{N_A v_A} \ln \phi_A + \frac{\phi_B}{N_B v_B} \ln \phi_B + \frac{\phi_A \phi_B}{v_{AB}} \chi_{AB} \quad (\text{A.3})$$

with ΔG_{mix} the gibbs free energy, k is Boltzmann constant, T the temperature, ϕ_i the volume fraction of the i -th component, N_i the number of segment per molecule i , v_i is the segmental volume, v_{AB} is the average segmental volume and finally χ is the interaction parameter. This relation was adapted for reaction induced phase separation by Williams *et al.* [5]:

$$\Delta G_{mix} = \frac{RT}{V_r} \left[\frac{\phi_A}{Z_A(\alpha)} \ln \phi_A + \frac{\phi_B}{Z_B} \ln \phi_B + \chi_{AB} \phi_A \phi_B \right] \quad (\text{A.4})$$

with R the perfect gas constant, V_r a reference molar volume, $Z_A(\alpha)$ is the ratio between the thermoset molar volume and the reference volume as a function of the degree of cure α . Z_B is the ratio between the thermoplastic molar volume and the reference volume that is independent from the degree of cure. These molar volumes can be replaced by the more convenient molar masses during the calculation. In the case of a n -component system Equation A.4 can be adapted as:

$$\Delta G_{mix} = \frac{RT}{V_r} \left[\sum_{i=1}^n \frac{\phi_i}{Z_i} \ln \phi_i + \sum_{i=1}^n \sum_{j \neq i}^n \chi_{ij} \phi_i \phi_j \right]. \quad (\text{A.5})$$

In each case, two parameters need to be determined: the evolution of the average molar mass with the degree of cure $M_n(\alpha)$ and the interaction parameters χ . Unsaturated polyester resins cure through free-radical co-polymerization where, for an ideal reaction model, the evolution of molar mass can be expressed by a modification of the *Flory-Stockmayer* theory [17]:

$$M_n = \frac{M_{n,0}}{1 - \frac{\alpha}{\alpha_c}} \quad (\text{A.6})$$

where $M_{n,0}$ and M_n are respectively the number average molecular weight before and during the cure, α the degree of cure and $\alpha_c = 0.3$ the critical degree of cure (in this case the degree of cure at gelation). Such simplified model was shown to have a rather bad fit with the experimental because the cure of the unsaturated polyester is characterized by the formation of polyester microgels at the early stage of the reaction due to a strong tendency for intra-molecular cyclization [18]. It is, however, a decent approximation in this case since the molecular dynamic simulation of the cure will not simulate this phenomenon. A possible deviation with the experimental is, however, to be expected. Note that this restriction would not be seen with epoxies where these relations are well established [19].

A.3. Molecular dynamic method

The solubility parameters were calculated for three types of molecules: polycaprolactone (PCL), styrene (St) and unsaturated polyester (UP). When the size of the two first molecules does not evolve during cure, the size of polyester chains get larger as the curing reaction goes. This could influence the interaction parameter χ and make the phase diagram slightly evolve during the cure. The evolution of the interaction parameter with the degree of cure $\chi(\alpha)$ was also studied by MD simulation. The different methods used for these simulations are described in what follows.

A.3.1. Definition of the simulation box

The different molecules were drawn in *Chem3D* (see Figure A.1). To each of these was applied the generic *Dreiding* force field through a python code [20]. The structure of the simulation box was created by stacking the desired number of molecules using the packing optimization package *Packmol* [21]. The forcefield was then applied to the optimized

packed structure using *Moltemplate* [22] which creates the final simulation box, a low density amorphous polymer structure. A flowchart for the creation of the simulation box is shown in Figure A.2. To improve the accuracy of the model, the semi-empirical *Qeq* method [23] was used for the charge assignment and equilibration of each molecules. The simulations were performed with the software LAMMPS [24] using the computational power of the Digital Research Alliance of Canada.

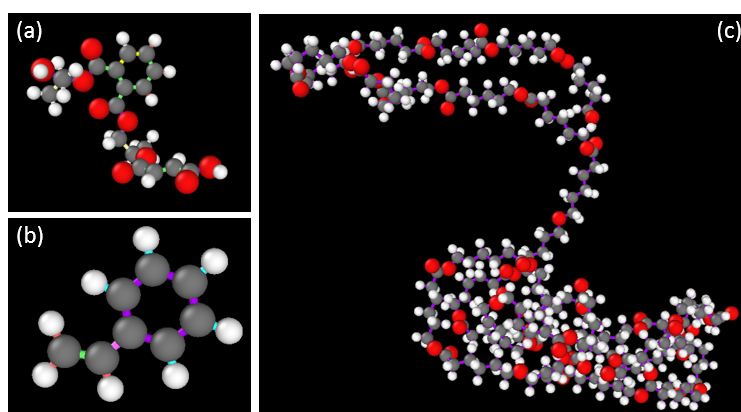


Figure A.1: Molecules created in Chem3D: (a) UP (n=1), (b) St and (c) PCL (n=30)

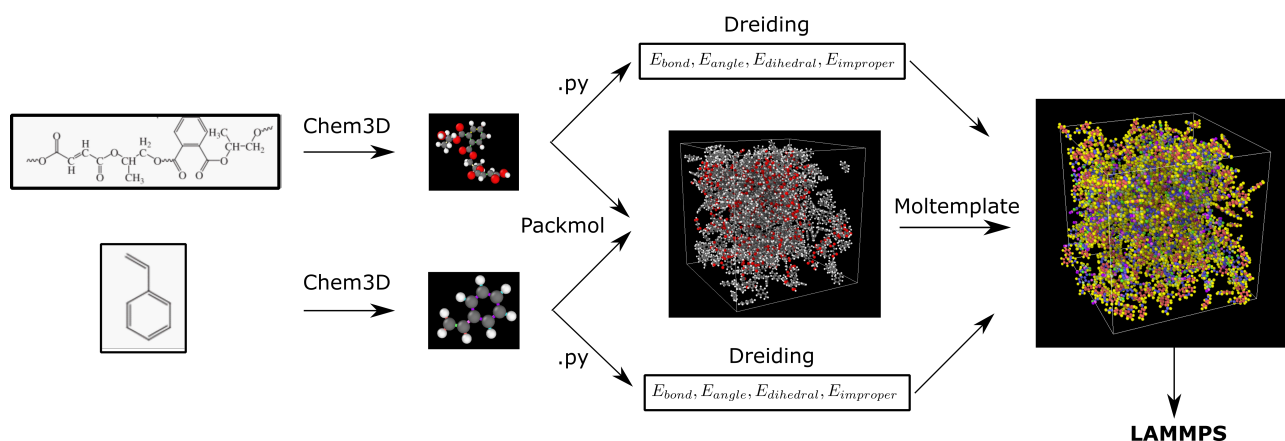


Figure A.2: Flowchart - Creation of the simulation box.

For the simulations to be accurate, two main factors need to be respected: (i) a condensed phase density and (ii) equilibrated molecular conformations. This can be achieved by a sequence of compression and expansion steps, until the system stabilizes to the target density. This method was developed by *Belmares et al.* [12] and was conducted

as follow: (i) the energy of the system was minimized for 5k steps using a *steepest descent* algorithm, (ii) the system was annealed at 700 K and let to equilibrate for 20k fs under a canonical fixed volume dynamics (NVT), (iii) the system was compressed shrinking its density by $(\rho_{high} - \rho_{low})/5$, step (i) and (ii) were then repeated to stabilize the atomic coordinates. This was reproduced five times until the density reaches $\rho_{high} = 1,25 \cdot \rho_{target}$. The simulation cell was then expended in a similar manner to the target density (experimental density), the energy of the system was minimized to relax the atomic coordinates and thermalized to the target temperature. Finally, a stabilization step was conducted for 10k fs before taking the measurement under isothermal-isobaric (NPT) conditions at 1 atm and target temperature. This approach was followed for each molecules to reach the target density either before cure for UP or before measuring the solubility parameter using the CED method.

A.3.2. Curing method

The curing of unsaturated polyester happens by free radical copolymerization in a two-step process [25]: (i) the initiator reacts with the double bonds of the unsaturated polyester which creates a reaction site for styrene molecules, (ii) the styrene bonds with the unsaturated polyester, which creates free radicals for other styrenes to react. This creates a long chain of styrene molecules attached to an unsaturated polyester molecule. In LAMMPS, atoms are defined by types depending on their nature and number of coordination. The cure is simulated by a step process linking two "atoms types" which makes it difficult to reproduce the real curing process. For example, simulating the cure as a two step process as described above (see Figure A.3): (i) linking "atom type (1)" of the unsaturated polyester with "atom type (2)" of the styrene, and (ii) linking "atom type (3)"

to "atom type (2)" to build a long styrene chain attached to the UP. This method would successfully bond styrene to the UP chain but it would also bond any styrene together, bonded to UP or not (see Figure A.3). This side reaction is not representative of the real curing method and would lead to an artificially higher degree of cure.

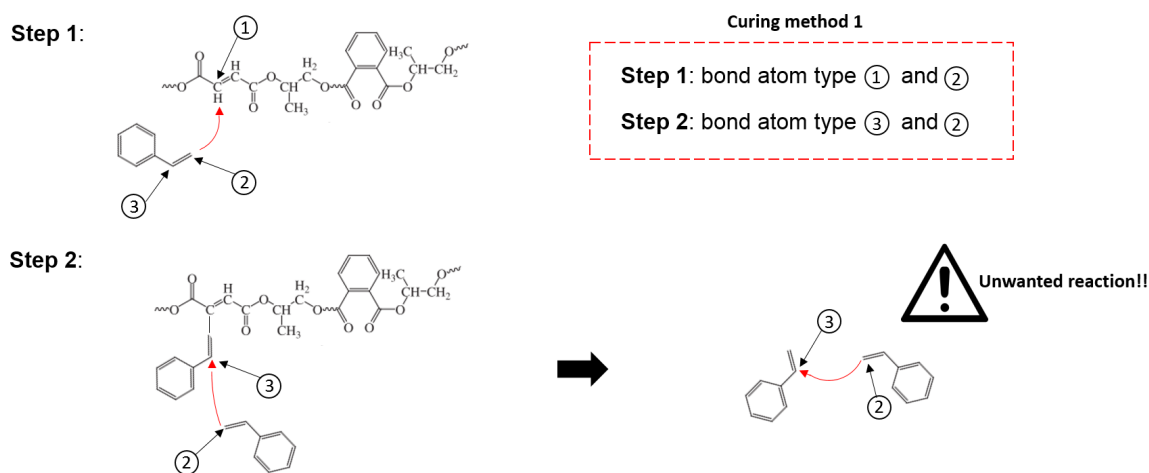


Figure A.3: Curing method 1 in LAMMPS.

To avoid this side reaction, two steps can be added to the previous simulation (see Figure A.4): (i) link "atom type (2)" of the styrene with "atom type (1)" of the unsaturated polyester, (ii) change the "atom type (3)" of the unbonded styrene to an arbitrary "atom type (3')", (iii) bond "atoms type (2)" of the unbonded styrene with "atom type (3)" of the bonded styrene and (iv) change back the atom type of unbonded styrene from (3') to (3). This is done for every time step of the curing process which mimic closely the real chemical reaction. In such a simulation, the cure kinetic of the system is not correctly represented as the software bonds atoms depending on a target distance rather than a chemical activity. This is not an issue here as these simulations were conducted to create unsaturated polyester at different degree of cure rather than studying its cure kinetic.

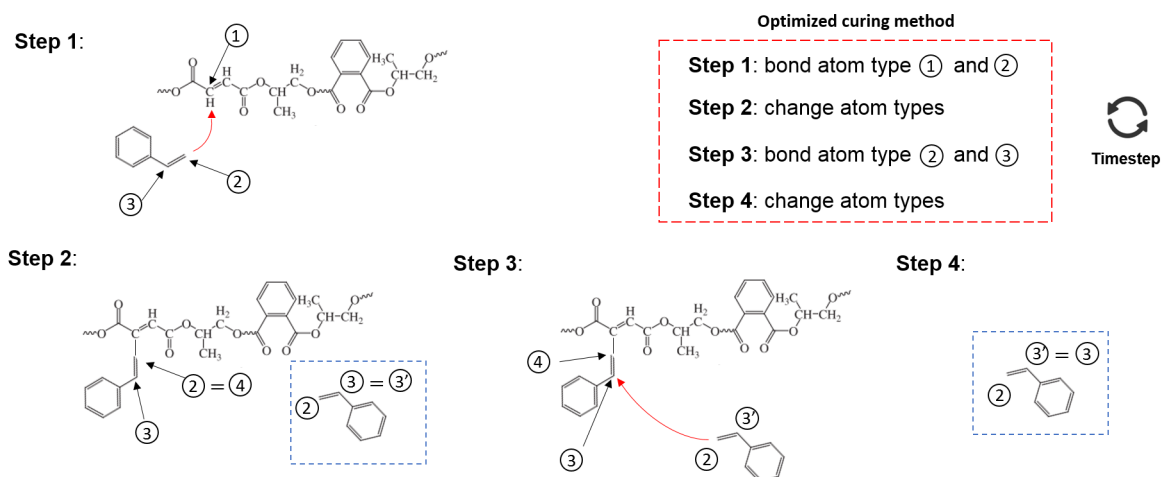


Figure A.4: Optimized curing method in LAMMPS.

The cure was simulated at 50°C using LAMMPS `<bond/create>` built-in function, looking for atoms to bond every 10 timesteps if their distance was smaller than 3.9Å. The structure was exported at several degree of cure, typically $\alpha = 0.1/0.2/0.3/0.4$ and was performed on unsaturated polyester with several molar mass $n = 2/4/8/16/32$. After the cure, styrene molecules were evaporated from these structure prior running the stabilization procedure described in Section A.3.1.

A.3.3. Cohesive energy density method

The method to calculate the Hildebrand solubility parameter is based on the average potential energy of a single cell in a condensed phase E_c and E_i the energy component of the individual molecules. It can be calculated as follow [12]:

$$\delta^2 = \frac{\langle E_i - E_c \rangle}{N_0 \langle V_c / n \rangle} \quad (\text{A.7})$$

where n is the number of molecules, N_0 Avogadro's number, V_c the volume of the simulated cell and $\langle \rangle$ represent a time average over the simulated data. This value was

calculated for styrene, PCL and unsaturated polyester at different degree of cure and molar mass. To study the influence of temperature, the simulation was performed at 25, 50 and 75 °C. The simulations were conducted in a NPT ensemble, from the stabilized structure at the target density obtained from the stabilization procedure presented above, the system was brought to the target temperature for in 10k timesteps and stabilized at that temperature for 30k additional timesteps. The measurement of each energy components was then carried taking the average value over 10k steps using the $\langle \text{compute 1 all pe pair} \rangle$ and $\langle \text{compute 2 all group/group all molecule intra} \rangle$ commands. The obtained Hildebrand solubility parameters were then used in Equation A.2 to calculate the interaction parameters.

A.4. Results & Discussion

A.4.1. Curing process

The degree of cure α of each simulated system was calculated based on the quantity of unreacted styrene molecules as follow:

$$\alpha = 1 - \frac{n_{styrene}}{n_{styrene}^0} \quad (\text{A.8})$$

with $n_{styrene}$ and $n_{styrene}^0$ the remaining and initial number of unbonded styrene. Doing so, it was possible to track the evolution of the cluster size with the degree of cure (see Figure A.5). At $\alpha = 0$ the two cluster size are representative of the styrene at 16 and UP at 91 atoms. As the cure goes, the styrenes molecules are bonded to the UP backbone increasing the cluster size by increment of 16 atoms. This is a sign of styrene being bonded to already

bonded styrene and that the cure is happening as expected. Reaching $\alpha = 0.42$, two larger cluster size are observed, this is a sign of the creation of a large network of several UP molecules linked by styrene chains. Similar behaviour were observed for UP at larger molar mass, usually leading to a lower degree of cure because of the lower number and reduced mobility of the chains. This cure simulation allowed to extract UP at different degree of cure for different initial molar masses.

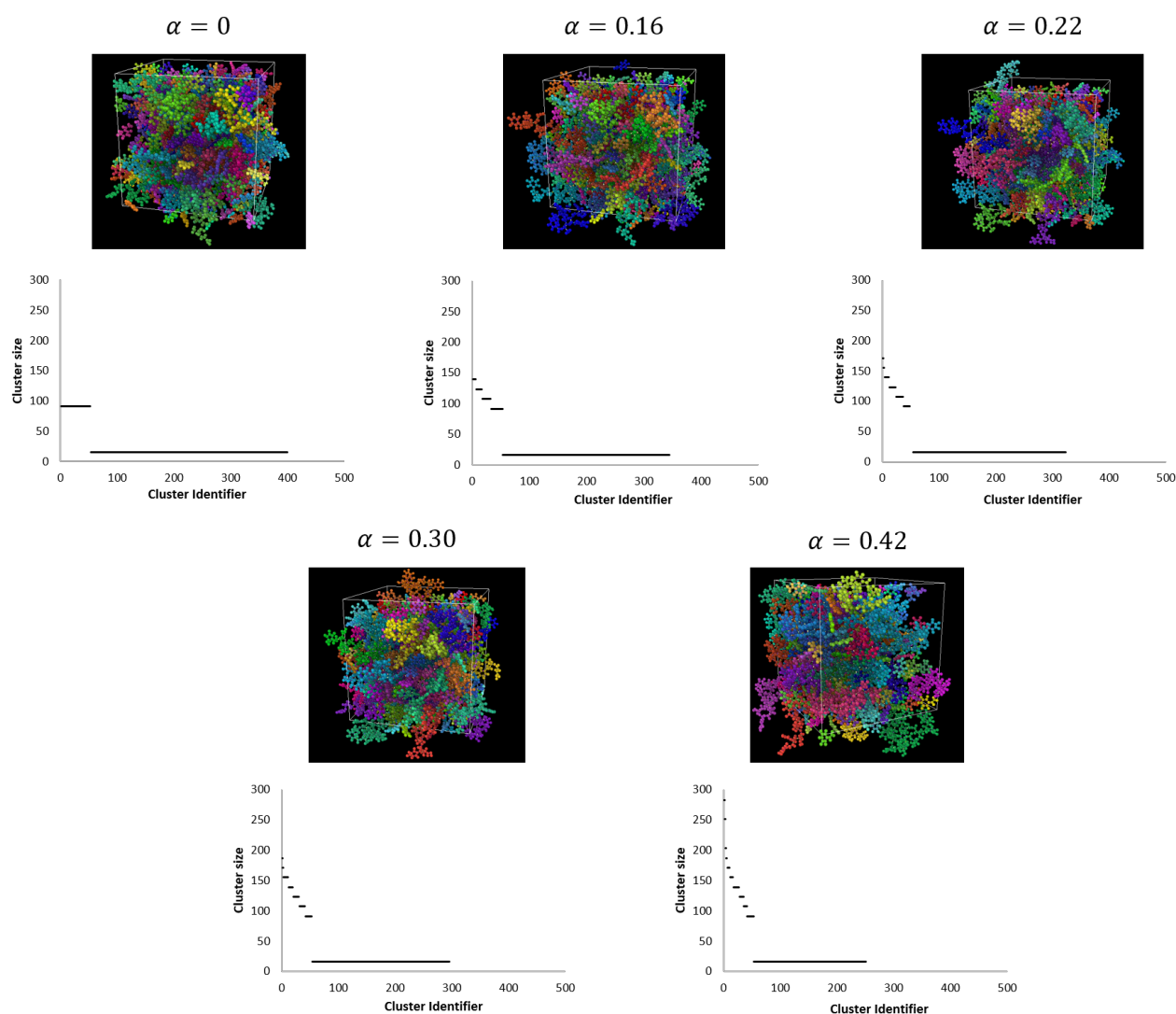


Figure A.5: Evolution of the cluster size with the degree of cure for UP ($n=2$).

A.4.2. Hildebrand solubility parameters

The Hildebrand solubility parameters were calculated according to the CED method based on Equation A.7. The results for the PCL ($n = 30$) and Styrene are shown in Table A.1. The values obtained with the simulation represent rather well the experimental solubility parameters, which validates the simulation method. The small difference can be attributed to the used model that underestimates the hydrogen bonds contribution. When the experimental solubility parameters usually slightly decrease with an increase in temperature, the simulated ones first increase with temperature up to 323 K before decreasing at higher temperature.

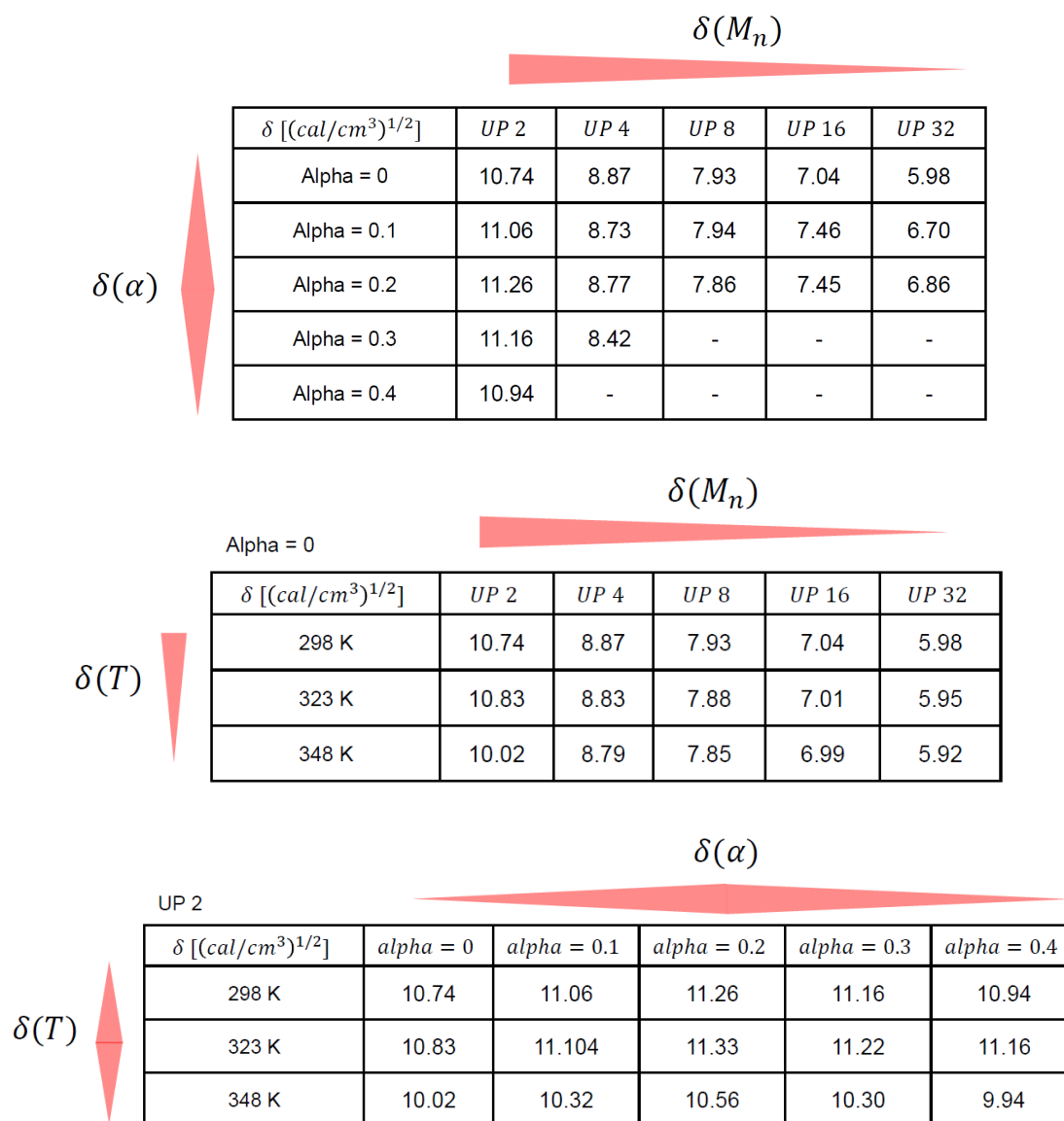
Table A.1: Calculated and literature Hildebrand solubility parameters for PCL ($n=30$) and Styrene.

$\delta[(cal/cm^3)^{1/2}]$	298K	323K	348K
PCL - CED	7.832	7.835	7.817
PCL lit. [26]	9.85	9.272	8.695
Styrene - CED	10.153	10.488	10.146
Styrene lit. [27]	9.29	-	-

The evolution of the solubility parameters of the unsaturated polyester with its initial molar mass M_n , degree of cure α and temperature are displayed in Table A.2. The values found for the UP's Hildebrand solubility parameters are usually close to $11.6 (cal/cm^3)^{1/2}$ [28], this was close to what was obtained with UP ($n = 2$). When increasing the molar mass of UP, the solubility parameter decreased linearly which was according to what was found in the literature [29]. The solubility parameter was found to slightly increase during the cure until reaching a degree of cure of $\alpha = 0.2$, after which it starts to decrease. This change in behaviour somewhat correspond to the experimental gel points. This was again close

to what was expected from literature where two regimes were observed with a transition at the gel point [30]. Finally, the solubility parameters slightly increased with temperature before decreasing at higher temperature. These changes were found stronger at higher degree of cure which was in opposition to what was usually observed in literature [30], where the larger changes are found for the lower degree of cure. The overall evolution of the solubility parameters with degree of cure, molar mass and temperature was, however, adequately predicted by the model.

Table A.2: Evolution of the solubility parameters of UP as a function of the molar mass, degree of cure and temperature



A.4.3. Interaction parameters and Gibbs free energy

The interaction parameters between the UP and the PCL were calculated according to Equation A.2 and the simulated solubility parameters, they are represented as function of the initial molar mass of UP and degree of cure in Figure A.6. The general behaviour was similar for each of the temperatures with a characteristic inversed bell curve, with smaller interaction parameters at 75°C and UP($n = 2$) compared to the ones at 25 and 50°C. These curve represent the stability of UP and PCL blends (independently of the composition) for varying initial molar mass of UP and degree of cure [31]. The blend was homogeneous below the bell curve and heterogeneous, with the presence of two phases, above the curve. By increasing the molar mass of UP, the miscibility of the two polymers decreases with a minimum around UP($n = 8$), after which the miscibility increases again slightly. The cure, while having a small impact at lower molar mass of UP, decreases the miscibility of the system at larger initial molar mass of UP. This is usually expected from a polymerization induced phase-separation. The evolution of the interaction parameter with the temperature is shown in Figure A.7.

In the Flory-Huggins definition of the interaction parameters, χ is considered to be reciprocal of the temperature: $\chi = a + b/T$. This was well observed for the samples with initial molar mass larger than UP($n = 2$). For this latter behaviour diverges somewhat from linearity.

Using as input the interaction parameters and the evolution of the molar mass according to Equation A.6 in the Flory-Huggins model for the free energy of mixing, it was possible to reconstruct the binodal phase diagram solving for the temperature (see Figure A.8). The characteristic bell curves obtained show the stability domain of the UP/PCL blend as a

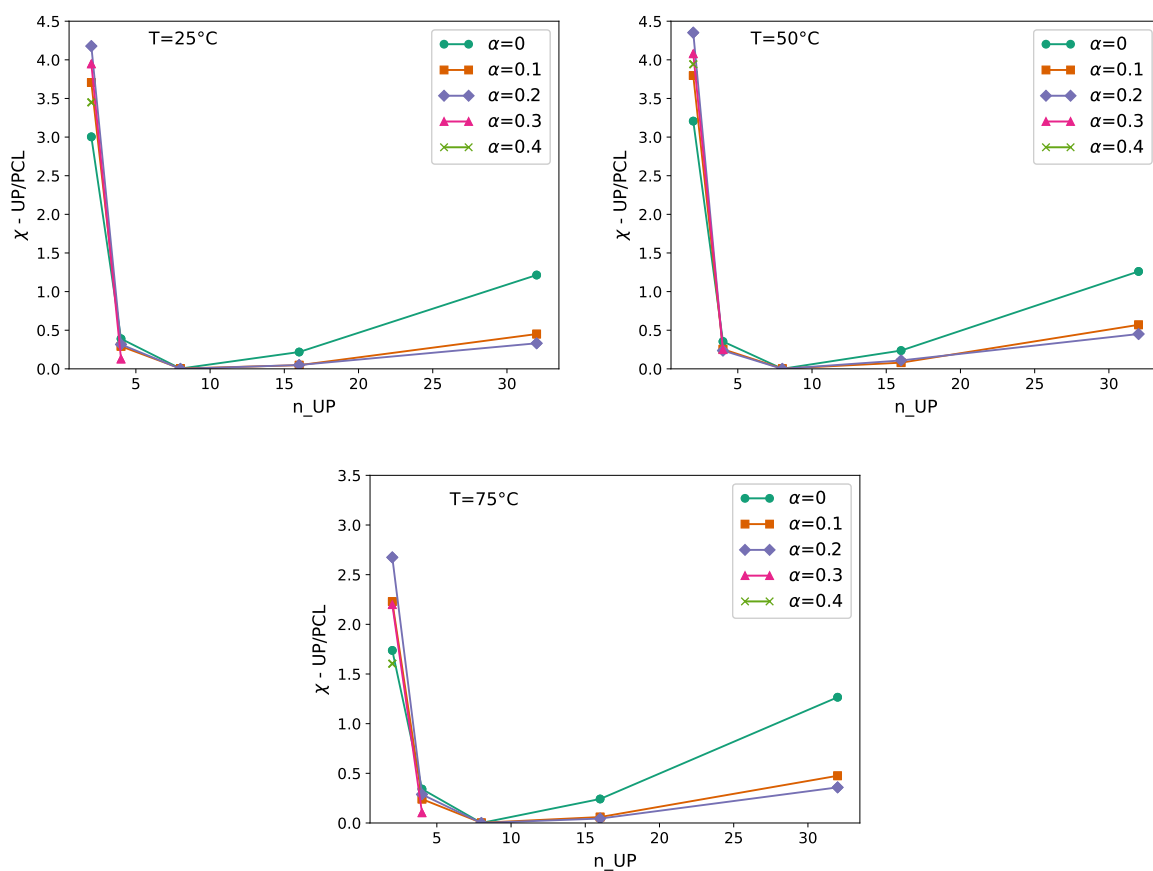


Figure A.6: Evolution of the interaction parameter with the initial molar mass of UP and degree of cure at 25, 50 and 75°C.

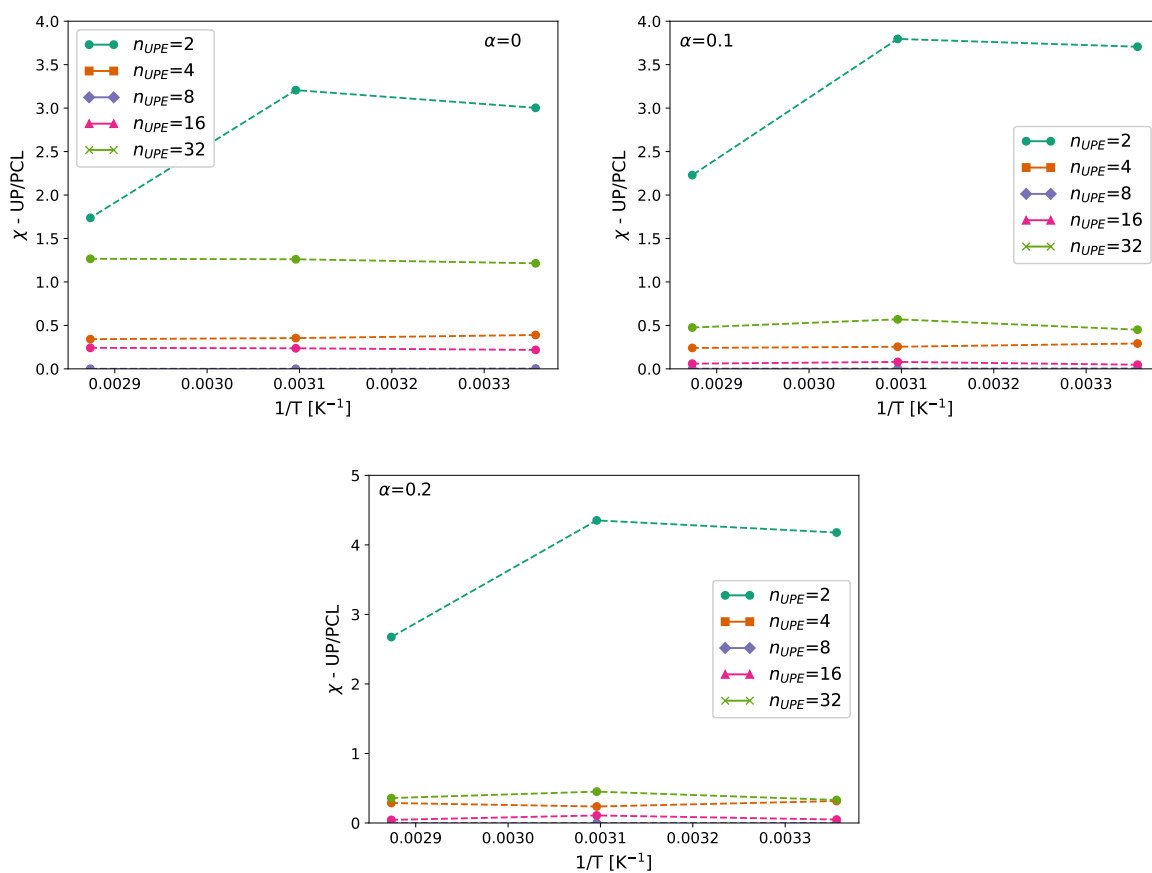


Figure A.7: Evolution of the interaction parameter as a function of $1/T$ for different initial molar mass of UP and degree of cure.

function of the temperature and composition. The region above the curve is the unstable region where the system phase separates to see the coexistence of two phase. The region below the curve is the stable region where the system is homogeneous and only one phase is present. Note that by solving only for the binodal curve, the metastable region of the system present in between the stable and unstable region was omitted. When curing the resin, the stability region decreases with a critical point (maximum of the binodal curve) that lowers in temperature. This was expected from a curing system where the increase of UP molar mass creates a destabilization of the blend. Interestingly, the composition at the critical point was in the region of what was found experimentally in Chapter 3.

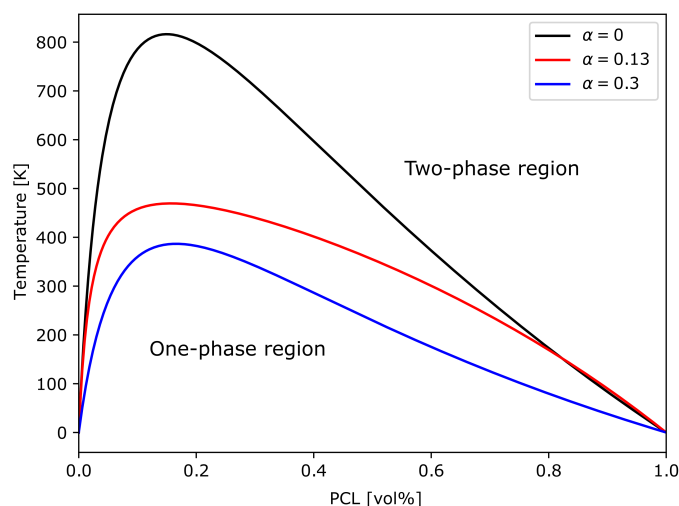


Figure A.8: Temperature phase-diagram for UP(n=4)/PCL blends at varying degree of cures.

A.5. Conclusion & Future work

The Hildebrand solubility parameters δ for polycaprolactone, styrene and unsaturated polyester were simulated by molecular dynamic simulation, and were found close to experimental values. For the polycaprolactone and styrene, an increase in temperature led

to a slight decrease of δ . The solubility parameter of the unsaturated polyester was found to decrease while increasing its molar mass and similarly decreases with an increase in temperature. A successful curing method was developed to create UP at different degree of cure and the resulting impact on δ . While curing UP, the evolution of δ showed two regimes with first an increase up to $\alpha = 0.2$, corresponding to the experimental gel-point, followed by a decrease of δ for larger degree of cure. All these behaviours correspond to what was found in the literature validating the efficiency of the simulation routine. The Flory-Huggins interaction parameters χ of UP/PCL were calculated from the simulated solubility parameters. They were found strongly affected by the initial molar mass of UP defining clear stable and unstable regions, and mostly linear with $1/T$ which is in-line with the Flory-Huggins definition of χ . From these, it was possible to create a temperature phase-diagram of the UP/PCL blend for different degree of cure showing that clearly shows a decrease in stability during the cure.

A future perspective for this work would be to include another component to the calculations and work out the ternary phase-diagram of the system. This could be done, for example, with graphene to understand its effect on the phase-separation morphology of a system and would help design processing maps to optimize percolation threshold and toughness.

References

- [1] Raffaele Mezzenga, Louis Boogh, and Jan-anders E Månson. A Thermodynamic Model for Thermoset Polymer Blends. pages 1893–1902, 2000.
- [2] Leszek A. Utracki and Charles A. Wilkie. *Polymer blends handbook*. 2014.
- [3] Jiao Jing Shao, Wei Lv, and Quan Hong Yang. Self-assembly of graphene oxide at interfaces. *Advanced Materials*, 26(32):5586–5612, 2014.

- [4] Nathan Hostettler and Pascal Hubert. A phase separation strategy for enhanced toughness self-assembly graphene-network composites. *Composites Science and Technology*, 225(March):109503, 2022.
- [5] Roberto J.J. Williams, Boris A. Rozenberg, and Jean Pierre Pascault. Reaction-Induced Phase Separation in Modified Thermosetting Polymers. *Advances in Polymer Science*, 128:95–156, 1997.
- [6] Thomas E. Gartner and Arthi Jayaraman. Modeling and Simulations of Polymers: A Roadmap. *Macromolecules*, 52(3):755–786, 2019.
- [7] William A. Pisani, Matthew S. Radue, Sorayot Chinkanjanarot, Brett A. Bednarczyk, Evan J. Pineda, Kevin Waters, Ravindra Pandey, Julia A. King, and Gregory M. Odegard. Multiscale modeling of PEEK using reactive molecular dynamics modeling and micromechanics. *Polymer*, 163(January):96–105, 2019.
- [8] O. Aluko, S. Gowtham, and G. M. Odegard. The development of multiscale models for predicting the mechanical response of GNP reinforced composite plate. *Composite Structures*, 206(January):526–534, 2018.
- [9] Yin Chang and Shu-Wei Chang. Full-atomistic simulations of poly(ϵ -caprolactone) diol models with CVFF and CGenFF. *Multiscale and Multiphysics Mechanics*, 1(4):327–340, 2016.
- [10] Yanlong Luo, Runguo Wang, Wei Wang, Liqun Zhang, and Sizhu Wu. Molecular Dynamics Simulation Insight into Two-Component Solubility Parameters of Graphene and Thermodynamic Compatibility of Graphene and Styrene Butadiene Rubber. *Journal of Physical Chemistry C*, 121(18):10163–10173, 2017.
- [11] Ahmed Jarray, Herman Wijshoff, Jurriaan A. Luiken, and Wouter K. den Otter. Systematic approach for wettability prediction using molecular dynamics simulations. *Soft Matter*, 16(17):4299–4310, 2020.
- [12] M. Belmares, M. Blanco, W. A. Goddard, R. B. Ross, G. Caldwell, S. H. Chou, J. Pham, P. M. Olofson, and Cristina Thomas. Hildebrand and hansen solubility parameters from molecular dynamics with applications to electronic nose polymer sensors. *Journal of Computational Chemistry*, 25(15):1814–1826, 2004.
- [13] Robert L. Scott. The thermodynamics of high polymer solutions. V. Phase equilibria in the ternary system: Polymer 1 - polymer 2 - solvent. *The Journal of Chemical Physics*, 17(3):279–284, 1949.
- [14] Augustinus J.M. Sweere and Johannes G.E.M. Fraaije. Accuracy Test of the OPLS-AA Force Field for Calculating Free Energies of Mixing and Comparison with PAC-MAC. *Journal of Chemical Theory and Computation*, 13(5):1911–1923, 2017.
- [15] E. Nies R. Koningsveld, W. H. Stockmayer. *Polymer Phase Diagrams: A textbook*. Oxford University Press, Inc, NewYork, 2001.
- [16] Paul J. Flory. *Principales of polymer chemistry*. Ithaca, N.Y. : Cornell University Press, 1953.

- [17] Chih-Pin G. Hsu. *An integrated analysis of styrene/unsaturated polyester free radical cross-linking polymerizations*. Ph.d dissertation, The Ohio State University, 1992.
- [18] X. Bulliard, V. Michaud, and J. A.E. Månson. Reaction-induced phase separation in poly(vinyl acetate)/ polyester blend. *Journal of Applied Polymer Science*, 102(4):3877–3888, nov 2006.
- [19] L. N. Mizerovskii and V. A. Padokhin. Molecular-Weight Distribution of Linear Polycodensation Polymers, Flory Theory. *Fibre Chemistry*, 44(6):8–22, 2013.
- [20] Stephen L. Mayo, Barry D. Olafson, and William A. Goddard. DREIDING: A generic force field for molecular simulations. *Journal of Physical Chemistry*, 94(26):8897–8909, 1990.
- [21] L. Martinez, R. Andrade, E. G Birgin, and J. M. Martinez. Packmol: A Package for Building Initial Configurations for molecular Dynamics Simulations. *Journal of computational chemistry*, 30:2157–2164, 2009.
- [22] Andrew I. Jewett, David Stelter, Jason Lambert, Shyam M. Saladi, Otello M. Roscioni, Matteo Ricci, Ludovic Autin, Martina Maritan, Saeed M. Bashusqeh, Tom Keyes, Remus T. Dame, Joan Emma Shea, Grant J. Jensen, and David S. Goodsell. Moltemplate: A Tool for Coarse-Grained Modeling of Complex Biological Matter and Soft Condensed Matter Physics. *Journal of Molecular Biology*, 433(11):166841, 2021.
- [23] Anthony K. Rappé and William A. Goddard. Charge equilibration for molecular dynamics simulations. *Journal of Physical Chemistry*, 95(8):3358–3363, 1991.
- [24] Aidan P. Thompson, H. Metin Aktulga, Richard Berger, Dan S. Bolintineanu, W. Michael Brown, Paul S. Crozier, Pieter J. in 't Veld, Axel Kohlmeyer, Stan G. Moore, Trung Dac Nguyen, Ray Shan, Mark J. Stevens, Julien Tranchida, Christian Trott, and Steven J. Plimpton. LAMMPS - a flexible simulation tool for particle-based materials modeling at the atomic, meso, and continuum scales. *Computer Physics Communications*, 271:108171, 2022.
- [25] Sabu Thomas, Mahesh Hosur, and Cintil Jose Chirayil, editors. *Unsaturated Polyester Resins: Fundamentals, Design, Fabrication and Applications*. Elsevier, 2019.
- [26] C. Bordes, V. Fréville, E. Ruffin, P. Marote, J. Y. Gauvrit, S. Briançon, and P. Lantéri. Determination of poly(ϵ -caprolactone) solubility parameters: Application to solvent substitution in a microencapsulation process. *International Journal of Pharmaceutics*, 383(1-2):236–243, 2010.
- [27] Burke and John. Solubility Parameters: Theory and Application. *The American Institute for Conservation*, 3:13–58, 1984.
- [28] Julien Molina, Aurélie Laroche, Jean Victor Richard, Anne Sophie Schuller, and Christian Rolando. Neural networks are promising tools for the prediction of the viscosity of unsaturated polyester resins. *Frontiers in Chemistry*, 7(MAY):1–15, 2019.

- [29] Rashawn Spann and David Boucher. Impact of molecular weight on the solubility parameters of poly(3-hexylthiophene). *Journal of Polymer Science*, 2022.
- [30] Chunyu Li and Alejandro Strachan. Cohesive energy density and solubility parameter evolution during the curing of thermoset. *Polymer*, 135:162–170, 2018.
- [31] Ezequiel R. Soulé, Julio Borrajo, and Roberto J.J. Williams. Thermodynamic analysis of a polymerization-induced phase separation in nanoparticle-monomer-polymer blends. *Macromolecules*, 40(22):8082–8086, 2007.

CHAPTER B
Supplementary Materials
A phase separation strategy for enhanced toughness self-assembly
graphene-network composites.

Table B.1: Detailed results for the Polylite 31520.

PCL [wt%]	2.5	5	10	15	16.5	20	25
K_{Ic} [$MPa \cdot m^{1/2}$]	0.411	0.323	0.336	0.328	0.575	0.541	0.801
σ_y [MPa]	55.02	43.66	35.68	34.48	32.22	19.86	24.53
a [cm]	0.827	0.797	0.775	0.711	0.771	0.819	0.786
a/W	0.539	0.508	0.489	0.452	0.491	0.521	0.523
$2.5 \left(\frac{K_Q}{0.7\sigma_y} \right)^2$	0.029	0.028	0.037	0.046	0.171	0.397	0.366
$W - a$ [cm]	0.707	0.772	0.809	0.863	0.799	0.755	0.718

Table B.2: Detailed results for the AOC R920.

PCL [wt%]	Neat	2.5	5	10	15	20
K_{Ic} [$MPa \cdot m^{1/2}$]	0.447	0.591	0.675	0.604	0.551	0.484
σ_y [MPa]	74.98	68.23	59.60	49.35	43.13	30.95
a [cm]	0.809	0.795	0.774	0.802	0.794	0.794
a/W	0.529	0.520	0.505	0.518	0.512	0.512
$2.5 \left(\frac{K_Q}{0.7\sigma_y} \right)^2$	0.019	0.044	0.068	0.077	0.085	0.085
$W - a$ [cm]	0.721	0.734	0.758	0.747	0.757	0.757

Table B.3: Detailed results for the PolyLite 31289.

PCL [wt%]	Neat	2	4	7	10
K_{Ic} [$MPa \cdot m^{1/2}$]	0.472	0.877	0.898	0.728	0.432
σ_y [MPa]	81.93	78.21	63.83	50.69	44.85
a [cm]	0.828	0.813	0.822	0.805	0.816
a/W	0.543	0.536	0.537	0.524	0.536
$2.5 \left(\frac{K_Q}{0.7\sigma_y} \right)^2$	0.018	0.064	0.102	0.105	0.048
$W - a$ [cm]	0.698	0.705	0.710	0.730	0.706

Table B.4: Detailed results of the PolyLite 31289 with graphene.

PolyLite 31289 - Neat

Graphene [wt%]	0	1	3	6
K_{Ic} [$MPa \cdot m^{1/2}$]	0.472	0.562	0.665	0.926
σ_y [MPa]	81.93	83.64	81.94	75.17
a [cm]	0.828	0.813	0.826	0.806
a/W	0.543	0.535	0.538	0.534
$2.5 \left(\frac{K_Q}{0.7\sigma_y} \right)^2$	0.018	0.023	0.034	0.078
$W - a$ [cm]	0.698	0.705	0.709	0.703

PolyLite 31289 - 2wt% PCL

Graphene [wt%]	0	1	3	6
K_{Ic} [$MPa \cdot m^{1/2}$]	0.877	0.783	0.908	1.012
σ_y [MPa]	78.21	81.16	74.57	72.29
a [cm]	0.813	0.826	0.816	0.811
a/W	0.536	0.541	0.539	0.526
$2.5 \left(\frac{K_Q}{0.7\sigma_y} \right)^2$	0.064	0.048	0.076	0.101
$W - a$ [cm]	0.705	0.702	0.698	0.733

Polylite 31289 - 4wt% PCL

Graphene [wt%]	0	1	3	6
K_{Ic} [$MPa \cdot m^{1/2}$]	0.898	0.864	0.898	0.878
σ_y [MPa]	63.83	61.07	66.19	58.61
a [cm]	0.822	0.806	0.802	0.830
a/W	0.537	0.524	0.530	0.539
$2.5 \left(\frac{K_Q}{0.7\sigma_y} \right)^2$	0.102	0.102	0.094	0.115
$W - a$ [cm]	0.710	0.733	0.711	0.710

Polylite 31289 - 7wt% PCL

Graphene [wt%]	0	1	3	6
K_{Ic} [$MPa \cdot m^{1/2}$]	0.728	0.699	0.672	0.747
σ_y [MPa]	50.69	42.47	45.14	45.42
a [cm]	0.805	0.793	0.817	0.810
a/W	0.524	0.518	0.519	0.528
$2.5 \left(\frac{K_Q}{0.7\sigma_y} \right)^2$	0.105	0.139	0.114	0.138
$W - a$ [cm]	0.730	0.737	0.759	0.726

B.1. Graphene morphology

We have found evidence of larger graphite residues in the graphene powder that cannot be dispersed. These particles usually appear shiny, sign of light diffraction and of a crystalline structure (see Figure B.1). We think that these shiny surfaces are fractured interfaces coming from the exfoliation process. The different nature of these large particles can also be observed in the size distribution histogram (Figure B.2) where they are found outside of the main distribution of aggregates after dispersion.

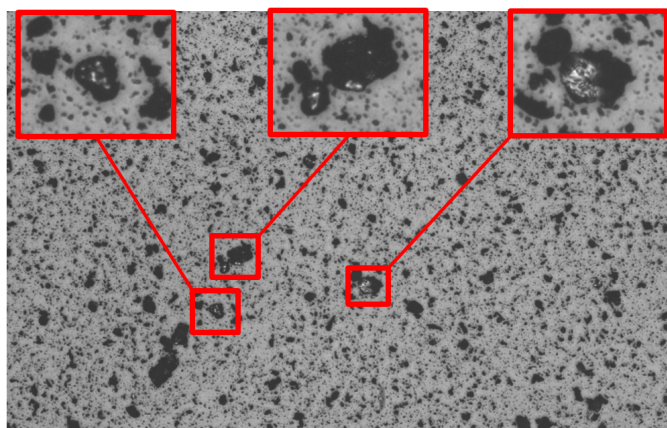


Figure B.1: close-up view of graphite residues in a 2wt% graphene sample.

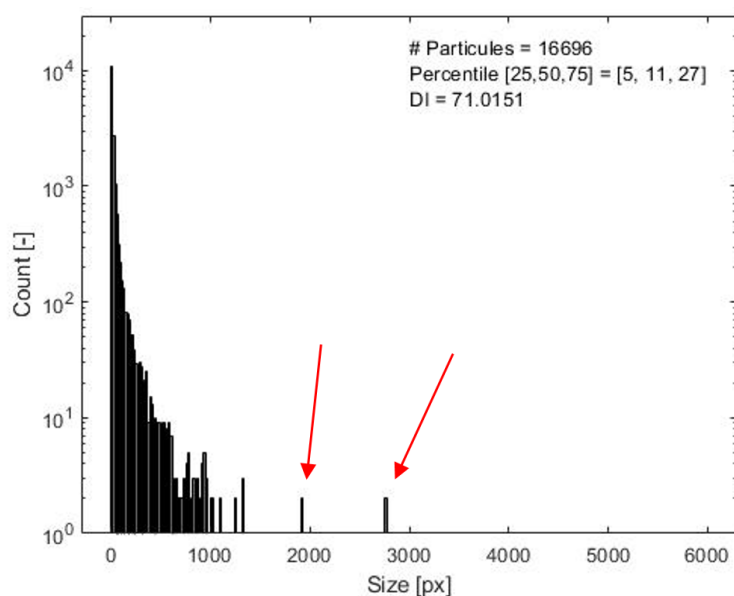


Figure B.2: size distribution histogram.

CHAPTER C

Electrical Circuits for sensing setup

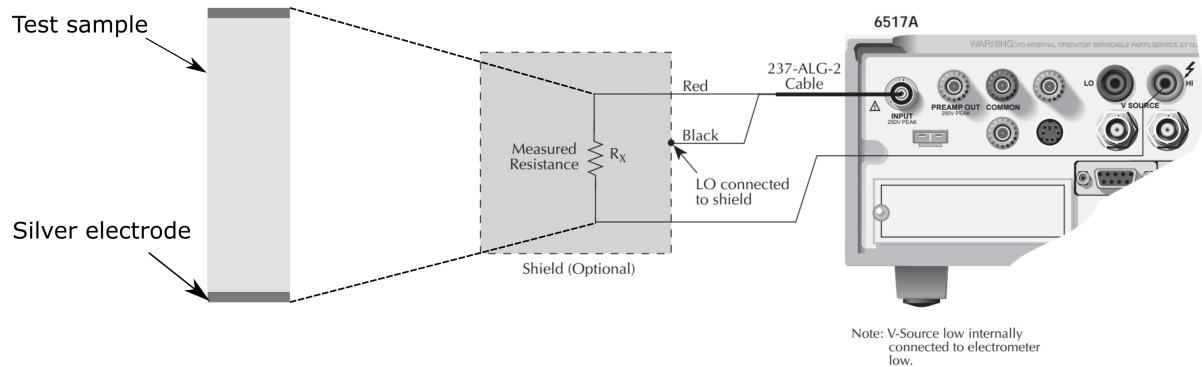


Figure C.1: 2-point equivalent electrical circuit and plugging procedure for the resistivity measurement used for strain and damage sensing. Note that no shielding was used in the context of this work. Adapted from the "Keithley Model 6517A Electrometer User's Manual" (2014).